



UNIVERSIDAD DE CONCEPCIÓN
FACULTAD DE CIENCIAS FÍSICAS Y MATEMÁTICAS
MAGÍSTER EN FÍSICA

**Exploring how deviations from the Kerr metric affect
images of supermassive black holes**

**Explorando cómo las desviaciones de la métrica de Kerr
afectan las imágenes de los agujeros negros supermasivos**

Profesor Guía: Dr. Dominik Schleicher
Departamento de Física
Facultad de Ciencias Físicas y Matemáticas
Universidad de Concepción

**Tesis para ser presentada a la Dirección de Postgrado de la Universidad
de Concepción para optar al grado de Magíster en Física**

FELIPE EDUARDO AGURTO SEPÚLVEDA
OCTUBRE DE 2023
CONCEPCIÓN, CHILE

©2023, Felipe Agurto Sepúlveda

Se autoriza la reproducción total o parcial, con fines académicos, por cualquier medio o procedimiento, incluyendo la cita bibliográfica del documento.

Acknowledgements

This project would not have been possible without the support of many people.

First and foremost, I want to thank all my family specially to my parents Maria Cristina and Eduardo, who always give me emotional and financial support in every step and road that I take in my life. I thank my uncle Cristian and my cousin Ignacio for giving me the seeds of critical thinking in my head and encourage it. I would like to express my great gratitude to my partner, Makarena, for always being with me in good and bad times and supporting me emotionally without a doubt, with special mention to your daily coffee preparations. A very special thanks to the friends I have made over the years as an undergraduate and graduate student, especially to Luis, Carolina, Carlos, Raúl, Nicolás and Michelle to make easily the pass of the undergraduate years.

Dr. Dominik Schleicher, my supervisor, deserves my sincerest gratitude for his advice, encouragement, and his insightful comments. I would like to express my gratitude to Dr. Julio Oliva always enlightened comments and for clarifying my ideas about the physics and life, for making numerous helpful ideas and collaborations for the project, and for sharing his knowledge. I owe a sincere gratitude to Bidisha Bandyopadhyay who helped me in the beginning of the project, to solve answers and clarifying how this types of simulations works. And finally I would like to express my gratitude to Marcelo Oyarzo for being a good friend and helping me in the understanding of physics from modified gravitation theories and also for sharing his knowledge and enlightenment comments in the road to finishing my thesis project.

We gratefully acknowledge support by the ANID BASAL projects ACE210002 and FB210003, as well as via the Millenium Nucleus NCN19-058 (TITANs).

Resumen

La descripción de los agujeros negros (BH) según la Relatividad General (GR), en particular a través de la solución de Kerr, se basa en suposiciones simplificadas. En este contexto, investigamos el impacto de las desviaciones de la solución de Kerr en las imágenes de agujeros negros supermasivos (SMBH). Utilizamos simulaciones de Transporte de Radiación Relativista General, centrándonos en la métrica de Kerr-Like, que presenta cuatro funciones no-lineales de desviación, es estacionaria, axisimétrica y asintóticamente plana. Además, exploramos dos métricas de gravedad modificada: la teoría de Chern-Simons y la de α' -corrected, ambas derivadas como límites de baja energía de la teoría de cuerdas.

Para obtener imágenes, empleamos el código RAPTOR I, un trazador de rayos de código abierto que admite diversas geometrías espacio-temporales. Cuantificamos las desviaciones al estudiar la asimetría, el diámetro y el desplazamiento de la sombra del BH, y las comparamos con un BH de Kerr. Nuestros resultados validan la efectividad del método desarrollado para medir desviaciones y muestran que estas afectan la forma de la sombra, siendo especialmente relevantes las desviaciones $A_1(r)$ y $A_2(r)$ de la métrica Kerr-Like. No obstante, observamos que la distribución de la materia y las emisividades alrededor del agujero negro también influyen. Por ende, la geometría y los efectos de las desviaciones en la sombra no pueden predecirse exclusivamente desde la forma del anillo de fotones.

Además, demostramos que las desviaciones originadas por teorías de gravedad modificada, especialmente el límite efectivo de la gravedad de Chern-Simons, son imperceptibles en las imágenes de agujeros negros. Asimismo, presentamos la separabilidad de la solución de agujero negro rotante lento en la teoría α' -corrected en las ecuaciones de Hamilton-Jacobi, lo cual promueve futuros estudios de su sombra.

Keywords – acreción, discos de acreción, física de agujeros negros, transferencia radiativa.

Abstract

The description of black holes (BH) according to General Relativity (GR), particularly through the Kerr solution, is based on simplified assumptions. In this context, we investigate the impact of deviations from the Kerr solution on images of supermassive black holes (SMBHs). We utilize simulations of General Relativistic Radiative Transport, focusing on the Kerr-Like metric, which features four non-linear functions of free deviation, is stationary, axisymmetric, and asymptotically flat. Additionally, we explore two metrics of modified gravity: the Chern-Simons theory and the α' -corrected theory, both derived as low-energy limits of string theory.

To obtain images, we employ the RAPTOR I code, an open-source ray-tracing tool that supports diverse spacetime geometries. We quantify deviations by studying the asymmetry, diameter, and displacement of the BH shadow, comparing them with a Kerr BH. Our results validate the effectiveness of the developed method for measuring deviations and show that these affect the shape of the shadow, with the deviations $A_1(r)$ and $A_2(r)$ of the Kerr-Like metric being particularly relevant. However, we observe that the distribution of matter and emissivities around the black hole also play a role. Thus, the geometry and effects of deviations on the shadow cannot be solely predicted from the shape of the photon ring.

Furthermore, we demonstrate that deviations arising from modified gravity theories, especially the effective limit of Chern-Simons gravity, are imperceptible in black hole images. Likewise, we present the separability of the slowly-rotating black hole solution in the α' -corrected theory within the Hamilton-Jacobi equations, which promotes future studies of its shadow.

Keywords – accretion, accretion disks, black hole physics, radiative transfer.

Contents

ACKNOWLEDGEMENTS	i
Resumen	ii
Abstract	iii
1 Introduction	1
2 About black holes	8
2.1 Compact Objects	8
2.2 General Relativity	9
2.3 Schwarzschild solution	13
2.3.1 Schwarzschild radius	17
2.3.2 Event Horizon	18
2.3.3 Bound orbits in Schwarzschild metric	24
2.4 Kerr solution	28
2.4.1 Properties	29
2.4.1.1 Event Horizon and Ergosphere	31
2.4.1.2 ISCO radius	33
2.5 Kerr-Like metric	36
2.5.1 Properties of Kerr-Like metric	40
2.5.1.1 Event Horizon	42
2.5.1.2 Ergosphere	44
2.5.1.3 ISCO radius	44
2.5.2 Kerr-Schild-Like metric	46
2.6 Accretion Disks	49
2.6.1 The fluid	50
2.6.2 Viscosity	51
2.6.3 Electromagnetic part	53
2.6.4 The radiation	54
2.6.5 Thin Disk model	55
2.6.6 HARM simulations	60
2.6.6.1 Theoretical scheme	61
2.6.6.2 Numerical scheme	63
2.7 Beyond Einstein Gravity	65
2.7.1 Slowly rotating Chern-Simons black hole solution	65
2.7.2 Slowly rotating α' theory black hole solution	69

3	Computational methods	73
3.1	Ray-Tracing	75
3.2	RAPTOR I	77
3.2.1	Inputs and Outputs of the code	78
3.2.2	Virtual camera	79
3.2.3	Numerical integration of the geodesic equation	79
3.2.3.1	Runge-Kutta	80
3.2.3.2	Vervlet	81
3.2.4	Radiative transfer	82
3.2.5	Emission model	85
3.2.5.1	Thin disk emission	85
3.2.5.2	Synchrotron emission	86
3.2.6	Fluid model	89
3.2.6.1	Novikov-Thorne Thin disk model	89
3.2.6.2	HARM model	92
3.3	Kerr-Like metric implementation	94
3.4	Intensity profile	98
3.4.1	Displacement, Diameter, and Asymmetry	100
4	Effects of the deviations from the Kerr metric and GRMHD simulations	103
4.1	Kerr-Like metric simulations	104
4.1.1	HARM model simulations	106
4.1.1.1	Deviation parameter α_{13}	107
4.1.1.2	Deviation parameter α_{22}	112
4.1.1.3	Deviation parameter α_{52}	115
4.1.1.4	Sgr A* case	117
4.1.2	Thin-disk model simulations	125
4.1.2.1	Deviation parameter α_{13}	126
4.1.2.2	Deviation parameter α_{22}	129
4.1.2.3	Implications of the Kerr-Like simulations	134
4.2	Beyond Einstein gravity	136
4.2.1	Slowly rotating Chern-Simons black hole solution	137
4.2.1.1	Kerr-Schild form	137
4.2.1.2	Relation with the Kerr-Like metric	140
4.2.1.3	Thin-disk simulations and analysis	141
4.2.2	Slowly rotating α' -corrected black hole solution	149
4.2.2.1	Kerr-Schild form	150
4.2.2.2	Separability of Hamilton-Jacobi equations and implications	151
5	Summary and discussion	155
	Bibliography	158
	Appendix	167

A	Supplementary calculations	167
A1	Modified coordinates	167
A1.1	From Boyer-Lindquist to Kerr-Schild	167
A1.2	From Kerr-Schild to Modified Kerr-Schild coordinates	168
A2	Christoffel symbols of Kerr-Like metric	169

List of Tables

2.1.1	Comparison of compact objects with a normal star (Sun) extracted from Shapiro and Teukolsky (2008)	9
3.2.1	Inputs for RAPTOR code.	78
3.2.2	Settings extracted from the test using in Bronzwaer et al. (2020)	91
3.2.3	Setup for the simulation of the SMBH with the distance and mass of M87*.	94
4.1.1	Setup for the simulation of the SMBH with the distance and mass of M87*	107
4.1.2	Setup for the simulation of the SMBH with the distance and mass of Sgr A*	118
4.1.3	Setting inspired in the test values used in Bronzwaer et al. (2020)	125
4.2.1	Settings based on previously for a thin accretion disk but with a spin parameter $a = 0.4M$ to works well in the slowly rotating limit.	144

List of Figures

2.3.1	The Finkelstein diagram for ingoing Eddington-Finkelstein coordinates.	23
3.0.1	First simulated image of a thin accretion disk around a Schwarzschild black hole (Luminet, 1979).	74
3.1.1	An esquematic diagram of the ray tracing algorithm (Henrik, 2023).	76
3.2.1	Thin-disk simulation for BH with a mass $10M_{\odot}$ and spin $a = 0.99 M$. With angle of view $i = 30^{\circ}$, $i = 60^{\circ}$ and $i = 90^{\circ}$	91
3.2.2	GRMHD simulation for SMBH with a mass $6.2 \times 10^9 M_{\odot}$ and spin $a = 0.9375 M$. With angle of view $i = 30^{\circ}$, $i = 60^{\circ}$ and $i = 90^{\circ}$	93
3.3.1	Comparison between the covariant components g_{tt} and $g_{t\phi}$ of the Kerr and Kerr-Like metrics. In the left panel of the figures, the comparison can be observed when the Kerr-Like metric has its free deviations set to zero (i.e., $\alpha_{13} = \alpha_{22} = 0$), thus reducing it to the Kerr metric. In the right panel of the figure, the difference can be seen when turning on the free deviations to first order in both functions $A_1(r)$ and $A_2(r)$, such that they have their maximum deviation values (i.e., $\alpha_{13} = -1$ and $\alpha_{22} = 1$).	96
3.3.2	Comparison between the contravariant components g^{tt} and $g^{t\phi}$ of the Kerr and Kerr-Like metrics. In the left panel of the figures, the comparison can be observed when the Kerr-Like metric has its free deviations set to zero (i.e., $\alpha_{13} = \alpha_{22} = 0$), reducing it to the Kerr metric. In the right panel of the figure, the difference is evident when the free deviations are activated to first order in both functions $A_1(r)$ and $A_2(r)$, such that they have their maximum deviation values (i.e., $\alpha_{13} = -1$ and $\alpha_{22} = 1$).	97
3.3.3	GRMHD simulation for a SMBH with a mass similar to M87* and spin $a = 0.9375 M$. In the left part of the figure a simulation of the Kerr-Like metric with deviation parameter $\alpha_{13} = -1$ and to compare this in the right part of the figure a simulation of a Kerr metric, with angle of view $i = 90^{\circ}$ (i.e edge-on).	98

3.4.1	An Example of four simulated images of a Kerr BH with the mass of Sgr A* (<i>Above images</i>) with the normalized intensity color bar and below each image the intensity profiles for three different angles of intensity measurement values. The <i>white dashed line</i> represents the circular orbit of the photon ring for a Kerr BH, included for the purpose of comparison with the shadow.	100
3.4.2	<i>(Blue line)</i> is the fit calculated by Johannsen and the <i>(Red dots)</i> are the values obtained by a post-processing data of the SMBH with the mass of M87* and spin $a = 0.9375M$ of the GRMHD simulated image.	102
4.1.1	Comparison between a Kerr photon ring for a circular orbit (<i>black line</i>) for a BH with spin $a = 0.9375 M$ and Kerr-Like with the deviation parameters $\alpha_{13} = [-1, 1]$ (<i>red and blue line</i>), respectively and angle of view $i = [1^\circ, 45^\circ, 90^\circ]$	105
4.1.2	Comparison between a Kerr photon ring for a circular orbit (<i>black line</i>) for a BH with spin $a = 0.9375 M$ and Kerr-Like with deviation parameters $\alpha_{22} = [-1, 1]$ (<i>red and blue line</i>), respectively and angle of view $i = [1^\circ, 45^\circ, 90^\circ]$	106
4.1.3	This figure displays a GRMHD simulation of a Kerr-Like black hole, which has a mass similar to that of M87* (with a spin of $a = 0.9375M$ and a deviation parameter $\alpha_{13} = -1$). In the upper panel, intensity maps are presented from four different viewing angles (0, 30, 60, 90 degrees). These maps show us how the shape of the black hole's shadow and the intensity of the disk change as we vary the viewing angle. The white line on each map represents the contour of the photon ring in a Kerr SMBH, allowing us to compare it with the shadow in this Kerr-Like metric. In the lower panel, intensity profiles corresponding to the upper images are shown. Each image has three intensity profiles taken from different angles. By observing how the height and location of the peak points change along the x-axis in these profiles, we can perform subsequent analysis of the diameter, displacement, and asymmetry of the black hole's shadow. . .	108

- 4.1.4 GRMHD simulation of a Kerr-Like black hole, which has a mass similar to that of M87* (with a spin of $a = 0.9375M$ and a deviation parameter $\alpha_{13} = 1$). In the upper panel, intensity maps are presented from four different viewing angles (0, 30, 60, 90 degrees). These maps show us how the shape of the black hole's shadow and the intensity of the disk change as we vary the viewing angle. The white line on each map represents the contour of the photon ring in a Kerr SMBH, allowing us to compare it with the shadow in this Kerr-Like metric. In the lower panel, intensity profiles corresponding to the upper images are shown. Each image has three intensity profiles taken from different angles. By observing how the height and location of the peak points change along the x-axis in these profiles, we can perform subsequent analysis of the diameter, displacement, and asymmetry of the black hole's shadow. 109
- 4.1.5 Comparison of diameter, displacement, and asymmetry values. It includes the fit calculated by Johannsen (2013a) (Blue line) for a Kerr-Like black hole with a deviation parameter $\alpha_{13} = -1$ (Red dashed line), $\alpha_{13} = 1$, and a Kerr-Like simulation (Red dots and Blue stars) of a black hole with these deviation parameters, respectively, alongside the simulation of a Kerr black hole (Orange triangles). The graph illustrates how these values change as the viewing angle varies from 0 to 90 degrees. It shows that the first two cases exhibit similar trends, while the last one behaves differently. It is noteworthy that there is a clear distinction in the values that consider deviations from the standard Kerr metric. 110
- 4.1.6 Comparison of how the values of diameter, displacement, and asymmetry change as the viewing angle varies from 0 to 90 degrees in simulations of a Kerr-Like black hole with deviation parameters $\alpha_{13} = -1$ (Blue stars), $\alpha_{13} = -0.5$ (Red dots), $\alpha_{13} = 0.5$ (Orange diamonds), $\alpha_{13} = 1$ (Dark cyan plus sign), and in the simulation of a Kerr black hole (Black triangles). Noticeable differences are observed between the deviated values and the background value for the Kerr simulation, although all differences are slight compared to Kerr. 112

- 4.1.7 GRMHD simulation of a Kerr-Like black hole, which has a mass similar to that of $M87^*$ (with a spin of $a = 0.9375M$ and a deviation parameter $\alpha_{22} = -1$). In the upper panel, intensity maps are presented from four different viewing angles (0, 30, 60, 90 degrees). These maps show us how the shape of the black hole's shadow and the intensity of the disk change as we vary the viewing angle. The white line on each map represents the contour of the photon ring in a Kerr SMBH, allowing us to compare it with the shadow in this Kerr-Like metric. In the lower panel, intensity profiles corresponding to the upper images are shown. Each image has three intensity profiles taken from different angles. By observing how the height and location of the peak points change along the x-axis in these profiles, we can perform subsequent analysis of the diameter, displacement, and asymmetry of the black hole's shadow. 113
- 4.1.8 GRMHD simulation of a Kerr-Like black hole, which has a mass similar to that of $M87^*$ (with a spin of $a = 0.9375M$ and a deviation parameter $\alpha_{22} = 1$). In the upper panel, intensity maps are presented from four different viewing angles (0, 30, 60, 90 degrees). These maps show us how the shape of the black hole's shadow and the intensity of the disk change as we vary the viewing angle. The white line on each map represents the contour of the photon ring in a Kerr SMBH, allowing us to compare it with the shadow in this Kerr-Like metric. In the lower panel, intensity profiles corresponding to the upper images are shown. Each image has three intensity profiles taken from different angles. By observing how the height and location of the peak points change along the x-axis in these profiles, we can perform subsequent analysis of the diameter, displacement, and asymmetry of the black hole's shadow. 114
- 4.1.9 Comparison of the diameter, displacement, and asymmetry values for a Kerr-Like BH simulations with deviation parameters $\alpha_{22} = -1$ (*Blue stars*), $\alpha_{22} = -0.5$ (*Red dots*), $\alpha_{22} = 0.5$ (*Orange diamonds*), $\alpha_{22} = 1$ (*Dark cyan plus sign*), and in the simulation of a Kerr black hole (*Black triangles*) and how these values change as the viewing angle varies from 0 to 90 degrees, showing noticeable differences between the deviated values and the background value for the Kerr simulation, although all differences are slight compared to Kerr. 115

- 4.1.10 GRMHD simulation of a Kerr-Like black hole, which has a mass similar to that of $M87^*$ (with a spin of $a = 0.9375M$ and a deviation parameter $\alpha_{52} = -1$). In the upper panel, intensity maps are presented from four different viewing angles (0, 30, 60, 90 degrees). These maps show us how the shape of the black hole's shadow and the intensity of the disk change as we vary the viewing angle. The white line on each map represents the contour of the photon ring in a Kerr SMBH, allowing us to compare it with the shadow in this Kerr-Like metric. In the lower panel, intensity profiles corresponding to the upper images are shown. Each image has three intensity profiles taken from different angles. By observing how the height and location of the peak points change along the x-axis in these profiles, we can perform subsequent analysis of the diameter, displacement, and asymmetry of the black hole's shadow. 116
- 4.1.11 Comparison of how the values of diameter, displacement, and asymmetry change as the viewing angle varies from 0 to 90 degrees in simulations of a Kerr-Like black hole with deviation parameters $\alpha_{52} = -1$ (*Blue stars*), $\alpha_{52} = -0.5$ (*Red dots*), $\alpha_{52} = 0.5$ (*Orange diamonds*), $\alpha_{52} = 1$ (*Dark cyan plus sign*), and in the simulation of a Kerr black hole (*Black triangles*). Noticeable differences are observed between the deviated values and the background value for the Kerr simulation, although all differences are slight compared to Kerr. 117
- 4.1.12 GRMHD simulation of a Kerr-Like black hole, which has a mass of $SgrA^*$ (with a spin of $a = 0.9375M$ and a deviation parameter $\alpha_{13} = -1$). In the upper panel, intensity maps are presented from four different viewing angles (0, 30, 60, 90 degrees). These maps show us how the shape of the black hole's shadow and the intensity of the disk change as we vary the viewing angle. The white line on each map represents the contour of the photon ring in a Kerr SMBH, allowing us to compare it with the shadow in this Kerr-Like metric. In the lower panel, intensity profiles corresponding to the upper images are shown. Each image has three intensity profiles taken from different angles. By observing how the height and location of the peak points change along the x-axis in these profiles, we can perform subsequent analysis of the diameter, displacement, and asymmetry of the black hole's shadow. . . 119

- 4.1.13 GRMHD simulation of a Kerr-Like black hole, which has a mass of $SgrA^*$ (with a spin of $a = 0.9375M$ and a deviation parameter $\alpha_{13} = 1$). In the upper panel, intensity maps are presented from four different viewing angles (0, 30, 60, 90 degrees). These maps show us how the shape of the black hole's shadow and the intensity of the disk change as we vary the viewing angle. The white line on each map represents the contour of the photon ring in a Kerr SMBH, allowing us to compare it with the shadow in this Kerr-Like metric. In the lower panel, intensity profiles corresponding to the upper images are shown. Each image has three intensity profiles taken from different angles. By observing how the height and location of the peak points change along the x-axis in these profiles, we can perform subsequent analysis of the diameter, displacement, and asymmetry of the black hole's shadow. . . 120
- 4.1.14 GRMHD simulation of a Kerr-Like black hole, which has a mass of $SgrA^*$ (with a spin of $a = 0.9375M$ and a deviation parameter $\alpha_{22} = -1$). In the upper panel, intensity maps are presented from four different viewing angles (0, 30, 60, 90 degrees). These maps show us how the shape of the black hole's shadow and the intensity of the disk change as we vary the viewing angle. The white line on each map represents the contour of the photon ring in a Kerr SMBH, allowing us to compare it with the shadow in this Kerr-Like metric. In the lower panel, intensity profiles corresponding to the upper images are shown. Each image has three intensity profiles taken from different angles. By observing how the height and location of the peak points change along the x-axis in these profiles, we can perform subsequent analysis of the diameter, displacement, and asymmetry of the black hole's shadow. . . 122
- 4.1.15 GRMHD simulation of a Kerr-Like black hole, which has a mass of $SgrA^*$ (with a spin of $a = 0.9375M$ and a deviation parameter $\alpha_{22} = 1$). In the upper panel, intensity maps are presented from four different viewing angles (0, 30, 60, 90 degrees). These maps show us how the shape of the black hole's shadow and the intensity of the disk change as we vary the viewing angle. The white line on each map represents the contour of the photon ring in a Kerr SMBH, allowing us to compare it with the shadow in this Kerr-Like metric. In the lower panel, intensity profiles corresponding to the upper images are shown. Each image has three intensity profiles taken from different angles. By observing how the height and location of the peak points change along the x-axis in these profiles, we can perform subsequent analysis of the diameter, displacement, and asymmetry of the black hole's shadow. . . 123

- 4.1.16 Comparison of the diameter, displacement, and asymmetry values for a Kerr-Like BH simulations with the mass of $SgrA^*$ and with deviation parameters $\alpha_{13} = -1$ (*Blue stars*), $\alpha_{22} = -1$ (*Red dots*), $\alpha_{13} = 1$ (*Orange diamonds*), $\alpha_{22} = 1$ (*Dark cyan plus sign*), and in the simulation of a Kerr black hole (*Black triangles*). This comparison highlights how these values change as the viewing angle varies from 0 to 90 degrees, revealing significant differences between the deviated values and the background value for the Kerr simulation. Furthermore, distinct differences are observed compared to the previously shown deviations for the mass of $M87^*$, particularly notable are the more abrupt and larger changes as the viewing angle increases, especially in diameter and displacement, changes expected to be caused by the structure of the disk. 124
- 4.1.17 Thin accretion disk simulation of a Kerr-Like black hole with a mass of $10M_{\odot}$ (with a spin of $a = 0.93M$ and a deviation parameter $\alpha_{13} = -1$). In the upper panel, intensity maps are presented from four different viewing angles (0, 30, 60, 89 degrees). These maps show us how the shape of the black hole's shadow and the intensity of the disk change as we vary the viewing angle. The white line on each map represents the contour of the photon ring in a Kerr BH, allowing us to compare it with the shadow in this Kerr-Like metric. In the lower panel, intensity profiles corresponding to the upper images are shown. Each image has three intensity profiles taken from different angles. By observing how the height and location of the peak points change along the x-axis in these profiles, we can perform subsequent analysis of the diameter, displacement, and asymmetry of the black hole's shadow. . . 126
- 4.1.18 Thin accretion disk simulation of a Kerr-Like black hole with a mass of $10M_{\odot}$ (with a spin of $a = 0.93M$ and a deviation parameter $\alpha_{13} = 1$). In the upper panel, intensity maps are presented from four different viewing angles (0, 30, 60, 89 degrees). These maps show us how the shape of the black hole's shadow and the intensity of the disk change as we vary the viewing angle. The white line on each map represents the contour of the photon ring in a Kerr BH, allowing us to compare it with the shadow in this Kerr-Like metric. In the lower panel, intensity profiles corresponding to the upper images are shown. Each image has three intensity profiles taken from different angles. By observing how the height and location of the peak points change along the x-axis in these profiles, we can perform subsequent analysis of the diameter, displacement, and asymmetry of the black hole's shadow. . . 127

- 4.1.19 Comparison of the diameter, displacement, and asymmetry values for a $10M_{\odot}$ BH in a thin disk simulation between the fit calculated by Johannsen (*Blue line*) for a Kerr-Like BH with a deviation parameter $\alpha_{13} = -1$ (*Red dashed line*), $\alpha_{13} = 1$ and a Kerr-Like simulation (*Blue stars* and *Red dots*) of a BH with these deviation parameters, respectively, and with the Kerr BH simulation (*Orange triangles*). This illustrates how these values change as the viewing angle towards the BH changes, noticing a notable shift as we approach edge-on angles. Here, the diameter consistently decreases in comparison to the fits, and the displacement increases until decreasing abruptly near 90° , while the asymmetry always grows. These changes induced by the deviations are quite pronounced in comparison to Kerr in this model. 128
- 4.1.20 Thin accretion disk simulation of a Kerr-Like black hole with a mass of $10M_{\odot}$ (with a spin of $a = 0.93M$ and a deviation parameter $\alpha_{22} = -1$). In the upper panel, intensity maps are presented from four different viewing angles (0, 30, 60, 89 degrees). These maps show us how the shape of the black hole's shadow and the intensity of the disk change as we vary the viewing angle. The white line on each map represents the contour of the photon ring in a Kerr BH, allowing us to compare it with the shadow in this Kerr-Like metric. In the lower panel, intensity profiles corresponding to the upper images are shown. Each image has three intensity profiles taken from different angles. By observing how the height and location of the peak points change along the x-axis in these profiles, we can perform subsequent analysis of the diameter, displacement, and asymmetry of the black hole's shadow. . . 130
- 4.1.21 Thin accretion disk simulation of a Kerr-Like black hole with a mass of $10M_{\odot}$ (with a spin of $a = 0.93M$ and a deviation parameter $\alpha_{22} = 1$). In the upper panel, intensity maps are presented from four different viewing angles (0, 30, 60, 89 degrees). These maps show us how the shape of the black hole's shadow and the intensity of the disk change as we vary the viewing angle. The white line on each map represents the contour of the photon ring in a Kerr BH, allowing us to compare it with the shadow in this Kerr-Like metric. In the lower panel, intensity profiles corresponding to the upper images are shown. Each image has three intensity profiles taken from different angles. By observing how the height and location of the peak points change along the x-axis in these profiles, we can perform subsequent analysis of the diameter, displacement, and asymmetry of the black hole's shadow. . . 131

- 4.1.22 Comparison of the diameter, displacement, and asymmetry values for a $10M_{\odot}$ BH in a thin disk simulation between the fit calculated by Johanssen (*Blue line*) for a Kerr-Like BH with a deviation parameter $\alpha_{22} = -1$ (*Red dashed line*), $\alpha_{22} = 1$ and a Kerr-Like simulation (*Blue stars* and *Red dots*) of a BH with these deviation parameters, respectively, and with the Kerr BH simulation (*Orange triangles*). This illustrates how these values change as the viewing angle towards the BH changes, noticing a notable shift as we approach edge-on angles. Here, the diameter consistently decreases in comparison to the fits, and the displacement increases until decreasing abruptly near 90° , while the asymmetry always grows. These changes induced by the deviations are quite pronounced in comparison to Kerr in this model. 132
- 4.1.23 Comparison of how the values of diameter, displacement, and asymmetry change as the viewing angle varies from 0 to 90 degrees in simulations of thin accretion disk around a Kerr-Like BH with mass of $10M_{\odot}$ and with deviation parameters $\alpha_{13} = -1$ (*Blue stars*), $\alpha_{22} = -1$ (*Red dots*), $\alpha_{13} = 1$ (*Orange diamonds*), $\alpha_{22} = 1$ (*Dark cyan plus sign*), and in the simulation of a Kerr black hole (*Black triangles*). This comparison reveals significant differences between the deviated and the Kerr simulation's background values. Furthermore, it shows a significant difference compared to the simulations carried out with the HARM model. In this case, apart from the disk's effect on these values, a notable difference is observed due to the geometry altering the position of R_{ISCO} 133
- 4.1.24 Comparison between two intensity maps of a thin accretion disk simulations, one for a BH in a Kerr space-time with a spin parameter $a = 0.71M$ and mass $M = 10M_{\odot}$ and the second one is for a BH in a Kerr-Like space-time with a spin parameter $a = 0.93M$ with the same mass $M = 10M_{\odot}$ and the deviation parameter of $\alpha_{22} = -1$, both for a four different angles of view, from face-on to edge-on, and the intensity values normalized and shown in the side color bar. 135
- 4.1.25 Comparison of diameter, displacement, and asymmetry values between a Kerr BH simulation with a spin parameter of $a = 0.71M$ (*Black triangles*) and a Kerr-Like BH simulation with a deviation parameter $\alpha_{22} = -1$ and a spin parameter of $a = 0.93M$ (*Red dots*), both with a mass of $10M_{\odot}$. This illustrates how these parameters change as the viewing angle varies from 0 to 90 degrees. It's also worth noting that there are no apparent differences between both simulations despite having different spin parameters. 136

- 4.2.1 Comparison between photon rings for Kerr black hole (*black line*) and for a Slowly rotating Chern-Simons black hole (*cyan line*) with a spin parameter $a = 0.4M$ (to works well in the slowly rotating limit) and with a coupling values of $\zeta_{CS} = [0.4, 0.6, 0.8]$. The upper panel of the figure shows an angle of view face-on (i.e 1°) and the lower panel of the figure shows an edge-on angle of view (i.e 90°). This shows that initially there is no difference between the photon rings for these two viewing angles and the different coupling parameters for the theory. 143
- 4.2.2 Comparison of intensity maps in thin-disk simulations within the slowly rotating Chern-Simons black hole solution. This is conducted for a black hole with a mass of $10M_\odot$ and coupling values of $\zeta_{CS} = [0., 0.4, 0.6, 0.8]$, a spin parameter of $a = 0.4M$, and viewing angles of $\theta_0 = [0, 30, 60, 89]^\circ$. The normalized intensity is represented in the side color bar. 145
- 4.2.3 Comparison between diameter, displacement and asymmetry taking for a different inclinations angles from the simulations of a Kerr black hole and for a Chern-Simons Slowly rotating solution with a coupling values of $\zeta_{CS} = [0.4, 0.6, 0.8]$. Here it is shown how these parameters change as the viewing angle varies from 0 to 90 degrees. This reveals that there is no apparent change in these values for the different coupling values, namely 0.4 (*Cyan stars*), 0.6 (*Red dots*), and 0.8 (*Yellow diamonds*). 146
- 4.2.4 Comparison of diameter, displacement, and asymmetry calculated by the photon rings for different values of the coupling term $\zeta_{CS} = [0, 10]$ with a constant angle of view of 90° . In this scenario, it should be possible to observe more significant changes compared to the Kerr metric, where these parameters remain constant, along with a spin parameter of $a = 0.4M$. We notice that as the coupling term exceeds 1, changes in the diameter, displacement, and asymmetry parameters in the photon ring start to appear, in the hypothetical case where $\zeta_{CS} > 1$ 148
- 4.2.5 Comparison of the photon rings for a different values of $\zeta_{CS} \geq 1$ and the Kerr metric photon ring boths with a 90° angle of view and spin parameter $a = 0.4M$. Here, a noticeable difference in the shape of the ring is observed on the left side, where there is a flattening towards the center as the coupling value ζ_{CS} increases. 149

Chapter 1

Introduction

The theory of General Relativity (GR) is widely accepted as the most well-established explanation of gravity. Since its introduction by Albert Einstein in 1915 (Einstein, 1915a), numerous physicists have conducted research and predicted several effects and phenomena, such as gravitational waves (Einstein, 1916, 1918), the Shapiro effect (Shapiro, 1964), gravitational redshift (Einstein, 1989), and the existence of black holes (Chandrasekhar, 1935; Oppenheimer and Volkoff, 1939), to name a few.

To verify its validity, numerous tests have been developed and today can be divided into two categories: weak field tests and strong field tests.

The weak field tests are performed in regions where the gravitational field is weak, and the effects of General Relativity (GR) can be described as small modifications to Newtonian gravity. These tests include the deflection of light by the Sun, the precession of Mercury's orbit, and the gravitational redshift of light.

In contrast, strong field tests are conducted in areas where the gravitational field is strong, and the effects of GR cannot be approximated as simple modifications to Newtonian gravity. Examples of these tests include the detection of gravitational waves, the periastron precession in binary pulsars, and direct observations of black holes.

The precession of Mercury's perihelion, first observed by Le Verrier (1859), defied explanation within the framework of Newtonian gravity. However,

Einstein's General Relativity (GR) predicted this phenomenon, foreseeing a precession value of approximately $\Delta\phi \approx 43'' \text{ century}^{-1}$ (Einstein, 1915b), representing the variability of the orbital axis over time. Current measurements closely align, at $42''.98 \pm 4 \text{ century}^{-1}$ (Lo et al., 2013), with Einstein's predictions.

Einstein's 1907 (Einstein, 1989) prediction of light deflection in a gravitational field was experimentally verified during the 1919 solar eclipse by Frank Dyson and Arthur Eddington (Dyson et al., 1920). Modern measurements, such as Very Long Baseline Interferometry (VLBI) (Shapiro et al., 2004), have further confirmed this phenomenon. Additionally, another GR prediction, gravitational redshift, was initially confirmed by Adams (1925) for Sirius B⁽¹⁶⁾ and more recently by Biriukov et al. (2014) using the Russian satellite RadiAstron. These tests validate GR, especially in the weak field regime. Beyond this, Shapiro et al. (1968) work studied the Shapiro effect, while LIGO (Abbott et al., 2016) detected gravitational waves in strong field conditions. Meanwhile, the Event Horizon Telescope (Collaboration et al., 2019) captured the first image of a black hole at the center of the M87 galaxy, putting Einstein's GR to the test in the strong field regime and further corroborating its validity.

Black holes are important for studying strong gravitational fields and are a recognizable prediction of Einstein's General Relativity. They provide opportunities for testing the theory through strong field tests, including the detection of gravitational waves and observations of black holes. The study of black holes began with Schwarzschild's spherically symmetrical solution (Schwarzschild, 1916) of Einstein's field equations, which was later refined by Lorentz and Eddington to determine their properties.

In 1963, Roy Kerr discovered another spherically symmetric but rotating solution (Kerr, 1963) that also supported the existence of gravitational collapsing solutions which describe black holes. Later, Newmann extended this solution to include electric charge. Building on these discoveries, the scientists Werner, Carter, and David Robinson showed that black holes can be fully characterized by three parameters: their angular momentum, mass, and electric charge. This conclusion is now referred to as the No-Hair Theorem.

The observational search for astrophysical black hole candidates in the Universe

began in the 1970s. Nowadays, we have observational evidence that at least two types of these objects exist: stellar-mass black holes ($M \approx 3 - 100M_{\odot}$) and supermassive black holes ($M \approx 10^5 - 10^{10}M_{\odot}$). There is also a belief that intermediate-mass black holes could exist, but there is no clear theoretical or observational clarity regarding them. However, in recent years, there have been potential detections and interest in these objects (Lin et al., 2020; Vitral et al., 2023).

Stellar-mass black holes form from the complete collapse of massive stars. When a star depletes its nuclear fuel through fusion, internal gas pressure can no longer counteract gravity, leading to collapse. This process often expels much material violently. This happens primarily to stars of $25M_{\odot}$ or greater, creating a black hole. For lower masses, quantum pressure from electrons or neutrons prevents strong gravitational collapse, resulting in white dwarfs or neutron stars (Rhoades Jr and Ruffini, 1974; Farr et al., 2011). However, stellar-mass black holes typically max out at around $\approx 100M_{\odot}$ (Belczynski et al., 2010; Spera et al., 2015), a limit strongly tied to the star's metallicity. Stellar evolution forecasts a population of $10^8 - 10^{10}$ such black holes in the Milky Way (van den Heuvel, 1992). Since Cygnus X-1's 1970 discovery (Webster and Murdin, 1972), finding stellar-mass black holes has centered on spotting compact objects in X-ray binaries with masses surpassing neutron star limits. Over 50 X-ray binaries are now considered candidates, and with LIGO's recent implementation, fresh detection methods are being explored (Abbott et al., 2016).

Astronomical observations reveal that in a galaxy's center, especially in large and medium-sized ones, a substantial mass is concentrated within a small volume (Kormendy and Richstone, 1995). The situation is less certain for small galaxies, where some may possess central masses while others might not (Ferrarese et al., 2006; Gallo et al., 2008). In the case of the Milky Way, studying star orbits near its center indicates a mass of roughly $M \approx 4 \times 10^6 M_{\odot}$ within a radius less than $R < 0.01\text{pc}$ (Ghez et al., 2005; Boehle et al., 2016). This substantial mass in such a confined space defies explanations involving neutron star clusters or brown dwarfs, leading to the natural inference of a supermassive black hole's presence (Maoz, 1998). Similar findings arise in other galaxies like NGC4258, supporting the idea that these massive black hole

systems have masses ranging from $M \approx 10^5$ to $10^{10}M_{\odot}$. While we anticipate stellar-mass black holes forming from massive star collapses, the formation process of supermassive black holes remains unclear. Although one might hypothesize that they grow through gravitational capture of objects like stars, the presence of $10^{10}M_{\odot}$ objects in distant galaxies when the universe was just 1Gyr old challenges this notion (Wu et al., 2015). They might have emerged from the collapse of massive primordial clouds, mergers of multiple black holes, or even super-Eddington accretion phases, as some models suggest (Madau et al., 2014). Yet, the precise formation mechanism remains a mystery.

A natural question that arises when studying supermassive black holes is how to measure their mass. As their origin is unknown, estimating their mass is challenging. To accomplish this, the $M - \sigma$ relation is currently employed. This relation is an empirical correlation between the stellar velocity dispersion of the galactic bulge and the mass M of the supermassive black hole at the center of the galaxy. It was first introduced in 1999 by Merritt (1999) and is sometimes referred to as the Faber-Jackson law for black holes. The relation is given by

$$\frac{M_{BH}}{10^8 M_{\odot}} \approx A \left(\frac{\sigma}{200 \text{km}^{-1}} \right)^{\alpha}, \quad (1.0.1)$$

where the scaling values are chosen to correspond to typical SMBH masses and velocity dispersions in galaxies, with parameters having values of $A \sim 3$ and $\alpha \sim 4 - 6$. The precise value of α depends on the sample of investigated galaxies; different authors suggest diverse values such as $\alpha = 4.24 \pm 0.41$ (Gültekin et al., 2009), $\alpha = 4.8 \pm 0.5$ (Ferrarese and Merritt, 2000), and $\alpha = 5.64$ (McConnell and Ma, 2013).

Over the las decades, significant efforts have been dedicated to the detection of black holes. The Event Horizon Telescope (EHT) ¹ recently achieved a major breakthrough by capturing the first direct images of SMBH. The first image, focused on visualizing the probable black hole at the center of the M87 galaxy (Collaboration et al., 2019), revealed a persistent, bright ring with a diameter of approximately 40 micro-arcseconds, in agreement with the predicted photon orbit around the "shadow" of this black hole. Another image, obtained by the

¹Here you can find the project: [Event horizon project](#)

EHT, unveiled the supermassive black hole Sgr A* (Markoff et al., 2022) at the heart of our galaxy. This image displayed a compact emission region with a bright, thick ring in the center, which has a diameter of around 51.8 micro-arcseconds and a slight brightness asymmetry. These remarkable achievements not only confirm previous predictions but also serve as crucial tests of general relativity, offering new opportunities to study these objects in the strong-field regime. Studies of the strong field tests (Gair et al., 2013; Yunes and Siemens, 2013) suggest that astrophysical BHs are fully described by the Kerr solution. However, BHs do not exist in a perfect vacuum and therefore are not fully axisymmetric, but are capable of evolving with time.

Although General Relativity (GR) appears to be a good theory for describing gravity, there are experimental and theoretical reasons to suggest that an extension beyond GR is needed. For instance, GR fails to predict the accelerating expansion of the universe without incorporating dark energy. In strong gravitational fields, GR predicts black hole (BH) solutions with singularities - regions of infinite density and zero volume within the horizon, where geometric quantities such as the Riemann tensor diverge. Hence, a more comprehensive theory is required to fully describe these regions and resolve the singularities.

To address these limitations of GR, there is a need for a more realistic solution, such as the parametric forms of the Kerr metric or solutions to modified gravity theories. This thesis focuses on exploring these possibilities by studying the properties of black holes described by the Kerr-Like metric (Johannsen, 2013a), which is a general space-time that covers both possibilities and is better described in a later section (2.5) and some black hole solutions beyond Einstein's gravity.

To study the properties of BHs in deviant Kerr spacetimes such as the Kerr-Like spacetime, ray tracing can be employed to obtain realistically simulated images of the accretion disk around the black hole, as well as its shadow. For several years, scientists have been intrigued by the appearance of these objects, particularly how light behaves around them. Luminet (1979) investigated the appearance of a thin accretion disk around a Schwarzschild black hole and introduced the concept of a "black hole shadow" for the first time. The shape of this shadow depends, in principle, on the spin parameter, mass,

and the observer's line-of-sight inclination towards the black hole or its specific geometry (a topic we'll delve into later in this study). Studies of the appearance of the black hole at the center of our galaxy have been conducted by [Falcke et al. \(1999\)](#), including ray tracing algorithms to quantify observed spectra with the intention of inferring parameters like its spin ([Davis and Hubeny, 2006](#); [Li et al., 2005](#); [Dauser et al., 2010](#)). It is also possible to use GRMHD simulations to complement ray tracing studies, simulations thoroughly examined by authors such as [De Villiers and Hawley \(2003\)](#); [Gammie et al. \(2003\)](#); [Broderick \(2006\)](#); [Dexter and Agol \(2009\)](#), where authors like ([Schnittman et al., 2006](#); [Noble and Krolik, 2009](#); [Dexter and Fragile, 2011](#); [Noble et al., 2011](#); [Kulkarni et al., 2011](#)) include variability and radiative efficiency properties. Leveraging advancements in this field, studies have also been conducted to compare these simulations with observations of Sgr A* ([Noble et al., 2007](#); [Dexter et al., 2009](#); [Chan et al., 2015](#); [Gold et al., 2017](#)) and M87 ([Dexter et al., 2012](#); [Mościbrodzka et al., 2016](#)). These investigations have focused on quantifying and understanding shadow properties, as well as the photon ring around these objects, and comprehending the potential features that can be expected in observations of SMBHs ([Roelofs et al., 2019](#); [Bronzwaer et al., 2021](#); [Bandyopadhyay et al., 2021, 2023](#)). In recent years, numerous ray-tracing software have been developed by authors such as [Vincent et al. \(2011\)](#); [Dexter \(2016\)](#); [Bronzwaer et al. \(2018\)](#). In particular, for this study, the Raptor I code ² was used, which is capable of using arbitrary spacetimes and also to characterize the properties of these images, the definitions of displacement, diameter, and asymmetry by [Johannsen \(2013a\)](#). These definitions were used to quantitatively describe the shadow of black holes and possible effects that could be measured in an observation.

This thesis presents a wide range of radiative transport simulations in the environment of a supermassive black hole (SMBH). We employ a HARM-type plasma model with mass and distance parameters similar to those of the SMBH in *M87** and a spin parameter of $a = 0.9375M$. Additionally, we apply the same spin value to the SMBH in *SgrA**, introducing changes in input parameters to create a more realistic model, following the parameters introduced by ([Mościbrodzka et al., 2009](#)). Furthermore, we conduct

²Which can be found at:[RAPTOR](#)

simulations using a thin accretion disk model based on (Shakura and Sunyaev, 1973; Novikov and Thorne, 1973) for a black hole with a mass of $10M_{\odot}$ to assess the properties of BHs in this scenario. We calculate properties related to the photon ring following the methodology of Johannsen (2013a) for a Kerr-like metric and explore how they vary with the free parameters of this spacetime. Additionally, we consider the effects of the plasma around the black hole as determined by the corresponding disk model. We test various ranges of first-order metric parameters and derive specific values for the diameter, asymmetry, and displacement of the photon ring in these simulations. These results are subsequently compared with those obtained by Johannsen and with radiative transport simulations for the Kerr metric. We also observe minor effects caused by non-circular photon orbits around the black hole, as well as their implications.

Moreover, we examine the effects of specific deviations introduced by solutions from modified gravity theories, such as the slowly rotating Chern-Simons solution. Additionally, we obtain a slowly rotating black hole solution for the α' -corrected theory and demonstrate its separability under the Hamilton-Jacobi equations as a preliminary step towards studying its shadow in future projects.

This thesis is presented as follows: an overview of black holes and their geometry is given together with the presentation of the Kerr-Like metric in Chapter 2. Chapter 3 presents the codes and model used to perform the simulations, as the methods utilized to characterize the black hole shadow. In Chapters 4 the results are given. The main conclusions and a discussion is presented in Chapter 5.

Chapter 2

About black holes

In this chapter, we will focus on the fundamental principles of black holes and their properties. Starting with Einstein's theory of General Relativity, we will delve into the mathematical solutions for black holes developed by Schwarzschild and Kerr. We will explore the concepts of the event horizon and the characterization of black holes based on their mass, spin, and other key parameters. By the end of this chapter, we will concentrate on the description of the Kerr-Like metric, its construction, and how it can be studied through the geodesic equation to better understand its properties.

2.1 Compact Objects

I would like to start with a simple and general description of compact objects. Some examples of these objects are white dwarfs, neutron stars, and black holes. They all share a common origin known as stars (at least on a stellar scale). Basically, these objects are formed when a star exhausts its nuclear fuel, causing the loss of its hydrostatic equilibrium. The internal thermonuclear pressure is no longer strong enough to counteract the gravitational collapse. As a result, the star sheds its outermost layer through an explosion known as a supernova and collapses its innermost material into one of the three aforementioned objects, depending on the star's initial mass and the magnitude of the collapse. Among the compact objects, white dwarfs are the least massive ones, formed from the remnants of low to medium-mass stars. Their masses range from

Table 2.1.1: Comparison of compact objects with a normal star (Sun) extracted from Shapiro and Teukolsky (2008).

Object -	Mass (M_{\odot})	Radius (R_{\odot})	Density (g/cm^3)	Surface potential (GM/Rc^2)
Sun	$1.98 \times 10^{30} \text{ kg} \sim M_{\odot}$	$10^9 \text{ m} \sim R_{\odot}$	1	10^{-6}
White dwarf	$\leq M_{\odot}$	$\sim 10^{-2} R_{\odot}$	$\leq 10^7$	$\sim 10^{-4}$
Neutron star	$1.5 - 3.0 M_{\odot}$	$\sim 10^{-5} R_{\odot}$	$\leq 10^{15}$	$\sim 10^{-1}$
Black hole	few to billion M_{\odot}	$2GM/c^2$	$\sim M/R^3$	~ 1

0.1 to 1.4 times that of the Sun. Neutron stars are more massive, resulting from the collapse of massive stars. They have densities so high that electrons and protons combine to form neutrons. Neutron stars typically have masses of 1.4 to 3 times that of the Sun, packed into a radius of about 10 kilometers. Black holes are the most massive objects, formed from extremely massive star remnants. Their gravity is so strong that nothing, not even light, can escape. Black holes can have a range of masses, from a few solar masses to billions. A most clear comparison is shown in Table (2.1.1).

In contrast to ordinary stars, compact objects are a clear example of matter under extreme conditions. When compared to stars of similar mass, compact objects have much smaller radii, making them denser and possessing extremely strong gravitational fields on their surfaces. Therefore, the study of these objects requires advanced physical knowledge, such as General Relativity. Even in the case of white dwarfs, where Newtonian gravity may appear sufficient for their description, General Relativity is necessary to study their stability.

2.2 General Relativity

The concept of gravity arose more than two thousand years ago with ancient Greeks such as Aristotle, who believed that all objects in the universe fell towards the earth because it was the center of the universe, or Archimedes, who discovered the center of gravity of a triangle. Although these thoughts forged the basis of the concept of gravitation, it was not until 1687, when Sir Isaac Newton published his work "Principia Mathematica", that the mathematical and physical foundations of the classical theory of gravity were established. In

this work, Newton described that all bodies in the universe exert an attractive force on all other bodies, called gravity. For many years, the Newtonian concept of gravity was widely accepted by the scientific community of the time. However, this understanding was fundamentally transformed in 1915 with the publication of Einstein's theory of general relativity, changing our perception of the nature of gravity.

Inspired by Faraday and Maxwell's development of the electromagnetic field, Einstein realized that gravity, previously thought of as an invisible force by Newton, was not a force at all, but instead a manifestation of a field similar to the electromagnetic field. This field was not an entity that existed in space but rather was space itself. With this newfound understanding and building upon his previous work on the theory of special relativity in 1905, Einstein established several fundamental principles, such as the principle of relativity, which states that the laws of physics are identical in all inertial frames of reference. He also established the constancy of the speed of light for all observers and introduced the concepts of time dilation and length contraction. Time dilation states that time passes differently for two observers in relative motion, with an observer in motion perceiving time to move more slowly than an observer at rest, while length contraction posits that lengths appear shorter for an object in motion relative to an observer at rest.

Motivated by these ideas and realizing that his theory of special relativity was not in line with Newtonian physics' perception of gravity, Einstein dedicated himself to creating a new theory of gravity, founded on two fundamental postulates:

The first postulate, known as the weak equivalence principle, states that all objects, regardless of their composition and mass, will be affected by the same acceleration under a gravitational field.

The second postulate, known as strong equivalence principle, states that locally, the effects of gravity and acceleration are indistinguishable. This means that in a small region of spacetime, an observer cannot tell whether a body in the system is accelerating or is under the influence of an external gravitational field.

These two principles are the most fundamental ingredients of Einstein's theory,

known as **General Relativity** (GR). There is a wide variety of experiments that confirm these two principles, some of which are (v. Eötvös et al., 1922; Roll et al., 1964; Schlamminger et al., 2008) for the weak equivalence principle and (Archibald et al., 2018; Voisin et al., 2020) for strong equivalence principle.

Under these two postulates, the mathematical construction of the theory can be carried out. Einstein based his theory on the idea of geometrizing the gravitational interaction, meaning that spacetime was curved under the effects of a gravitational field. Thus, inspired by the mathematics and geometry developed by Bernhard Riemann, he described his theory considering spacetime as a curved (pseudo-Riemannian) manifold with a line element $ds^2 = g_{\mu\nu}dx^\mu dx^\nu$, where the metric $g_{\mu\nu}$ and the transformations between the coordinates systems, are Lorentzian type.

As the geometry in this theory is Riemannian and does not exhibit torsion (since Einstein did not construct it that way), both metric properties and affine properties are completely determined by a single object, the metric.

The metric is the dynamical field of the theory, and it is useful to define some mathematical objects associated with it to better understand the following discussion about the solutions. The **connection**, which in this case is described by the Christoffel symbols, is defined as

$$\Gamma^\lambda_{\mu\nu} = \frac{1}{2}g^{\lambda\rho}(\partial_\mu g_{\nu\rho} + \partial_\nu g_{\mu\rho} - \partial_\rho g_{\mu\nu}), \quad (2.2.1)$$

where $g_{\mu\nu}$ is the covariant metric and $g^{\lambda\rho}$ is the contravariant metric.

As GR is a theory built on a curved manifold that seeks to be invariant under arbitrary coordinate transformations, it must be invariant under diffeomorphisms. Therefore, the derivative used to operate mathematically must satisfy this condition. The usual partial derivative is not an option since it is not invariant under diffeomorphisms. In response to this, Einstein introduced the concept of the covariant derivative of a tensor in his theory. This type of derivative is constructed in a way that preserves the tensor's covariance under coordinate transformations and is defined as follows

$$\nabla_\mu \zeta^\lambda = \partial_\mu \zeta^\lambda + \Gamma^\lambda_{\mu\nu} \zeta^\nu, \quad (2.2.2)$$

where ξ^λ is an arbitrary contravariant tensor and $\Gamma^\lambda_{\mu\nu}$ is the connection of the theory. Similarly, it is possible to define the covariant derivative acting on an arbitrary covariant tensor.

On the other hand, if one studies the commutativity property of the second covariant derivatives of an arbitrary tensor, it is concluded that these do not commute, and the following property is obtained

$$[\nabla_\mu, \nabla_\nu]\xi^\lambda = \nabla_\mu \nabla_\nu \xi^\lambda - \nabla_\nu \nabla_\mu \xi^\lambda = R^\lambda_{\rho\mu\nu} \xi^\rho, \quad (2.2.3)$$

where $R^\lambda_{\rho\mu\nu}$ is the Riemann curvature tensor defined as

$$R^\lambda_{\rho\mu\nu} := \partial_\mu \Gamma^\lambda_{\nu\rho} - \partial_\nu \Gamma^\lambda_{\mu\rho} + \Gamma^\lambda_{\mu\sigma} \Gamma^\sigma_{\nu\rho} - \Gamma^\lambda_{\nu\sigma} \Gamma^\sigma_{\mu\rho}. \quad (2.2.4)$$

It is also useful to define, from the curvature tensor, the Ricci tensor, given by contracting two indices of the Riemann tensor

$$R_{\rho\nu} := R^\mu_{\rho\mu\nu}, \quad (2.2.5)$$

and the Ricci scalar, given by contracting the Ricci tensor with the metric, that is

$$R := R_{\rho\nu} g^{\rho\nu}. \quad (2.2.6)$$

With these mathematical ingredients capable of describing the geometry of curved spacetime and the inclusion of the interaction between matter and fields in this spacetime, Einstein constructed the equation

$$G_{\mu\nu} := \frac{8\pi G}{c^4} T_{\mu\nu} \quad (2.2.7)$$

known as the field equation of the general theory of relativity, where the left-hand side of the equation is given as $G_{\mu\nu} = R_{\mu\nu} - \frac{1}{2}g_{\mu\nu}R$ and purely describes the geometry of spacetime. The right-hand side of the equation includes the energy-momentum tensor $T_{\mu\nu}$, which describes the distribution and energy of matter with which these fields interact.

The field equations in general are a complex system of highly non-linear differential equations. When solved, they result in a metric that can describe the effects of a certain gravitational field under the matter that interacts with it.

A useful equation to define in order to observe these effects, and for the subsequent physical discussion in the following sections, is the geodesic equation. It is a mathematical description of the weak equivalence principle and can be expressed as follows

$$\frac{d^2 x^\mu}{d\lambda^2} + \Gamma^\mu_{\rho\sigma} \frac{dx^\rho}{d\lambda} \frac{dx^\sigma}{d\lambda} = 0, \quad (2.2.8)$$

where $\Gamma^\mu_{\rho\sigma}$ is the Christoffel connection and λ is the affine parameter. In the next section, we will discuss the Schwarzschild solution and focus on how it was a fundamental piece in developing the concept of black holes.

2.3 Schwarzschild solution

The first exact analytical solution of Einstein's field equations was developed by the German astronomer Karl Schwarzschild in 1916. Schwarzschild developed his solution to describe the gravitational field surrounding a spherically symmetric mass at rest i.e with spherical symmetry and independent of time.

The fact that it has spherical symmetry implies that in this spacetime there are three spatial Killing vectors, which obey the algebra of the rotation group $SO(3)$.

Starting from the preservation of these symmetries and the fact that in a 4-dimensional Riemannian space-time it is possible to define coordinates as $x^\mu = (t, r, \theta, \phi)$, such that the line element can be written as

$$ds^2 = -F(r, t)dt^2 + G(r, t)dr^2 + r^2 \left[d\theta^2 + \sin^2 \theta d\phi^2 \right], \quad (2.3.1)$$

where $F(r, t)$ and $G(r, t)$ are metric functions that depend on the radial and temporal coordinates, and where the rest of the line element corresponds to that of the 2-sphere.

A convenient and possible ansatz for writing these two metric functions is the following:

$$F(r, t) = e^{f(r, t)}, \quad (2.3.2)$$

$$G(r, t) = e^{g(r, t)}, \quad (2.3.3)$$

such that the line element becomes,

$$ds^2 = -e^{f(r, t)} dt^2 + e^{g(r, t)} dr^2 + r^2 \left[d\theta^2 + \sin^2 \theta d\phi^2 \right], \quad (2.3.4)$$

where it is clear to note that the covariant metric tensor only has terms on its diagonal and can be written as

$$g_{tt} = -e^{f(r, t)}, \quad (2.3.5)$$

$$g_{rr} = e^{g(r, t)}, \quad (2.3.6)$$

$$g_{\theta\theta} = r^2, \quad (2.3.7)$$

$$g_{\phi\phi} = r^2 \sin^2 \theta. \quad (2.3.8)$$

Similarly, the contravariant form of this tensor is

$$g^{tt} = -e^{-f(r, t)}, \quad (2.3.9)$$

$$g^{rr} = e^{-g(r, t)}, \quad (2.3.10)$$

$$g^{\theta\theta} = \frac{1}{r^2}, \quad (2.3.11)$$

$$g^{\phi\phi} = \frac{1}{r^2 \sin^2 \theta}. \quad (2.3.12)$$

Using this form of the metric tensor and introducing it into the field equations (2.2.7) for a spherically symmetric object in vacuum, i.e., for

$$R_{\mu\nu} - \frac{1}{2} g_{\mu\nu} R = 0 \quad (2.3.13)$$

with $T_{\mu\nu} = 0$, the equations reduce to

$$0 = \frac{1}{r^2} - \frac{1}{r} \frac{\partial g(r,t)}{\partial r} - \frac{e^{g(r,t)}}{r^2}, \quad (2.3.14)$$

$$0 = \frac{\partial g(r,t)}{\partial t}, \quad (2.3.15)$$

$$0 = \frac{1}{r^2} - \frac{1}{r} \frac{\partial f(r,t)}{\partial r} - \frac{e^{g(r,t)}}{r^2}, \quad (2.3.16)$$

$$0 = e^{-g(r,t)} \left[\frac{\partial^2 f(r,t)}{\partial r^2} + \frac{1}{2} \left(\frac{\partial f(r,t)}{\partial r} \right)^2 - \frac{1}{2} \frac{\partial g(r,t)}{\partial r} \frac{\partial f(r,t)}{\partial r} \right. \\ \left. + \frac{1}{r} \left(\frac{\partial f(r,t)}{\partial r} - \frac{\partial g(r,t)}{\partial r} \right) \right] - e^{-f(r,t)} \left[\frac{\partial^2 g(r,t)}{\partial t^2} \right. \\ \left. - \frac{1}{2} \frac{\partial g(r,t)}{\partial t} \frac{\partial f(r,t)}{\partial t} + \frac{1}{2} \left(\frac{\partial g(r,t)}{\partial t} \right)^2 \right]. \quad (2.3.17)$$

We note here that the last equation does not provide additional information.

From equation (2.3.15), it is possible to notice that $g(r,t)$ is independent of time, that is, $g(r,t) = g(r)$. On the other hand, if we subtract equation (2.3.14) from equation (2.3.16), we obtain

$$\frac{\partial}{\partial r} [f(r,t) + g(r,t)] = 0, \quad (2.3.18)$$

such that

$$f(r,t) + g(r,t) = H(t) \quad (2.3.19)$$

with $H(t)$ a function dependent only on time. And as $g(r,t) = g(r)$, we have that

$$f(r,t) = H(t) - g(r). \quad (2.3.20)$$

As a consequence of this, we can choose $H(t) = 0$, without losing generality of the solution, so that $f(r,t) = f(r) = -g(r)$.

Given this, we observe that the components of the proposed metric do not depend on time. If we then replace this result in equation (2.3.14), we notice that it becomes identical to equation (2.3.16). Therefore, using (2.3.14) and returning to the original variables with $e^{f(r)} = F(r)$, we obtain the equation

$$r \frac{\partial F(r)}{\partial r} + F(r) - 1 = 0. \quad (2.3.21)$$

And if we also make a change of variable of the form $u(r) := F(r) - 1$, the equation is reduced to

$$r \frac{\partial u(r)}{\partial r} + u(r) = 0 \quad (2.3.22)$$

and when solved, we obtain

$$u(r) = -\frac{C_1}{r}, \quad (2.3.23)$$

where C_1 is a constant, which for future convenience we will choose as $C_1 = 2m$, where also m is a constant with dimensions of distance.

Therefore, the solution would be

$$F(r) = e^{f(r)} = 1 - \frac{2m}{r}, \quad (2.3.24)$$

$$G(r) = e^{-f(r)} = \frac{1}{1 - \frac{2m}{r}}. \quad (2.3.25)$$

Then, the line element of the Schwarzschild solution can be written as

$$ds^2 = - \left(1 - \frac{r_s}{r}\right) c^2 dt^2 + \frac{dr^2}{\left(1 - \frac{r_s}{r}\right)} + r^2 \left[d\theta^2 + \sin^2 \theta d\phi^2 \right], \quad (2.3.26)$$

where $r_s := 2m = 2GM/c^2$, in which $m := GM/c^2$, with M the physical mass of the central object, G the universal gravitational constant, and c the speed of light. Usually, we put $G = 1$ and $c = 1$ to use the geometric units.

Here **Birkhoff's theorem** comes into play, stating that *any solution to the vacuum field equations of Einstein's theory with spherical symmetry must have a stationary and asymptotically flat exterior. As a result, the spacetime outside a static, spherically symmetric object can be described by the Schwarzschild metric.*

2.3.1 Schwarzschild radius

The Schwarzschild solution given by the line element (2.3.26) is physically interpreted as the description of a gravitational field outside $r > r_0$ for a spherically symmetric star of radius r_0 . However, this solution presents a problem for $r = r_s = 2m$, where it seems to explode for this particular value of the radius r , thus a "singularity in the metric" appears.

This particular point for r in the chosen coordinate system is known today as the Schwarzschild radius and is denoted by $r_s = 2GM/c^2$. Each body associated with a solution of this type has a characteristic distance given by this radius. For example, if we approximate the Sun as a spherically symmetric object and associate it with the Schwarzschild solution, we can obtain that this radius is approximately

$$r_{s_{\odot}} = \frac{2GM_{\odot}}{c^2} \approx 3 \text{ km}, \quad (2.3.27)$$

a radius for which the matter distribution that forms the Sun surpasses it by far, that is, the radius of the Sun is much larger than its associated Schwarzschild radius, or $r_{\odot} > r_{s_{\odot}}$. Therefore, for this type of object, there is no problem with the singularity in the metric, since $r > r_0$ and $r_0 > r_s$.

The problem with this "singularity" appears when we study compact objects as described in (2.1), particularly for objects where their radius is $r_0 < r_s$.

The word "singularity" is used in quotation marks, since in this context we do not yet know if it really corresponds to a singularity of the curvature, or if it is only a singularity of the coordinate system, because one definition differs from the other.

A *coordinate system singularity* is a particular point that explodes to infinity in a given coordinate system, and which can be eliminated by the appropriate change of coordinates. On the other hand, a *curvature singularity* is a given point in the manifold that explodes to infinity and which is not removable by an appropriate change of coordinates.

To mathematically differentiate an intrinsic singularity of the geometry (or curvature) from an apparent singularity given by the coordinate system, it

is necessary to use the calculation of invariant quantities in the theory, i.e., scalars, the simplest case is the calculation of the Ricci scalar, given by equation (2.2.6). However, this scalar is always $R = 0$ for any solution of the Einstein field equations in vacuum. Hence, it becomes necessary to utilize other scalars obtained by contracting the curvature tensor. If a scalar diverges at a particular point, it indicates that this point is a singularity of the geometry.

In the case of the Schwarzschild metric, the Kretschmann scalar is employed, and it is

$$R_{\mu\nu\rho\sigma}R^{\mu\nu\rho\sigma} = \frac{48m^2}{r^6}. \quad (2.3.28)$$

Therefore, if we substitute the value of the Schwarzschild radius $r = 2m$ into the equation, we note that it does not diverge, so this value is not a singularity of the geometry. It can also be verified that none of the scalars present in the theory diverge at the Schwarzschild radius. On the contrary, if we introduce $r = 0$ into the equation, we can notice that this value is a singularity of the geometry.

2.3.2 Event Horizon

While the sphere located at $r_s = 2m$ is not a singularity of the curvature, it remains an interesting limit to study, commonly known as the *event horizon* or simply the *horizon*. Knowing this, we still need to understand what happens at this horizon. Although we are aware that it is not a singularity of the curvature, it poses a problem in the coordinates used to describe the Schwarzschild metric, which prevents us from fully understanding what occurs when $r \leq r_s$.

To understand the behavior of this spacetime near the horizon, it is best to study what's happening with the metric in its vicinity, that is, by evaluating

$$r = 2m + \varepsilon, \quad (2.3.29)$$

where $0 < \varepsilon \ll 2m$. Then, the line element of the Schwarzschild metric is given by

$$ds^2 = -\frac{\varepsilon}{2m}dt^2 + \frac{2m}{\varepsilon}d\varepsilon^2 + (2m)^2d\Omega^2, \quad (2.3.30)$$

where $d\Omega^2 = d\theta^2 + \sin^2\theta d\phi^2$ represents the line element of the S^2 sphere with a radius of $2m$, and the remaining part of the line element corresponds to Lorentzian geometry in $d = 1 + 1$ dimensions. If we focus our attention on the first part of the line element (i.e., the Lorentzian part), it can be written as

$$ds^2 = -\left(\frac{\rho}{4m}\right)^2 dt^2 + d\rho^2, \quad (2.3.31)$$

where

$$\rho^2 = 8m\varepsilon.$$

This metric is known as the *Rindler space*, which can be transformed back into Minkowski space through a simple transformation:

$$T = \rho \sinh\left(\frac{t}{4m}\right) \quad X = \rho \cosh\left(\frac{t}{4m}\right) \quad (2.3.32)$$

that converts the line element into

$$ds^2 = -dT^2 + dX^2. \quad (2.3.33)$$

The coordinates (2.3.32) are the coordinates experienced by an observer undergoing constant acceleration.

Considering that $\rho > 0$ corresponds to the exterior of the horizon, with $-\infty < t < +\infty$, we have that in Minkowski space it corresponds to the region $X > |T|$. We can also analyze the behavior of this metric at the horizon itself, where $\rho = 0$, so in Minkowski space $X = T = 0$ maps to its origin. Thus, if $t \rightarrow \infty$ and $\rho \rightarrow 0$ while keeping the combination $\rho e^{\pm t/4m}$ fixed, the horizon corresponds to the lines,

$$r = 2m \Rightarrow X = \pm T. \quad (2.3.34)$$

This implies that the event horizon of a black hole is not a timelike surface; instead, it is a null surface.

From the metric (2.3.33), we notice that it makes perfect sense for all $X, T \in \mathbb{R}$ and that there is nothing suspicious about the point $X = \pm T$. However, in the

latter case, it can be observed that the horizon presents interesting properties. To study them, it is useful to have a global view of this type of coordinates for a black hole.

The first step to do this is to introduce a new radial coordinate called r_* , such that

$$dr_*^2 = \left(1 - \frac{2m}{r}\right)^{-2} dr^2, \quad (2.3.35)$$

where

$$r_* = r + 2m \log \left(\frac{r - 2m}{2m} \right). \quad (2.3.36)$$

Here it can be seen that the region outside the horizon, i.e., $2m < r < +\infty$, is mapped to $-\infty < r_* < +\infty$ in the new radial coordinate. Also known as the *tortoise coordinate*, due to its slow change in r as r_* varies when approaching the horizon.

This type of coordinate is useful for studying the path of light rays traveling in the radial coordinate, so if we consider null radial geodesics, it satisfies that

$$ds^2 = 0 \Rightarrow \frac{dr}{dt} = \pm \left(1 - \frac{2m}{r}\right) \Rightarrow \frac{dr_*}{dt} = \pm 1. \quad (2.3.37)$$

Therefore, the radial geodesics are given by

$$t \pm r_* = \text{constant}, \quad (2.3.38)$$

where the plus sign corresponds to ingoing geodesics (as t increases, r_* must decrease) and the minus sign corresponds to outgoing geodesics.

If we introduce

$$v = t + r_*, \quad (2.3.39)$$

$$u = t - r_* \quad (2.3.40)$$

as the null coordinates, we can construct the well-known ingoing and outgoing *Eddington-Finkelstein coordinates*.

For our study interest, we will focus only on the *ingoing* coordinates as they describe what we now know as black holes for the Schwarzschild metric. Using the transformation (2.3.39), we can construct

$$dt = dv - dr_* = dv - \left(1 - \frac{2m}{r}\right)^{-1} dr. \quad (2.3.41)$$

Substituting this into the Schwarzschild metric (2.3.26), we obtain

$$ds^2 = - \left(1 - \frac{2m}{r}\right)^{-1} dv^2 + 2dvdr + r^2(d\theta^2 + \sin^2\theta d\phi^2), \quad (2.3.42)$$

the line element for the Schwarzschild metric in the *ingoing Eddington-Finkelstein coordinates*. Here we can see that the term dr^2 disappears, and there are no longer singularities at $r = 2m$, although dv^2 changes sign for values of $r < 2m$. It might appear that the metric is still problematic at these values, but simply calculating the determinant of it reveals that this is not the case, as

$$\det(g) = -r^4 \sin^2\theta, \quad (2.3.43)$$

where we note that the cross-term $dvdr$ prevents the metric from becoming degenerate at the horizon, and the signature remains Lorentzian for all values of r .

On the other hand, the Schwarzschild metric written as in (2.3.26) is time-independent since it has a timelike Killing vector $K = \partial_t$. Similarly, in the Eddington-Finkelstein coordinates, this Killing vector ($K = \partial_v$) also exists, but it is no longer timelike ($g_{vv} < 0$) throughout its domain, as it becomes spacelike inside the horizon (i.e. $g_{vv} > 0$). This means that the complete geometry of the black hole is not time-independent.

Now, if we analyze the behavior of the light rays that escape from the black hole using the coordinate transformation (2.3.40):

$$u = t - r_* = \text{constant} \quad (2.3.44)$$

using $v = t + r$ to eliminate t in the outgoing null geodesic, it is satisfied that $v = 2r + \text{constant}$. If $r > 2m$, using the tortoise coordinates, we obtain:

$$v = 2r + 4m \log \left(\frac{r - 2m}{2m} \right) + \text{constant}. \quad (2.3.45)$$

Here, it is clear that the logarithmic term behaves poorly for values of $r < 2m$. However, this can be solved by taking the absolute value of the argument in the definition of r_* , such that:

$$r_* = r + 2m \log \left| \frac{r - 2m}{2m} \right|. \quad (2.3.46)$$

This means that r_* has multiple valid values for both the exterior and interior of the horizon, where r_* takes values of $r_* \in (-\infty, +\infty)$ and $r_* \in (-\infty, 0)$, respectively. Moreover, $r_* = 0$ represents the singularity. The outgoing geodesics inside the horizon have the form:

$$v = 2r + 4m \log \left(\frac{2m - r}{2m} \right) + \text{constant}. \quad (2.3.47)$$

We also note that for $r = 2m$, the term dv^2 disappears, hence this surface is itself a null geodesic. Therefore, the horizon is a null surface.

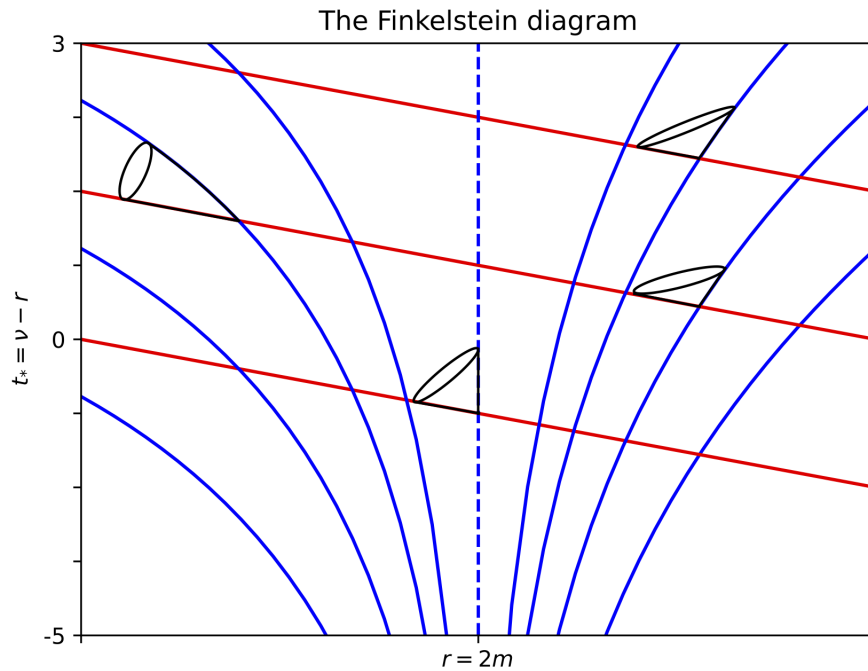


Figure 2.3.1: The Finkelstein diagram for ingoing Eddington-Finkelstein coordinates.

Finally, this information can be better illustrated by using a *Finkelstein diagram*, where it is easier to see the behavior inside and outside the horizon. In the diagram shown in Fig. (2.3.1), light rays traveling on null geodesics for ingoing Finkelstein coordinates are represented. The axes of the diagram are the time t_* and the radius r , related by the expression:

$$v = t + r_* = t_* + r. \quad (2.3.48)$$

In the diagram, the incoming null geodesics are represented by red lines, and the outgoing null geodesics are represented by blue lines. Additionally, the dashed line represents the horizon boundary at $r = 2m$. Inside the horizon, the outgoing geodesics inevitably move towards the singularity at $r = 0$, whereas outside the horizon, the outgoing geodesics move away from the horizon and escape to infinity. In the case of incoming null geodesics, the diagram is designed to represent them as constant lines traveling at a 45 angle.

Furthermore, light cones can be represented in the Finkelstein diagram with

the intention of understanding the behavior of massive particles near the horizon. These can be constructed at the intersections of the outgoing and incoming curves. We can observe that outside the horizon, the inclination of the top part of the light cones becomes more vertical as they move away from the event horizon. This means that a particle near the vicinity of the horizon but outside of it can escape towards infinity. On the other hand, light cones inside the horizon have an opposite inclination, always pointing towards the singularity. This indicates that once the horizon limit is crossed, the trajectory will inevitably fall towards the singularity.

This behavior of objects near the event horizon is what gives these objects the name "black hole," as beyond the horizon, nothing, not even light, can escape from it. Additionally, this diagram can give us an idea of what an observer outside the black hole would see if they witnessed a companion entering it. As the companion passes the horizon, they would not notice anything strange and would continue on their path towards the singularity. However, the external observer would not be able to see this because the light rays emitted by the companion would gradually slow down as they approach the horizon. The observer would perceive a static image of their companion, which, over time, would gradually experience **redshift** given the infinite redshift surface at $r = 2m$ and that $g_{tt} \rightarrow 0$ as we approach the horizon, by gravitational time dilation, which can also be expressed mathematically as

$$\frac{\Delta\tau_1}{\Delta\tau_2} = \frac{\sqrt{1 - \frac{2m}{r_1}}}{\sqrt{1 - \frac{2m}{r_2}}}, \quad (2.3.49)$$

where r_1 and r_2 are the positions of the two "static" observers.

Similarly, the outgoing Eddington-Finkelstein coordinates can be analyzed, but these would lead us to the concept of a white hole, which is not necessary to explore for the understanding of this study.

2.3.3 Bound orbits in Schwarzschild metric

Finally, to fully understand the Schwarzschild solution, it is beneficial to study the behavior of geodesics. Therefore, the first required ingredient is the

non-zero components of the Christoffel symbols, which are given by

$$\Gamma_{tr}^t = \frac{m}{r(r-2m)}, \quad (2.3.50)$$

$$\Gamma_{tt}^r = \frac{m(r-2m)}{r^3}, \quad (2.3.51)$$

$$\Gamma_{rr}^r = \frac{-m}{r(r-2m)}, \quad (2.3.52)$$

$$\Gamma_{\theta\theta}^r = -(r-2m), \quad (2.3.53)$$

$$\Gamma_{\phi\phi}^r = -(r-2m) \sin^2 \theta, \quad (2.3.54)$$

$$\Gamma_{r\theta}^\theta = \frac{1}{r}, \quad (2.3.55)$$

$$\Gamma_{\phi\phi}^\theta = -\sin \theta \cos \theta, \quad (2.3.56)$$

$$\Gamma_{r\phi}^\phi = \frac{1}{r}, \quad (2.3.57)$$

$$\Gamma_{\theta\phi}^\phi = \frac{\cos \theta}{\sin \theta}. \quad (2.3.58)$$

If they are used in the geodesic equation, the following 4 equations can be obtained, with the affine parameter λ ;

$$\frac{d^2 t}{d\lambda^2} + \frac{2m}{r(r-2m)} \frac{dr}{d\lambda} \frac{dt}{d\lambda} = 0, \quad (2.3.59)$$

$$\begin{aligned} \frac{d^2 r}{d\lambda^2} + \frac{m}{r^3} (r-2m) \left(\frac{dt}{d\lambda} \right)^2 - \frac{m}{r(r-2m)} \left(\frac{dr}{d\lambda} \right)^2 \\ - (r-2m) \left[\left(\frac{d\theta}{d\lambda} \right)^2 + \sin^2 \theta \left(\frac{d\phi}{d\lambda} \right)^2 \right] = 0, \end{aligned} \quad (2.3.60)$$

$$\frac{d^2 \theta}{d\lambda^2} + \frac{2}{r} \frac{d\theta}{d\lambda} \frac{dr}{d\lambda} - \sin \theta \cos \theta \left(\frac{d\phi}{d\lambda} \right)^2 = 0, \quad (2.3.61)$$

$$\frac{d^2 \phi}{d\lambda^2} + \frac{2}{r} \frac{d\phi}{d\lambda} \frac{dr}{d\lambda} + 2 \frac{\cos \theta}{\sin \theta} \frac{d\theta}{d\lambda} \frac{d\phi}{d\lambda} = 0. \quad (2.3.62)$$

These equations can be solved thanks to the numerous symmetries exhibited by the Schwarzschild solution.

The metric has 4 constants of motion for a free particle, which is due to having the same number of Killing vectors

$$K_\mu \frac{dx^\mu}{d\lambda} = \text{constant}. \quad (2.3.63)$$

Three of them are spatial due to their spherical symmetry, and one is due to temporal translations. Additionally, there is another constant that always appears for geodesics, which is written as

$$\tilde{c} = -g_{\mu\nu} \frac{dx^\mu}{d\lambda} \frac{dx^\nu}{d\lambda}. \quad (2.3.64)$$

For massive particles, when $\lambda = \tau$ (i.e., timelike curves), we have $\tilde{c} = -g_{\mu\nu} U^\mu U^\nu = +1$. For massless particles, $\tilde{c} = 0$, and for spacelike curves, $\tilde{c} = -1$.

Now, if we look at what the Killing vectors imply for the conserved quantities in the Schwarzschild metric, we notice that the symmetries indicate invariance under temporal translations and spatial rotations. Therefore, we can infer that there will be at least two Killing vectors associated with these quantities.

The conservation of spatial rotations leads to conservation of angular momentum (which has 3 Killing vectors, 2 for its directions and one for magnitude). Therefore, we can choose to work in the equatorial plane to simplify the calculations. If the particle is orbiting outside the plane, we can rotate the coordinate system until it is in the plane. Then, the two Killing vectors associated with the direction of angular momentum imply that

$$\theta = \frac{\pi}{2}, \quad (2.3.65)$$

such that the remaining two Killing vectors are $K = \partial_t$ representing energy and $L = \partial_\phi$ representing angular momentum magnitude, which lead us to the equations

$$\left(1 - \frac{2m}{r}\right) \frac{dt}{d\lambda} = E, \quad (2.3.66)$$

$$r^2 \frac{d\phi}{d\lambda} = L. \quad (2.3.67)$$

Together, these conserved quantities applied to equation (2.3.64) lead us to the equation

$$-E^2 + \left(\frac{dr}{d\lambda}\right)^2 + \left(1 - \frac{2m}{r}\right) \left(\frac{L^2}{r^2} + \tilde{c}\right) = 0, \quad (2.3.68)$$

which can be rewritten as

$$\frac{1}{2} \left(\frac{dr}{d\lambda} \right)^2 + V(r) = \frac{1}{2} E^2 \quad (2.3.69)$$

where

$$V(r) = \frac{1}{2} \tilde{c} - \tilde{c} \frac{m}{r} + \frac{L^2}{2r^2} - \frac{mL^2}{r^3}. \quad (2.3.70)$$

This is the effective potential of the Schwarzschild metric for particles moving along geodesics in a plane, where the first three terms have a Newtonian character and the last term represents the contribution of general relativity to the potential, which becomes significant for small values of r .

This potential serves to describe the types of possible orbits. There will be different values of $V(r)$ for different values of L . The general behavior of a particle will be to move along the potential until it reaches the "inflection point" where $V(r) = \frac{1}{2} E^2$, at which point its motion will change direction. In some cases, there is no inflection point, and the particle will remain in that motion. The particle can also remain in circular orbits, where r is constant and occurs when $dV/dr = 0$.

Therefore, by taking the derivative of the equation (2.3.70) with respect to r , we can find the radius for the circular orbit r_c via

$$\tilde{c} m r_c^2 - L^2 r_c + 3mL^2 \gamma = 0. \quad (2.3.71)$$

The circular orbit will be stable if the value of r corresponds to a minimum of the potential and unstable if it corresponds to a maximum. In general relativity, it is possible to find a circular orbit for massless particles at

$$r_c = 3m, \quad (2.3.72)$$

which is a maximum value for $V(r)$. Therefore, a photon can orbit indefinitely at this radius (known as the **photon radius** r_{ph}). However, any perturbation will cause it to either collapse to $r = 0$ or escape to $r = \infty$.

For massive particles, circular orbits are given by

$$r_c = \frac{L^2 \pm \sqrt{L^4 - 12m^2L^2}}{2m} \quad (2.3.73)$$

and depend solely on the value of L . For large values of L , there are two circular orbits, one stable and one unstable. As $L \rightarrow \infty$, the stable orbit grows and approaches the value of $r_c = L^2/m$, while the unstable orbit approaches the value of circular orbits for massless particles, i.e., $r_c = 3m$.

On the other hand, as L decreases, both orbits converge and coincide at the value $L = \sqrt{12}m$, for which

$$r_c = 6m. \quad (2.3.74)$$

This value is the smallest possible for stable circular orbits in the Schwarzschild metric and is known as the **ISCO radius** (Innermost Stable Circular Orbit).

It is important to note that these orbits are geodesics, and there is nothing preventing an accelerated particle from going beyond $r = 3m$ toward the event horizon and returning, as long as it does not cross the horizon. With this context, we can have a better understanding of the concepts that I will discuss in the following chapters.

2.4 Kerr solution

Now, it happens that if we make an extremely massive object with spherical symmetry rotate, it will necessarily have an axis of rotation, and thus the invariance under rotations will be inevitably lost. Roy Kerr in 1963 proposed this idea in his famous work (Kerr, 1963) was the first to write the analytical solution for Einstein's field equations in a spherically symmetric and rotating geometry. This solution, written in *Boyer-Lindquist* coordinates, takes the form

$$g_{tt} = - \left(1 - \frac{2mr}{\Sigma} \right), \quad (2.4.1)$$

$$g_{t\phi} = - \frac{2mar \sin^2 \theta}{\Sigma}, \quad (2.4.2)$$

$$g_{rr} = \frac{\Sigma}{\Delta}, \quad (2.4.3)$$

$$g_{\theta\theta} = \Sigma, \quad (2.4.4)$$

$$g_{\phi\phi} = \left(r^2 - a^2 \frac{2ma^2 r \sin^2 \theta}{\Sigma} \right) \sin^2 \theta, \quad (2.4.5)$$

where

$$\Delta \equiv r^2 - 2mr + a^2, \quad (2.4.6)$$

$$\Sigma \equiv r^2 + a^2 \cos^2 \theta \quad (2.4.7)$$

that written as a line element is given as

$$ds^2 = - \left(1 - \frac{2mr}{\Sigma} \right) dt^2 - \frac{4mar \sin^2 \theta}{\Sigma} dt d\phi + \frac{\Sigma}{\Delta} dr^2 + \Sigma d\theta^2 + \left(r^2 - a^2 \frac{2ma^2 r \sin^2 \theta}{\Sigma} \right) \sin^2 \theta d\phi^2. \quad (2.4.8)$$

Important characteristics that can be observed from this line element are that the Kerr solution is a stationary solution, it has axial symmetry (since the metric coefficients do not depend on t or ϕ , so ∂_t and ∂_ϕ are Killing vectors). Furthermore, just like the Schwarzschild solution, which is invariant under the discrete symmetries $t \rightarrow -t$ and $\phi \rightarrow -\phi$, the Kerr solution is only invariant under $(t, \phi) \rightarrow (-t, -\phi)$.

2.4.1 Properties

After a quick inspection, it can be noted that the solution depends on two parameters, m and a , where a has dimensions of length, and when $a = 0$, the Schwarzschild solution is recovered. Additionally, in the asymptotic limit (i.e., $r \gg m$), the flat Minkowski geometry is recovered with the coordinates (t, r, θ, ϕ) .

On the other hand, the isometries given by the Killing vectors

$$K = \frac{\partial}{\partial t}, \quad (2.4.9)$$

$$L = \frac{\partial}{\partial \phi}, \quad (2.4.10)$$

lead us to the fact that if we calculate the integrals of *Komar* of each of these we obtain that m defines the mass of the object and that the solution of L leads us to the definition of angular momentum as

$$J = am. \quad (2.4.11)$$

Therefore, a is defined as the rotation parameter of the metric, and its sign will determine the direction of rotation.

These two isometries (2.4.9) and (2.4.10) allow us to obtain and define two important constants of motion for the solution, which are the energy E and the angular momentum L , which can also be expressed as follows

$$p^t = -E, \quad (2.4.12)$$

$$p^\phi = L. \quad (2.4.13)$$

In terms of the four-momentum, where $p^t = \mu u^t$ is the temporal component of the four-momentum and $p^\phi = \mu u^\phi$ is the azimuthal component of the four-momentum, with μ being the rest mass of a particle for a geodesic orbit.

But in addition to these, there is a third constant of motion that allows the solution to be completely integrable.

The third constant of motion can be found using the Hamilton-Jacobi method by solving the equation ¹:

$$-\frac{\partial S}{\partial \tau} = \frac{1}{2} g^{\alpha\beta} \frac{\partial S}{\partial x^\alpha} \frac{\partial S}{\partial x^\beta} \quad (2.4.14)$$

as Carter did in (Carter, 1968) and where S is the Jacobi action, which has the form of

¹Method extracted from (Johannsen, 2013b)

$$S = \frac{1}{2}\mu^2\tau - Et + L\phi + S_r(r) + S_\theta(\theta), \quad (2.4.15)$$

where τ is the proper time. The Hamilton-Jacobi equation (2.4.14) is separable for the four coordinates, which makes geodesic motion in the Kerr metric integrable. From the separability of the equations and some algebra, it is finally obtained that the Carter constant is defined by

$$Q = C - (L - aE)^2 \quad (2.4.16)$$

or

$$Q = (p^\theta)^2 + \cos^2\theta \left[a^2(\mu^2 - E^2) + \left(\frac{L}{\sin\theta} \right)^2 \right]. \quad (2.4.17)$$

2.4.1.1 Event Horizon and Ergosphere

On the other hand, similar to the Schwarzschild metric, the Kerr metric exhibits a singularity, such that the Kretschmann scalar associated with this metric is

$$R_{\mu\nu\alpha\beta}R^{\mu\nu\alpha\beta} = \frac{48m^2(r^2 - a^2 \cos^2\theta)[\Sigma^2 - 16r^2a^2 \cos^2\theta]}{\Sigma^6}. \quad (2.4.18)$$

Here we can see that there is only one singularity when $\Sigma = 0$, which implies that $r^2 + a^2 \cos^2\theta = 0$. Therefore, the singularity occurs if

$$r = 0, \quad (2.4.19)$$

$$\cos\theta = 0. \quad (2.4.20)$$

From this, it can be deduced that the singularity present in this metric is a ring of radius a in the xy plane

$$x^2 + y^2 = a^2, \quad z = 0 \quad (2.4.21)$$

with the change of coordinates given by

$$d\tilde{t} = dt + \frac{2mr}{\Delta} dr, \quad (2.4.22)$$

$$x = r \sin \theta \cos \phi + a \sin \theta \sin \phi, \quad (2.4.23)$$

$$y = r \sin \theta \sin \phi - a \sin \theta \cos \phi, \quad (2.4.24)$$

$$z = r \cos \theta. \quad (2.4.25)$$

Just like in the Schwarzschild solution, there is also an infinite redshift surface in this Kerr solution, which can be found from the fact that on these surfaces $g_{tt} = 0$, resulting in the condition

$$r^2 - 2mr + a^2 \cos^2 \theta = 0 \quad (2.4.26)$$

from which the two surfaces appear as ²

$$r_{s\pm}(\theta) = m \pm \sqrt{m^2 - a^2 \cos^2 \theta} \quad (2.4.27)$$

with S_+ being a surface with a radius of $2m$ at the equator and a radius of $m + \sqrt{m^2 - a^2}$ at the poles when $a^2 < m^2$, and S_- being a surface contained within S_+ . Here, r_{s+} from equation (2.4.27) coincides with the Schwarzschild radius when $a = 0$, and r_{s-} corresponds to the singularity.

Now, if we perform the same analysis to find the radius of the event horizon, we need to examine where g_{rr} diverges, that is, when Δ vanishes, implying that

$$r^2 - 2mr + a^2 = 0, \quad (2.4.28)$$

so the horizon is at

$$r_{\pm} = m \pm \sqrt{m^2 - a^2}. \quad (2.4.29)$$

And they only exist if $a^2 \leq m^2$. When $a^2 > m^2$, a "naked" singularity appears in the gravitational field since there is no horizon. The hypothesis that this

²Surfaces also known as **Killing horizons**, since for all points on them it holds that $\varepsilon^\mu \varepsilon_\mu = 0$, with ε^μ being a Killing vector.

cannot exist in reality is known as the *Cosmic Censorship Conjecture* proposed by Penrose, which states that gravitational collapses have well-behaved initial conditions and therefore cannot give rise to a naked singularity.

When analyzing the behavior of the aforementioned regions, three zones are found where the Kerr solution is regular

$$I : r_+ < r < \infty, \quad (2.4.30)$$

$$II : r_- < r < r_+, \quad (2.4.31)$$

$$III : 0 < r < r_-, \quad (2.4.32)$$

where the area described between the infinite redshift surface S_+ and the event horizon r_+ is known as *Ergosphere*.

2.4.1.2 ISCO radius

Now, if we consider a photon emitted in the direction of the coordinate ϕ in the equatorial plane (i.e., $\theta = \pi/2$) of a rotating black hole. Since at the instant of emission, its momentum has no r or θ components, the condition for it to be null is

$$ds^2 = 0 = g_{tt}dt^2 + g_{t\phi}(dtd\phi + d\phi dt) + g_{\phi\phi}d\phi^2, \quad (2.4.33)$$

from which it is possible to obtain that

$$\frac{d\phi}{dt} = -\frac{g_{t\phi}}{g_{\phi\phi}} \pm \sqrt{\left(\frac{g_{t\phi}}{g_{\phi\phi}}\right)^2 - \frac{g_{tt}}{g_{\phi\phi}}}. \quad (2.4.34)$$

If evaluated at the Killing horizon (see footnote 2), this yields $g_{tt} = 0$, and the non-zero solution appears as

$$\frac{d\phi}{dt} = \frac{2a}{(2m)^2 + a^2} \quad (2.4.35)$$

and can be interpreted as the photon moving around the black hole following the same direction as its rotation. When the solution is zero, the interpretation is that the photon cannot move against the direction of the black hole's rotation, illustrating that for massive particles, they will necessarily be dragged in the

direction of the black hole's rotation within the Killing horizon. Thus, with this, we can define the angular velocity at the event horizon itself as

$$\Omega_H = \frac{d\phi}{dt} \Big|_{r_+} = \frac{a}{r_+^2 + a^2}. \quad (2.4.36)$$

On the other hand, if we consider the geodesic equation (2.2.8),

$$\frac{d^2 x^\mu}{d\tau^2} + \Gamma^\mu_{\rho\sigma} \frac{dx^\rho}{d\tau} \frac{dx^\sigma}{d\tau} = 0, \quad (2.4.37)$$

where τ is the proper time and plays the role of λ as an affine parameter.

Considering also the normalization condition of the four-velocity given by

$$g_{\mu\nu} \dot{x}^\mu \dot{x}^\nu = \delta, \quad (2.4.38)$$

where δ is a parameter that defines whether the condition is for timelike geodesics ($\delta = -1$) or null geodesics ($\delta = 0$).

Following the work done by Ryan (1995) and using the condition (2.4.38) in equation (2.4.37) for a circular orbit in the equatorial plane, where thanks to the axial and reflection symmetries $dr/d\tau = d\theta/d\tau = d^2r/d\tau^2 = 0$, the geodesic motion in the radial direction is reduced to,

$$\frac{1}{2} \partial_r g_{tt} \left(\frac{dt}{d\tau} \right)^2 + \partial_r g_{t\phi} \frac{dt}{d\tau} \frac{d\phi}{d\tau} + \frac{1}{2} \partial_r g_{\phi\phi} \left(\frac{d\phi}{d\tau} \right)^2 = 0, \quad (2.4.39)$$

where $\partial_r = \partial/\partial r$. From this equation, we can find the *Keplerian frequency* (or angular velocity in this particular case)³ in the equatorial plane as

$$\Omega_\phi = \frac{d\phi/d\tau}{dt/d\tau} = \frac{p_\phi}{p_t} = \frac{-\partial_r g_{t\phi} \pm \sqrt{(\partial_r g_{t\phi})^2 - \partial_r g_{tt} \partial_r g_{\phi\phi}}}{\partial_r g_{\phi\phi}} \quad (2.4.40)$$

$$= \frac{m}{(r^{3/2} + am^{1/2})^2} \quad (2.4.41)$$

³It is important to highlight that this coincidence between the Keplerian frequency and the angular velocity only occurs in specific circular orbits in the Kerr metric. For elliptical or other orbital configurations, the relationship between the Keplerian frequency and the angular velocity may be different.

where the sign $+$ refers to prograde orbits and $-$ to retrograde orbits, depending on the value of the spin parameter a , where (2.4.41) is the angular velocity for this particular case in geometric units.

Using this definition and the fact that we are working with circular orbits, in equation (2.4.38) we can obtain the expressions

$$\frac{E}{\mu} = \frac{-g_{tt} - g_{t\phi}\Omega_\phi}{\sqrt{-g_{tt} - 2g_{t\phi}\Omega_\phi - g_{\phi\phi}\Omega_\phi^2}}, \quad (2.4.42)$$

$$\frac{L}{\mu} = \pm \frac{g_{t\phi} + g_{\phi\phi}\Omega_\phi}{\sqrt{-g_{tt} - 2g_{t\phi}\Omega_\phi - g_{\phi\phi}\Omega_\phi^2}}, \quad (2.4.43)$$

which are the expressions for the energy per unit mass μ and the axial angular momentum per unit mass.

On the other hand, evaluating in the equatorial plane, the equation

$$p^\alpha p_\alpha = -\mu^2 \quad (2.4.44)$$

allows us to obtain the effective potential of the particles, given by

$$V_{eff}(r) = \mu^2 u^\alpha u_\alpha \quad (2.4.45)$$

$$= -\frac{1}{2}(g^{tt}E^2 - 2g^{t\phi}EL + g^{\phi\phi}L^2\mu^2) \quad (2.4.46)$$

$$= \frac{(-E^2 + \mu^2)r^3 - 2M\mu^2r^2 + ((-E^2 + \mu^2)a^2 + L^2)r - 2M(Ea - L)^2}{4Mr^2 - 2a^2r - 2r^3}, \quad (2.4.47)$$

from which we can obtain the innermost stable circular orbit, finding the minima and maxima of this potential by solving

$$V_{eff}(r) = 0, \quad (2.4.48)$$

$$\frac{dV_{eff}(r)}{dr} = 0, \quad (2.4.49)$$

and we obtain

$$r_{ISCO} = R_g(3 + Z_2 - [(3 - Z_1)(3 + Z_1 + 2Z_2)]^{1/2}), \quad (2.4.50)$$

where $Z_1 = 1 + (1 - a_*^2)^{1/3}[(1 + a_*)^{1/3} + (1 - a_*)^{1/3}]$, $Z_2 = (3a_*^2 + Z_1^2)^{1/2}$, $a_* = a/M$, and $R_g := m = GM/c^2$ are known as gravitational radii, a concept we will use later on.

2.5 Kerr-Like metric

The Kerr-like metric, described in [Johannsen \(2013b\)](#), is a spacetime constructed with the idea of being regular in the exterior domain of its horizon and having three constants of motion for its mathematical description to be fully integrable and preserving the separability of the Hamilton-Jacobi equations.

This last sentence is the starting point to construct this metric, i.e, if we see the Kerr solution in Boyer-Linquist coordinates as [\(2.4.1\)](#), we note that this solution has a three constant of motion including the Carter constant ([Carter, 1968](#)), which are found by Carter explicitly solving the Hamilton-Jacobi equations,

$$-\frac{\partial S}{\partial \tau} = \frac{1}{2} g^{\alpha\beta} \frac{\partial S}{\partial x^\alpha} \frac{\partial S}{\partial x^\beta}, \quad (2.5.1)$$

where τ is the proper time.

Therefore, the path Johannsen took to search for a more general metric that satisfied the separability of the equation [\(2.5.1\)](#) was to start with the expansion of the Kerr metric in its contravariant form, meaning that from the equation,

$$\begin{aligned} g^{\alpha\beta} \frac{\partial}{\partial x^\alpha} \frac{\partial}{\partial x^\beta} &= -\frac{1}{\Delta \Sigma} \left[(r^2 + a^2) \frac{\partial}{\partial t} + a \frac{\partial}{\partial \phi} \right]^2 \\ &+ \frac{1}{\Sigma \sin^2 \theta} \left[\frac{\partial}{\partial \phi} + a \sin^2 \theta \frac{\partial}{\partial t} \right]^2 \\ &+ \frac{\Delta}{\Sigma} \left(\frac{\partial}{\partial r} \right)^2 + \frac{1}{\Sigma} \left(\frac{\partial}{\partial \theta} \right)^2, \end{aligned} \quad (2.5.2)$$

he rewrote it as

$$\begin{aligned}
g^{\alpha\beta} \frac{\partial}{\partial x^\alpha} \frac{\partial}{\partial x^\beta} = & -\frac{1}{\Delta\tilde{\Sigma}} \left[(r^2 + a^2)A_1(r) \frac{\partial}{\partial t} + aA_2(r) \frac{\partial}{\partial \phi} \right]^2 \\
& + \frac{1}{\tilde{\Sigma} \sin^2 \theta} \left[A_3(\theta) \frac{\partial}{\partial \phi} + a \sin^2 \theta A_4(\theta) \frac{\partial}{\partial t} \right]^2 \\
& + \frac{\Delta}{\tilde{\Sigma}} A_5(r) \left(\frac{\partial}{\partial r} \right)^2 + \frac{1}{\tilde{\Sigma}} A_6(\theta) \left(\frac{\partial}{\partial \theta} \right)^2
\end{aligned} \tag{2.5.3}$$

with

$$\tilde{\Sigma} \equiv \Sigma + f(r) + g(\theta), \tag{2.5.4}$$

where the free scalar functions $f(r)$, $f(\theta)$, $A_i(r)$, $i = 1, 2, 5$, and $A_j(\theta)$, $j = 3, 4, 6$ are introduced, so that the Hamilton-Jacobi equations remain separable.

As in the case of Kerr, the Hamilton-Jacobi function can be defined as:

$$S \equiv \frac{1}{2}\mu^2\tau - Et + L_z\phi + S_r(r) + S_\theta(\theta), \tag{2.5.5}$$

where μ is the rest mass of a test particle on a geodesic orbit, L_z is the axial angular momentum and E is the energy, and

$$\frac{\partial S}{\partial x^\alpha} = p_\alpha, \tag{2.5.6}$$

$$\frac{\partial S}{\partial \tau} = \frac{1}{2}\mu^2. \tag{2.5.7}$$

Here,

$$p^\alpha \equiv \mu \frac{dx^\alpha}{d\tau} \tag{2.5.8}$$

is the particle's 4-momentum. From the function (2.5.5) and the equation (2.5.1) one can obtain the solutions for $S_r(r)$ and $S_\theta(\theta)$ which are,

$$S_r(r) = \pm \int dr \frac{1}{\Delta} \sqrt{\frac{R(r)}{A_5(r)}}, \tag{2.5.9}$$

$$S_\theta(\theta) = \pm \int d\theta \sqrt{\frac{\Theta(\theta)}{A_6(\theta)}}, \tag{2.5.10}$$

$$\tag{2.5.11}$$

where

$$R(r) = P^2 - \Delta\{\mu^2[r^2 + f(r)] + (L_z - aE)^2 + Q\}, \quad (2.5.12)$$

$$\begin{aligned} \Theta(\theta) = & Q + (L_z - aE)^2 - \mu^2[a^2 \cos^2 \theta + g(\theta)] \\ & - \frac{1}{\sin^2 \theta} [A_3(\theta)L_z - aA_4(\theta)E \sin^2 \theta]^2, \end{aligned} \quad (2.5.13)$$

$$P \equiv (r^2 + a^2)A_1(r)E - aA_2(r)L_z, \quad (2.5.14)$$

and also obtain the Carter-Like constant and the relation between the momenta p_α and the constant of motion:

$$E = -p_t, \quad (2.5.15)$$

$$L_z = p_\phi, \quad (2.5.16)$$

$$\begin{aligned} Q = & A_6(\theta)p_\theta^2 - (L_z - aE)^2 + \mu^2[a^2 \cos^2 \theta + g(\theta)] \\ & + \frac{1}{\sin^2 \theta} [A_3(\theta)L_z - aA_4(\theta)E \sin^2 \theta]^2. \end{aligned} \quad (2.5.17)$$

From this, the equations of motion for a particle with rest mass μ can finally be found, as Johannsen did in [Johannsen \(2013b\)](#).

Thus, since there are equations of motion associated with particles moving around this spacetime, it is valid to write the Kerr-Like metric which, in its covariant form in Boyer-Lindquist coordinates, is given by

$$g_{tt} = -\frac{\tilde{\Sigma}[\Delta A_3(\theta)^2 - a^2 A_2(r)^2 \sin^2(\theta)]}{[(r^2 + a^2)A_1(r)A_3(\theta) - a^2 A_2(r)A_4(\theta) \sin^2(\theta)]^2}, \quad (2.5.18)$$

$$g_{t\phi} = -\frac{a[(r^2 + a^2)A_1(r)A_2(r) - \Delta A_3(\theta)A_4(\theta)]\tilde{\Sigma} \sin^2(\theta)}{[(r^2 + a^2)A_1(r)A_3(\theta) - a^2 A_2(r)A_4(\theta) \sin^2(\theta)]^2}, \quad (2.5.19)$$

$$g_{rr} = \frac{\tilde{\Sigma}}{\Delta A_5(r)}, \quad (2.5.20)$$

$$g_{\theta\theta} = \frac{\tilde{\Sigma}}{A_6(\theta)}, \quad (2.5.21)$$

$$g_{\phi\phi} = \frac{\tilde{\Sigma} \sin^2(\theta)[(r^2 + a^2)^2 A_1(r)^2 - a^2 \Delta A_4(\theta)^2 \sin^2(\theta)]}{[(r^2 + a^2)A_1(r)A_3(\theta) - a^2 A_2(r)A_4(\theta) \sin^2(\theta)]^2}. \quad (2.5.22)$$

This metric also depends nonlinearly on six independent free deviation functions which in order to obtain an explicit form of this metric, [Johannsen](#)

(2013b), writes these functions as a power of series in M/r ,

$$A_i(r) \equiv \sum_{n=0}^{\infty} \alpha_{in} \left(\frac{M}{r} \right)^n, \quad i = 1, 2, 5, \quad (2.5.23)$$

and furthermore

$$f(r) \equiv \sum_{n=0}^{\infty} \epsilon_n \frac{M^n}{r^{n-2}}, \quad (2.5.24)$$

$$g(\theta) \equiv M^2 \sum_{k,l=0}^{\infty} \gamma_{kl} \sin^k \theta \cos^l \theta. \quad (2.5.25)$$

From the requirement that the metric be asymptotically flat, it can be obtained that $\alpha_{10} = \alpha_{20} = \alpha_{50} = 1$ and $A_3(\theta) = A_4(\theta) = A_6(\theta) = 1$. Additionally, Johannsen sets $\alpha_{11} = \alpha_{21} = \alpha_{51} = 0$, which defines the mass parameter M of the central object and the spin parameter a of this metric without the need for rescaling.

This metric can be further reduced by proposing constraints on its deviation parameters using the Parametrized post-Newtonian Framework (PPN), where the deviation parameters and function $\epsilon_2 = \alpha_{12} = g(\theta) = 0$ can be fixed. See Johannsen (2013b) for more details.

Finally, summarizing these conditions, the Kerr-Like metric can be written as follows:

$$g_{tt} = -\frac{\tilde{\Sigma}[\Delta - a^2 A_2(r)^2 \sin^2(\theta)]}{[(r^2 + a^2)A_1(r) - a^2 A_2(r) \sin^2(\theta)]^2}, \quad (2.5.26)$$

$$g_{t\phi} = -\frac{a[(r^2 + a^2)A_1(r)A_2(r) - \Delta]\tilde{\Sigma} \sin^2(\theta)}{[(r^2 + a^2)A_1(r) - a^2 A_2(r) \sin^2(\theta)]^2}, \quad (2.5.27)$$

$$g_{rr} = \frac{\tilde{\Sigma}}{\Delta A_5(r)}, \quad (2.5.28)$$

$$g_{\theta\theta} = \tilde{\Sigma}, \quad (2.5.29)$$

$$g_{\phi\phi} = \frac{\tilde{\Sigma} \sin^2(\theta) [(r^2 + a^2)^2 A_1(r)^2 - a^2 \Delta \sin^2(\theta)]}{[(r^2 + a^2)A_1(r) - a^2 A_2(r) \sin^2(\theta)]^2}, \quad (2.5.30)$$

where

$$A_1(r) = 1 + \sum_{n=3}^{\infty} \alpha_{1n} \left(\frac{M}{r} \right)^n, \quad (2.5.31)$$

$$A_2(r) = 1 + \sum_{n=2}^{\infty} \alpha_{2n} \left(\frac{M}{r} \right)^n, \quad (2.5.32)$$

$$A_5(r) = 1 + \sum_{n=2}^{\infty} \alpha_{5n} \left(\frac{M}{r} \right)^n, \quad (2.5.33)$$

$$\Delta \equiv r^2 - 2Mr + a^2, \quad (2.5.34)$$

$$\tilde{\Sigma} = r^2 + a^2 \cos^2 \theta + f(r), \quad (2.5.35)$$

$$f(r) = \sum_{n=3}^{\infty} \epsilon_n \frac{M^n}{r^{n-2}} \quad (2.5.36)$$

are the free functions of the metric. The Kerr metric is recovered when all the deviation parameters vanish, i.e., when $A_1(r) = A_2(r) = A_5(r) = 1$ and $f(r) = 0$.

This metric is asymptotically flat, is consistent with the current PPN constraints and has a correct Newtonian limit. Furthermore, an additional advantage of this metric is that, due to its free functions, it can describe black hole solutions in alternative theories of gravity that differ from the Kerr solution.

2.5.1 Properties of Kerr-Like metric

One of the key regions to analyze in this metric is its exterior domain with the intention of ruling out possible singularities or pathological regions that could be introduced by the free deviation functions (2.5.31). Thus, to discard potential violations of Lorentzian signature or the existence of closed timelike curves, we can start by analyzing the determinant of the metric, given by

$$\det(g_{\alpha\beta}) = -\frac{\tilde{\Sigma}^4 \sin^2 \theta}{A_5(r)[A_1(r)(r^2 + a^2) - a^2 A_2(r) \sin^2 \theta]^2}, \quad (2.5.37)$$

where this is not necessarily negative definite. [Johannsen \(2013b\)](#) then imposes the condition

$$A_1(r)(r^2 + a^2) - a^2 A_2(r) \sin^2 \theta \neq 0, \quad (2.5.38)$$

to ensure that the determinant is negative definite. Additionally, from the metric description in (2.5.26), we must have

$$\tilde{\Sigma} > 0, \quad (2.5.39)$$

$$A_5(r) > 0, \quad (2.5.40)$$

which must be fulfilled everywhere inside and outside the horizon.

These conditions can be written for the lowest order of the free deviation functions, which imposes constraints on the free parameters themselves. Therefore, we have that

$$\alpha_{13} \neq \frac{a^2 r (r^2 + \alpha_{22} M^2) \sin^2 \theta - r^3 (r^2 + a^2)}{M^3 (r^2 + a^2)}, \quad (2.5.41)$$

$$\alpha_{52} > -\frac{(M + \sqrt{M^2 - a^2})^2}{M^2}, \quad (2.5.42)$$

$$\epsilon_3 > -\frac{(M + \sqrt{M^2 - a^2})^3}{M^3}. \quad (2.5.43)$$

These limits were obtained by replacing r with r_+ with the intention of obtaining lower limits for the deviation parameters that are valid for all radii, $r \geq r_+$.

Furthermore, to rule out the existence of closed timelike curves, Johanssen imposes an additional requirement on the (ϕ, ϕ) component of the metric, which is

$$A_1(r)(r^2 + a^2)^2 - a^2 \Delta \sin^2 \theta > 0, \quad (2.5.44)$$

which implies, at the lowest order, that

$$\alpha_{13} > -\frac{(M + \sqrt{M^2 - a^2})^3}{M^3}. \quad (2.5.45)$$

This limit is also obtained for $r = r_+$. If we combine this expression with the condition (2.5.41), we obtain the limit

$$\alpha_{22} > -\frac{(M + \sqrt{M^2 - a^2})^2}{M^2}. \quad (2.5.46)$$

Therefore, the equations (2.5.45), (2.5.46), (2.5.42), and 2.5.43 define the lower limits for the deviation parameters up to the lowest order in the metric (2.5.26), depending on the mass and spin parameter.

Johannsen in (Johannsen, 2013b) verified numerically that the metric does not exhibit curvature singularities using these deviation parameters in the Kretschmann scalar.

2.5.1.1 Event Horizon

The event horizon in the case of the Kerr-like metric is calculated following the method in (Johannsen, 2013c). Since the event horizon is a null surface generated by null geodesics, the normal to the surface can be defined as n^μ , satisfying $n^\mu n_\mu = 0$. Taking this surface as a level surface of a scalar function $f(x^\alpha)$, we have

$$n^\mu = \nabla^\mu f = \partial^\mu f. \quad (2.5.47)$$

Thus, the event horizon is defined by the condition

$$g^{\mu\nu}(\partial_\mu f)(\partial_\nu f) = 0. \quad (2.5.48)$$

For metrics described in spherical-like, stationary, and axisymmetric coordinates, the equation becomes

$$g^{rr}(\partial_r f)^2 + 2g^{r\theta}(\partial_r f)(\partial_\theta f) + g^{\theta\theta}(\partial_\theta f)^2 = 0. \quad (2.5.49)$$

For the case of the Kerr metric, the function f is given by

$$f = r - H, \quad (2.5.50)$$

where the null surface is defined by $f = 0$, and the level surface in spherical-like coordinates is

$$g^{rr}(H) = 0, \quad (2.5.51)$$

from which

$$H = r_+ = M + \sqrt{M^2 - a^2}. \quad (2.5.52)$$

In a more general case, it is assumed that

$$f = r - H(\theta), \quad (2.5.53)$$

where the fact that $H(\theta)$ depends on θ is general enough to describe any horizon for which there exists a unique horizon radius at any angle θ .

Using this method (Johannsen, 2013b), it is determined that for the metric (2.5.26), that

$$r_+ = H(\theta), \quad (2.5.54)$$

which defines the ordinary differential equation,

$$g^{rr} + g^{\theta\theta} \left(\frac{dH}{d\theta} \right)^2 = 0, \quad (2.5.55)$$

where $g^{rr} = 1/g_{rr}$ and $g^{\theta\theta} = 1/g_{\theta\theta}$. At the poles and in the equatorial plane, the equation reduces to

$$g^{rr} = 0, \quad (2.5.56)$$

where the conditions (2.5.39) hold for any radius $r \geq r_+$. Thus, $g^{rr} = 0$ reduces to

$$\Delta = r^2 - 2Mr + a^2 = 0. \quad (2.5.57)$$

Hence, the horizon is given by

$$r_+ = M + \sqrt{M^2 - a^2}, \quad (2.5.58)$$

which coincides with the Kerr event horizon for any angle θ .

2.5.1.2 Ergosphere

On the other hand, the Killing horizon can be found by solving the equation

$$g_{t\phi}^2 - g_{tt}g_{\phi\phi} = \frac{\Delta\tilde{\Sigma}^2 \sin^2 \theta}{[(r^2 + a^2)A_1(r) - a^2A_2(r) \sin^2 \theta]^2}, \quad (2.5.59)$$

which reduces to the equation

$$\Delta = 0, \quad (2.5.60)$$

for which the solution is r_+ , so the *Killing horizon* coincides with the event horizon.

As we know, the ergosphere is the area between the Killing horizon and the event horizon. It can be determined by solving the equation

$$g_{tt} = 0, \quad (2.5.61)$$

which reduces to the equation,

$$\Delta - a^2A_2(r)^2 \sin^2 \theta = 0. \quad (2.5.62)$$

Thus, the shape of the ergosphere will depend on the spin parameter and the free function $A_2(r)$.

2.5.1.3 ISCO radius

By performing an analogous analysis to the one used in section 2.4.1.2, we can determine the values for the angular momentum per unit mass, energy per unit mass, Keplerian frequency, and the ISCO radius for the Kerr-Like metric. Therefore, from the geodesic equation, we have the condition

$$\partial_r g_{tt} \dot{t}^2 + 2\partial_r g_{t\phi} \dot{t} \dot{\phi} + \partial_r \dot{\phi}^2 = 0, \quad (2.5.63)$$

where $\partial_r := \partial/\partial r$ and the dot denotes $d/d\tau$. Here, the Keplerian frequency is

$$\Omega_\phi = \frac{-\partial_r g_{t\phi} \pm \sqrt{(\partial_r g_{t\phi})^2 - \partial_r g_{tt} \partial_r g_{\phi\phi}}}{\partial_r g_{\phi\phi}}, \quad (2.5.64)$$

where the signs + and – refer to prograde and retrograde orbits, respectively. Here, it is noticeable that the Keplerian frequency is independent of the free function $A_5(r)$ since it does not depend on g_{rr} .

In terms of the constants of motion,

$$\Omega_\phi = \frac{p_\phi}{p_t} = -\frac{g_{t\phi}E + g_{tt}L_z}{g_{\phi\phi}E + g_{t\phi}L_z}, \quad (2.5.65)$$

from which we can determine the energy and axial angular momentum as

$$\frac{E}{\mu} = -\frac{g_{tt} + g_{t\phi}\Omega_\phi}{\sqrt{-g_{tt} - 2g_{t\phi}\Omega_\phi - g_{\phi\phi}\Omega_\phi^2}}, \quad (2.5.66)$$

$$\frac{L_z}{\mu} = \pm \frac{g_{t\phi} + g_{\phi\phi}\Omega_\phi}{\sqrt{-g_{tt} - 2g_{t\phi}\Omega_\phi - g_{\phi\phi}\Omega_\phi^2}}, \quad (2.5.67)$$

where again the signs + and – refer to prograde and retrograde orbits, respectively. These expressions are also independent of the deviation function $A_5(r)$.⁴

On the other hand, the effective potential for the Kerr-Like metric can also be obtained analogously to what we obtained for the Kerr metric. From the equation

$$p^\alpha p_\alpha = -\mu^2, \quad (2.5.68)$$

where p^α is the momentum of the particles in an orbit and μ is the rest mass. Thus, the effective potential is given by the expression,

$$V_{eff}(r) = -\frac{1}{2}(g^{tt}E^2 - 2g^{t\phi}EL + g^{\phi\phi}L^2\mu^2), \quad (2.5.69)$$

⁴It should be noted that while these are independent of $A_5(r)$, this only occurs for circular orbits in the equatorial plane; for other types of orbits, they may depend on $A_5(r)$.

where circular orbits in the equatorial plane are governed by the equations,

$$V_{eff}(r) = 0, \quad (2.5.70)$$

$$\frac{dV_{eff}(r)}{dr} = 0, \quad (2.5.71)$$

and the radius of the innermost stable circular orbit (ISCO), in the particular case of the Kerr-Like metric, is found by numerically solving the differential equation

$$\frac{dE}{dr} = 0 \quad (2.5.72)$$

to find its minima and maxima. As we can see from the expression for the energy, it depends on the free functions $f(r)$, $A_1(r)$, and $A_2(r)$. For example, in the case of first-order deviations, at a given radius, the energy and axial angular momentum increase for decreasing values of the parameters ϵ_3 and α_{22} , and for increasing values of α_{13} .

2.5.2 Kerr-Schild-Like metric

In order to study the behavior of this metric in GRMHD-type simulations, it is useful for us to define it in Kerr-Schild coordinates, as we eliminate the coordinate singularity present at the horizon r_+ .

The derivation proposed by [Johannsen \(2013b\)](#) is similar to the one given for the Kerr metric ([Kerr, 1963](#); [Debney et al., 1969](#)). For null geodesics, the following parameters are introduced

$$\xi \equiv \frac{L_z}{E}, \quad (2.5.73)$$

$$\eta \equiv \frac{Q}{E^2}. \quad (2.5.74)$$

Using these parameters, in the functions (2.5.12) and (2.5.13), they can be

written as

$$\frac{R(r)}{E^2} = [(r^2 + a^2)A_1(r) - aA_2(r)\xi]^2 - \Delta[(\xi - a)^2 + \eta], \quad (2.5.75)$$

$$\frac{\Theta(\theta)}{E^2} = \eta + (\xi - a)^2 - \frac{1}{\sin^2 \theta}(\xi - a \sin^2 \theta)^2. \quad (2.5.76)$$

From the solutions for S_θ and S_r , we obtain the condition,

$$\eta + (\xi - a)^2 \geq 0, \quad (2.5.77)$$

where if and only if

$$\theta = \theta_0 = \text{const}, \quad (2.5.78)$$

$$\xi = a \sin^2 \theta, \quad (2.5.79)$$

the equality holds. Thus,

$$\eta = -a^2 \cos^4 \theta_0. \quad (2.5.80)$$

These expressions for the parameters η and ξ are identical for the case of the Kerr metric.

Then, with these expressions, Johanssen obtained the equations of motion for a photon, as follows

$$\frac{dt}{d\lambda} = l^t E = \frac{(r^2 + a^2)A_1(r)}{\Delta} \frac{(r^2 + a^2)A_1(r) - a^2 A_2(r) \sin^2 \theta}{\tilde{\Sigma}} E, \quad (2.5.81)$$

$$\frac{dr}{d\lambda} = \pm l^r E = \pm \sqrt{A_5(r)} \frac{(r^2 + a^2)A_1(r) - a^2 A_2(r) \sin^2 \theta}{\tilde{\Sigma}} E, \quad (2.5.82)$$

$$\frac{d\theta}{d\lambda} = 0, \quad (2.5.83)$$

$$\frac{d\phi}{d\lambda} = l^\phi E = \frac{aA_2(r)}{\Delta} \frac{(r^2 + a^2)A_1(r) - a^2 A_2(r) \sin^2 \theta}{\tilde{\Sigma}} E, \quad (2.5.84)$$

where λ is an affine parameter.

If we set $E = 1$, the principal null directions are given by the vectors,

$$l_\pm^\alpha = (l^t, \pm l^r, 0, l^\phi), \quad (2.5.85)$$

where using the incoming ($-l^r$) and outgoing ($+l^r$) principal null directions, we can define the Kerr-Schild coordinates for the Kerr-Like metric as

$$dt_{\text{KS}} = dt_{\text{BL}} \mp \frac{l^t}{l^r} dr_{\text{BL}}, \quad (2.5.86)$$

$$dr_{\text{KS}} = \pm \frac{1}{l^r} dr_{\text{BL}}, \quad (2.5.87)$$

$$d\theta_{\text{KS}} = d\theta_{\text{BL}}, \quad (2.5.88)$$

$$d\phi_{\text{KS}} = d\phi_{\text{BL}} \mp \frac{l^\phi}{l^r} dr_{\text{BL}}. \quad (2.5.89)$$

Setting $E = 1$, the principal null directions for this transformation are,

$$l_{\pm}^{\alpha} = (0, \pm 1, 0, 0), \quad (2.5.90)$$

However, this transformation, in practice, is quite cumbersome and may be very difficult to carry out explicitly. Therefore, Johanssen proposes an alternative transformation for the Kerr-Schild-Like coordinates, which eliminates the transformation of the radial coordinate and also replaces the factor $(r^2 + a^2)/\Delta$ in the expression of l^t with $2Mr/\Delta$, following the work by [McKinney and Gammie \(2004\)](#). As a result, the transformation (2.5.86) becomes,

$$dt_{\text{KS}} = dt_{\text{BL}} - \frac{2Mr A_1(r)}{\Delta \sqrt{A_5(r)}} dr_{\text{BL}}, \quad (2.5.91)$$

$$dr_{\text{KS}} = dr_{\text{BL}}, \quad (2.5.92)$$

$$d\theta_{\text{KS}} = d\theta_{\text{BL}}, \quad (2.5.93)$$

$$d\phi_{\text{KS}} = d\phi_{\text{BL}} - \frac{a A_2(r)}{\Delta \sqrt{A_5(r)}} dr_{\text{BL}}. \quad (2.5.94)$$

So finally, the Kerr-Like metric transformed to the Kerr-Schild coordinates

becomes

$$g_{tt} = -\frac{\tilde{\Sigma}[\Delta - a^2 A_2(r)^2 \sin^2(\theta)]}{F}, \quad (2.5.95)$$

$$g_{tr} = \frac{\tilde{\Sigma}}{\sqrt{A_5(r)}F} \{A_1(r)[2Mr + a^2 A_2(r)^2 \sin^2(\theta)] \quad (2.5.96)$$

$$- a^2 A_2(r) \sin^2(\theta)\}, \quad (2.5.97)$$

$$g_{t\phi} = -\frac{a[(r^2 + a^2)A_1(r)A_2(r) - \Delta]\tilde{\Sigma} \sin^2(\theta)}{F}, \quad (2.5.98)$$

$$g_{rr} = \frac{\tilde{\Sigma}A_1(r)}{A_5(r)F} \{A_1(r)[\Delta + 4Mr + a^2 A_2(r)^2 \sin^2(\theta)] \quad (2.5.99)$$

$$- 2a^2 A_2(r) \sin^2(\theta)\}, \quad (2.5.100)$$

$$g_{r\phi} = -\frac{a\tilde{\Sigma} \sin^2(\theta)}{\sqrt{A_5(r)}F} [(r^2 + a^2)A_1(r)^2 A_2(r) \quad (2.5.101)$$

$$+ 2MrA_1(r) - a^2 A_2(r) \sin^2(\theta)], \quad (2.5.102)$$

$$g_{\theta\theta} = \tilde{\Sigma}, \quad (2.5.103)$$

$$g_{\phi\phi} = \frac{\tilde{\Sigma} \sin^2(\theta)[(r^2 + a^2)^2 A_1(r)^2 - a^2 \Delta \sin^2(\theta)]}{F}, \quad (2.5.104)$$

where $F = [(r^2 + a^2)A_1(r) - a^2 A_2(r) \sin^2(\theta)]^2$.

This metric will be very useful for the inclusion of this metric in the GRMHD simulations and will be discussed again in the next chapter.

2.6 Accretion Disks

Accretion disks are fundamental structures formed by matter, mainly gas in a plasma state, orbiting rapidly around interstellar objects such as stars or black holes. To understand these disks, it is necessary to start with the fundamental laws of physics, such as the conservation of mass and the conservation of the stress-energy tensor

$$\nabla_\mu(\rho u^\mu) = 0, \quad (2.6.1)$$

$$\nabla_\mu T^{\mu\nu} = 0, \quad (2.6.2)$$

where ρ is the rest mass density, u^μ is the fluid's four-velocity, ∇ is the covariant derivative, and $T^{\mu\nu}$ is the stress-energy tensor that describes the properties of

the fluid. In the case of an accretion disk around a black hole, the stress-energy tensor can be written in a generic form, as follows

$$T^\mu{}_\nu = (T^\mu{}_\nu)_F + (T^\mu{}_\nu)_V + (T^\mu{}_\nu)_M + (T^\mu{}_\nu)_R. \quad (2.6.3)$$

The reason for writing the lower index is that the symmetries of the metric generate conserved currents. In the Kerr metric, for instance, the axial symmetry and the stationary nature of the metric generate conserved currents of angular momentum and energy. In general, for metrics with one coordinate x^μ suppressed, the source term on the right-hand side of the evolution equation for $T^t{}_\mu$ vanishes. These source terms do not vanish when the equation is written with both indices up.

2.6.1 The fluid

From the previous equation, it can be seen that $(T^\mu{}_\nu)_F$ is the stress-energy tensor for the *fluid*, and it is expressed as:

$$(T^\mu{}_\nu)_F = \rho H u^\mu u_\nu + \delta^\mu{}_\nu P. \quad (2.6.4)$$

Here, the density, enthalpy, and pressure of the fluid are related, along with other parameters that follow the first law of thermodynamics

$$dU = TdS - PdV \leftrightarrow d\epsilon = Hd\rho + nTdS, \quad (2.6.5)$$

where U is the internal energy of the system, T is the temperature, S is the entropy, and $\epsilon = \rho c^2 + \Pi$ is the total energy density, with Π being the internal energy density.

In some cases, the equation of state associated with these quantities is assumed to be that of an ideal gas, which is given by

$$P = \frac{R}{\mu} \rho T, \quad (2.6.6)$$

where R is the gas constant and μ is the average molecular weight.

Thus, as in other cases, we work with two temperatures in the fluid, where T_i and μ_i are the temperature and molecular weight of the ions, and T_e, μ_e are those of the electrons, respectively. So,

$$P = \frac{R}{\mu_i} \rho T_i + \frac{R}{\mu_e} \rho T_e. \quad (2.6.7)$$

Plasmas with two temperatures are important for advection-dominated flows. These types of plasmas are also significant when considering radiation, as ions are generally heated through dissipative processes in the disk, while electrons are the ones that radiate. They exchange energy with the ions through Coulomb collision interactions. The electrons in the inner parts of accretion flows are usually much cooler because the energy exchange process is highly inefficient. However, cutting-edge research in plasma physics suggests that there may be more efficient processes that could couple the ions and electrons of the fluid. Hence, it is difficult to determine precisely the amount of energy exchange experienced by the electrons.

When in equation (2.6.3), the only surviving value of the stress-energy tensor is that of the fluid (2.6.4), it is called the stress-energy tensor of a *perfect fluid*, fulfilling the Bianchi identity given by the conservation law of this tensor. From this, we can obtain the constants of motion

$$B = -Hu_t, \quad J = Hu_\phi, \quad (2.6.8)$$

where J is the angular momentum of the fluid, and B is known as the Bernoulli function, representing the total energy of the fluid. Consequently, the specific angular momentum can be obtained as

$$l = \frac{J}{B} = -\frac{u_\phi}{u_t}, \quad (2.6.9)$$

which is a constant of motion for geodesic motion in the fluid.

2.6.2 Viscosity

The second term of the stress-energy tensor refers to the part that describes the internal forces or pressures present in an accretion disk and is represented as

$$(T^\mu{}_\nu)_V = \nu_* \sigma^\mu{}_\nu, \quad (2.6.10)$$

where $\sigma^{\mu\nu}$ is the strain tensor, defined as,

$$\sigma_{\mu\nu} = \left[\frac{1}{2} (\nabla_\mu u_\nu + \nabla_\nu u_\mu) - \Theta g_{\mu\nu} \right]_\perp, \quad (2.6.11)$$

where \perp denotes the projection into the instantaneous 3-space perpendicular to u^μ .

The vorticity is also a invariant term of the viscosity part, defined by

$$\omega_{\mu\nu} = \frac{1}{2} (\nabla_\mu u_\nu - \nabla_\nu u_\mu)_\perp \quad (2.6.12)$$

and the expansion,

$$\Theta \equiv \frac{1}{3} (\nabla_\mu u^\mu) \quad (2.6.13)$$

The viscous stress tensor in the standard hydrodynamic approach is proportional to the shear tensor, given by

$$S^\mu{}_\nu = \nu_* \rho \sigma^\mu{}_\nu, \quad (2.6.14)$$

where the rate of heat generation by the viscous stress tensor in a certain volume is given by

$$Q^+ = \int S^\mu{}_\nu \sigma^\nu{}_\mu dV, \quad (2.6.15)$$

On the other hand, the rates of viscous energy and angular momentum across a surface S are given by

$$\mathcal{J}_S = \int S^\mu{}_\nu \xi^k \nu_* N_\mu dS, \quad (2.6.16)$$

$$\mathcal{B}_S = \int S^\mu{}_\nu \eta^k \nu_* N_\mu dS. \quad (2.6.17)$$

In astrophysical accretion disks, molecular viscosity cannot explain observed phenomena due to its weakness. Instead, the turbulence generated by the

magneto-rotational instability (MRI) serves as the source of stresses in the disk. Nevertheless, these stresses can be modeled as effective viscosity within standard hydrodynamics, avoiding the complexity of magnetohydrodynamics (MHD). The Shakura-Sunyaev "alpha viscosity" prescription is used to parameterize these stresses. This approximation, based on dimensional arguments, remains relevant today and can be described by the kinematic viscosity coefficient,

$$\nu_* \approx l_0 v_0, \quad (2.6.18)$$

where l_0 is the correlation length of turbulence and v_0 is the mean turbulence speed. Assuming that the velocity of turbulent elements cannot exceed the speed of sound ($v_0 < c_s$, where c_s is the speed of sound) and that the size of these turbulent elements cannot be larger than the disk thickness ($l_0 < H$), we have

$$v_0 = \alpha H c_s, \quad (2.6.19)$$

where $0 < \alpha < 1$ is a dimensionless coefficient, assumed to be constant by Shakura and Sunyaev.

In the particular case of a thin accretion disk, the viscous stress tensor has an internal torque given by

$$\tau_{r\phi} \approx \rho \nu_* r \frac{\partial \Omega}{\partial r}. \quad (2.6.20)$$

However, for this case $r(\partial \Omega / \partial r \approx -\Omega)$ and $c_s \approx (P/\rho)^{1/2} \approx \Omega H$, so the torque is $\tau_{r\phi} = -\alpha P$.

2.6.3 Electromagnetic part

The magnetic field in accretion disks can play an important role, including generating torque to extract angular momentum, transporting energy and angular momentum out of the system, contributing to accretion disk jets, and even harnessing the differential rotation of the disk to trigger instabilities

leading to significant processes such as turbulence, energy dissipation, and angular momentum transport, which are necessary for disk accretion.

In some accretion disks around black holes, an ideal MHD description can be assumed, where infinite conductivity and zero magnetic diffusivity are considered. In this case, magnetic field lines are frozen into the fluid, theoretically satisfying the homogeneous Maxwell's equation for these accretion disks

$$\nabla_{\mu}(*F^{\mu}{}_{\nu}) = 0, \quad (2.6.21)$$

where $F^{\mu}{}_{\nu}$ is the dual. If the magnetic field four-vector is defined as $b^{\mu} = u^{\nu}F^{\mu}{}_{\nu}$, then using the condition $b^{\mu}u_{\mu} = 0$, we can obtain

$$*F^{\mu}{}_{\nu} = b^{\mu}u_{\nu} - b_{\nu}u^{\mu}. \quad (2.6.22)$$

Using this equation, the homogeneous Maxwell's equation leads us to the induction equation, where its spatial and temporal parts lead us to

$$\partial_t(\sqrt{-g}B^i) = -\partial_j(\sqrt{-g}(B^i v^j - B^j v^i)), \quad (2.6.23)$$

$$\partial_i(\sqrt{-g}B^i) = 0, \quad (2.6.24)$$

where $B^i = u^t b^i - u^i b^t$, and g is the determinant of the metric.

2.6.4 The radiation

Another crucial aspect in accretion disks is radiation, as it serves as a mechanism for carrying excess energy away from the system. In the case of geometrically thin and optically thick accretion disks, radiation is often highly efficient and dissipates the locally generated thermal energy, thus maintaining the disk in a relatively "cold" state. On the other hand, for disks dominated by advection-dominated accretion flows (ADAFs), radiation is inefficient, causing such disks to remain geometrically thick and optically thin.

In the context of optically thin disks, the radiation emissivity ϵ is composed of emissivities: bremsstrahlung ϵ_{br} , synchrotron ϵ_{synch} , and their Comptonized counterparts $\epsilon_{\text{br,C}}$ and $\epsilon_{\text{synch,C}}$. In the case of the optically thick limit, the diffusion approximation is commonly used with the total optical depth $\tau =$

$\tau_{\text{abs}} + \tau_{\text{es}}$, which accounts for both absorption and electron scattering. In both cases, radiation emission is essential for the behavior and temperature of accretion disks, resulting in the total emissivity being expressed as follows

$$\epsilon = \begin{cases} \epsilon_{\text{br}} + \epsilon_{\text{synch}} + \epsilon_{\text{br,C}} + \epsilon_{\text{synch,C}} & \text{optically thin } (\tau \ll 1), \\ \frac{8\sigma T_e^4}{3H\tau} & \text{optically thick } (\tau \gg 1), \end{cases}$$

where σ is the Stefan-Boltzmann constant. For the intermediate case, solving the transfer equation directly is necessary.

2.6.5 Thin Disk model

Most of the analytical accretion disk models assume steady and axially symmetric states of the matter accreting around the black hole. In all these types of models, physical quantities depend solely on the radial spatial coordinate r and the coordinate z , which defines the height relative to the rotation axis, in the case of cylindrical coordinates. Furthermore, it is assumed that the disk's thickness is small rather than large. These thin disks then satisfy the condition $z/r \ll 1$ throughout the matter distribution.

In the case of the Kerr geometry, the equations that describe the physics of a thin disk model are as follows:

- The equation of continuity or conservation of mass in this model is

$$\dot{M} = -2\pi\Sigma\Delta^{1/2}\frac{V}{\sqrt{1-V^2}}, \quad (2.6.25)$$

where $\Delta = r^2 - 2Mr + a^2$, Σ is the surface density defined as

$$\Sigma(r) = \int_{-H(r)}^{+H(r)} \rho(r, z) dz, \quad (2.6.26)$$

here $z = \pm H(r)$ is the height limit of the disk surface. Furthermore, V is the radial velocity of the gas measured by an observer fixed at r and co-rotating with the fluid.

- The expression for the conservation of radial momentum is given by

$$\frac{V}{1-V^2} \frac{dV}{dr} = \frac{\mathcal{A}}{r} - \frac{1}{\Sigma} \frac{dP}{dr}, \quad (2.6.27)$$

where

$$\mathcal{A} = -\frac{M\tilde{\mathcal{A}}}{r^3\Delta\Omega_k^+\Omega_k^-} \frac{(\Omega - \Omega_k^+)(\Omega - \Omega_k^-)}{1 - \tilde{\Omega}^2\tilde{R}^2}, \quad (2.6.28)$$

with $\tilde{\mathcal{A}} = (r^2 + a^2)^2 - a^2\Delta \sin^2\theta$, $\Omega = u^\phi/u^t$ which defines the angular velocity with respect to the stationary observer. $\tilde{\Omega} = \Omega - \omega$ is the angular velocity with respect to the inertial observer and

$$\Omega_k^\pm = \pm \frac{M^{1/2}}{(r^{3/2} \pm aM^{1/2})}, \quad (2.6.29)$$

which are the co-rotating and counter-rotating Keplerian frequencies.

Moreover, $\tilde{R} = \tilde{\mathcal{A}}/(r^2\Delta^{1/2})$ which is the radius of gyration.

- Another conservation law of the model is the conservation of angular momentum, given by the expression

$$\frac{\dot{M}}{2\pi}(\mathcal{L} - \mathcal{L}_{in}) = \frac{\tilde{\mathcal{A}}^{1/2}\Delta^{1/2}}{r} \gamma\alpha\Pi, \quad (2.6.30)$$

where $\mathcal{L} = u_\phi$, which is the specific angular momentum, γ is the Lorentz factor, $\Pi = 2HP$ which is considered as the integrated vertical pressure, and α is the standard alpha viscosity.

- The conservation law for energy is given by the equation

$$-\frac{\alpha\Pi\tilde{\mathcal{A}}\gamma^2}{r^3} \frac{d\Omega}{dr} - \frac{32\sigma T^4}{3\kappa\Sigma} = -\frac{\dot{M}}{2\pi r\rho} \frac{1}{\Gamma_3 - 1} \left(\frac{dP}{dr} - \Gamma_1 \frac{P}{\rho} \frac{d\rho}{dr} \right), \quad (2.6.31)$$

where T is the temperature in the equatorial plane, κ is the average opacity and

$$\Gamma_1 = \beta^* + (4 - 3\beta^*)(\Gamma_3 - 1), \quad (2.6.32)$$

$$\Gamma_3 = 1 + \frac{(4 - 3\beta^*)(\gamma_g - 1)}{12(1 - \beta/\beta_m)(\gamma_g - 1) + \beta}, \quad (2.6.33)$$

where also,

$$\beta = \frac{P_{gas}}{(P_{gas} + P_{rad} + P_{mag})}, \quad (2.6.34)$$

$$\beta_m = \frac{P_{gas}}{(P_{gas} + P_{mag})}, \quad (2.6.35)$$

$$\beta^* = \beta \frac{(4 - \beta_m)}{3\beta_m}, \quad (2.6.36)$$

and γ_g is the ratio of the specific heat of the gas.

- Additionally, along with these conservation laws, we also have the expression for vertical equilibrium, given by

$$\frac{\Pi}{\Sigma H^2} = \frac{\mathcal{L}^2 - a^2(\mathcal{E}^2 - 1)}{2r^4} \quad (2.6.37)$$

with $\mathcal{E} = -u_t$ and represents the energy conserved due to time symmetry.

Shakura and Sunyaev (Shakura and Sunyaev, 1973) added a couple of extra assumptions to the model in order to reduce these differential equations to just a set of algebraic equations.

If the radial pressure and velocity gradients vanish and the rotation is Keplerian, i.e., $\Omega = \Omega_k^+$, then the radial momentum equation (2.6.27) becomes the trivial identity $0 = 0$. Furthermore, the angular momentum equation (2.6.30) only requires us to specify \mathcal{L}_{in} . Thus, if we assume that the torque vanishes at the ISCO,

$$\mathcal{L}_{in} = \mathcal{L}_k(ISCO). \quad (2.6.38)$$

In the energy conservation equation (2.6.31), it is assumed that the right-hand side is equal to zero, meaning that advective cooling disappears.

Given that the model also assumes a Keplerian-type rotation $\Omega = \Omega_k^+$ and furthermore, $\Omega = \Omega(r)$, the equation for energy (2.6.31) has, as its first term on the left-hand side, the viscous heating term which becomes a purely algebraic term due to the assumptions. Similarly, the second term becomes algebraic and represents radiative cooling.

Therefore, due to the algebraic nature of the equations (2.6.25)-(2.6.37), they

can be analytically solved for this model, for the outer, inner, and middle parts of the disk.

While this model is very useful for understanding the physics of accretion disks, the relativistic correction calculated by (Novikov and Thorne, 1973) is even more accurate and is the one we will use in this study. Thus, considering the scaling factors $m = M/M_\odot$ and $\dot{m} = \dot{M}c^2/L_{\text{edd}}$ where L_{edd} is the Eddington luminosity.

For the outer region ($P = P_{\text{gas}}, \kappa = \kappa_{ff}$ [free-free opacity]), the solution of the model's equations is:

$$\begin{aligned}
F &= [7 \times 10^{26} \text{erg cm}^{-2} \text{s}^{-1}] (m^{-1} \dot{m}) r_*^{-3} \mathcal{B}^{-1} \mathcal{C}^{-1/2} \mathcal{Q}, \\
\Sigma &= [4 \times 10^5 \text{g cm}^{-2}] (\alpha^{-4/5} m^{2/10} \dot{m}_{0*}^{7/10}) r_*^{-3/4} \mathcal{A}^{1/10} \mathcal{B}^{-4/5} \mathcal{C}^{1/2} \mathcal{D}^{-17/20} \mathcal{E}^{-1/20} \mathcal{Q}^{7/10}, \\
H &= [4 \times 10^2 \text{cm}] (\alpha^{-1/10} m^{18/20} \dot{m}^{3/20}) r_*^{9/8} \mathcal{A}^{19/20} \mathcal{B}^{-11/10} \mathcal{C}^{1/2} \mathcal{D}^{-23/40} \mathcal{E}^{-19/40} \mathcal{Q}^{11/20}, \\
\rho_0 &= [4 \times 10^2 \text{g cm}^{-3}] (\alpha^{-7/10} m^{-7/10} \dot{m}^{11/20}) r_*^{-15/8} \mathcal{A}^{-17/20} \mathcal{B}^{3/10} \mathcal{D}^{-11/40} \mathcal{E}^{17/40} \mathcal{Q}^{11/20}, \\
T &= [2 \times 10^8 \text{K}] (\alpha^{-1/5} m^{-1/5} \dot{m}^{3/10}) r_*^{-3/4} \mathcal{A}^{-1/10} \mathcal{B}^{-1/5} \mathcal{D}^{-3/20} \mathcal{E}^{1/20} \mathcal{Q}^{3/10}, \\
\beta/(1-\beta) &= [3] (\alpha^{-1/10} m^{-1/10} \dot{m}^{-7/20}) r_*^{3/8} \mathcal{A}^{-11/20} \mathcal{B}^{9/10} \mathcal{D}^{7/40} \mathcal{E}^{11/40} \mathcal{Q}^{-7/20}, \\
\tau_{ff}/\tau_{es} &= [2 \times 10^{-3}] (\dot{m}^{-1/2}) r_*^{3/4} \mathcal{A}^{-1/2} \mathcal{B}^{2/5} \mathcal{D}^{1/4} \mathcal{E}^{1/4} \mathcal{Q}^{-1/2},
\end{aligned}$$

where $r_* = rc^2/GM$.

On the other hand, for the middle region ($P = P_{\text{gas}}, \kappa = \kappa_{es}$ [electron-scattering opacity]), we have

$$\begin{aligned}
F &= [7 \times 10^{26} \text{erg cm}^{-2} \text{s}^{-1}] (m^{-1} \dot{m}) r_*^{-3} \mathcal{B}^{-1} \mathcal{C}^{-1/2} \mathcal{Q}, \\
\Sigma &= [9 \times 10^4 \text{g cm}^{-2}] (\alpha^{-4/5} m^{1/5} \dot{m}^{3/5}) r_*^{-3/5} \mathcal{B}^{-4/5} \mathcal{C}^{1/2} \mathcal{D}^{-4/5} \mathcal{Q}^{3/5}, \\
H &= [1 \times 10^3 \text{cm}] (\alpha^{-1/10} m^{9/10} \dot{m}^{1/5}) r_*^{21/20} \mathcal{A} \mathcal{B}^{-6/5} \mathcal{C}^{1/2} \mathcal{D}^{-3/5} \mathcal{E}^{-1/2} \mathcal{Q}^{1/5}, \\
\rho_0 &= [4 \times 10^1 \text{g cm}^{-3}] (\alpha^{-7/10} m^{-7/10} \dot{m}^{2/5}) r_*^{-33/20} \mathcal{A}^{-1} \mathcal{B}^{3/5} \mathcal{D}^{1/5} \mathcal{E}^{1/2} \mathcal{Q}^{2/5}, \\
T &= [7 \times 10^8 \text{K}] (\alpha^{-1/5} m^{-1/5} \dot{m}^{2/5}) r_*^{-9/10} \mathcal{B}^{-2/5} \mathcal{D}^{-1/5} \mathcal{Q}^{2/5}, \\
\beta/(1-\beta) &= [7 \times 10^{-3}] (\alpha^{-1/10} m^{-1/10} \dot{m}^{-4/5}) r_*^{21/20} \mathcal{A}^{-1} \mathcal{B}^{9/5} \mathcal{D}^{2/5} \mathcal{E}^{1/2} \mathcal{Q}^{-4/5}, \\
\tau_{ff}/\tau_{es} &= [2 \times 10^{-6}] (\dot{m}^{-1}) r_*^{3/2} \mathcal{A}^{-1} \mathcal{B}^2 \mathcal{D}^{1/2} \mathcal{E}^{1/2} \mathcal{Q}^{-1},
\end{aligned}$$

and the inner region ($P = P_{\text{gas}}, \kappa = \kappa_{\text{es}}$) are considered

$$\begin{aligned}
F &= [7 \times 10^{26} \text{erg cm}^{-2} \text{s}^{-1}] (m^{-1} \dot{m}) r_*^{-3} \mathcal{B}^{-1} \mathcal{C}^{-1/2} \mathcal{Q}, \\
\Sigma &= [5 \text{g cm}^{-2}] (\alpha^{-1} \dot{m}^{-1}) r_*^{3/2} \mathcal{A}^{-2} \mathcal{B}^3 \mathcal{C}^{1/2} \mathcal{E} \mathcal{Q}^{-1}, \\
H &= [1 \times 10^5 \text{cm}] (\dot{m}) \mathcal{A}^2 \mathcal{B}^{-3} \mathcal{C}^{1/2} \mathcal{D}^{-1} \mathcal{E}^{-1} \mathcal{Q}, \\
\rho_0 &= [2 \times 10^{-5} \text{g cm}^{-3}] (\alpha^{-1} m^{-1} \dot{m}^{-2}) r_*^{3/2} \mathcal{A}^{-4} \mathcal{B}^6 \mathcal{D} \mathcal{E}^2 \mathcal{Q}^{-2}, \\
T &= [5 \times 10^7 \text{K}] (\alpha^{-1/4} m^{-1/4}) r_*^{-3/8} \mathcal{A}^{-1/2} \mathcal{B}^{1/2} \mathcal{E}^{1/4}, \\
\beta/(1-\beta) &= [4 \times 10^{-6}] (\alpha^{-1/4} m^{-1/4} \dot{m}^{-2}) r_*^{21/8} \mathcal{A}^{-5/2} \mathcal{B}^{9/2} \mathcal{D} \mathcal{E}^{5/4} \mathcal{Q}^{-2}, \\
(\tau_{\text{ff}}/\tau_{\text{es}})^{1/2} &= [1 \times 10^{-4}] (\alpha^{-17/16} m^{-1/16} \dot{m}^{-2}) r_*^{93/32} \mathcal{A}^{-25/8} \mathcal{B}^{41/8} \mathcal{C}^{1/2} \mathcal{D}^{1/2} \mathcal{E}^{25/16} \mathcal{Q}^{-2}.
\end{aligned}$$

Here, if we consider $y = (r/M)^{1/2}$ and $a_* = a/M$, we have that

$$\begin{aligned}
\mathcal{A} &= 1 + a_*^2 y^{-4} + 2a_*^2 y^{-6}, & \mathcal{B} &= 1 + a_* y^{-3}, \\
\mathcal{C} &= 1 - 3y^{-2} + 2a_* y^{-3}, & \mathcal{D} &= 1 - 2y^{-2} + a_*^2 y^{-4}, \\
\mathcal{E} &= 1 + 4a_*^2 y^{-4} - 4a_*^2 y^{-6} + 3a_*^4 y^{-8} & \mathcal{Q}_0 &= \frac{1 + a_* y^{-3}}{y(1 - 3y^{-2} + 2a_* y^{-3})^{1/2}},
\end{aligned}$$

$$\begin{aligned}
\mathcal{Q} &= \mathcal{Q}_0 \left[y - y_0 - \frac{3}{2} a_* \ln \left(\frac{y}{y_0} \right) - \frac{3(y_1 - a_*)^2}{y_1(y_1 - y_2)(y_1 - y_3)} \ln \left(\frac{y - y_1}{y_0 - y_1} \right) \right] \\
&\quad - \mathcal{Q}_0 \left[\frac{3(y_2 - a_*)^2}{y_2(y_2 - y_1)(y_2 - y_3)} \ln \left(\frac{y - y_2}{y_0 - y_2} \right) - \frac{3(y_3 - a_*)^2}{y_3(y_3 - y_1)(y_3 - y_2)} \ln \left(\frac{y - y_3}{y_0 - y_3} \right) \right],
\end{aligned}$$

where $y_0 = (r_{\text{ms}}/M)^{1/2}$, and y_1, y_2 , and y_3 are the three roots of $y^3 - 3y + 2a_* = 0$; which is

$$\begin{aligned}
y_1 &= 2 \cos[(\cos^{-1} a_* - \pi)/3], \\
y_2 &= 2 \cos[(\cos^{-1} a_* + \pi)/3], \\
y_3 &= -2 \cos[(\cos^{-1} a_*)/3].
\end{aligned}$$

The solutions of Shakura-Sunyaev and Novikov-Thorne are limited to being local solutions. These solutions assume that the viscous torque becomes zero at the ISCO, introducing a singularity in the model at that point. For very low

accretion rates, this singularity does not affect the electromagnetic spectrum or several other crucial astrophysical predictions of the model. However, in astrophysical applications where the inner boundary condition is relevant, such as global modes of disk oscillation, the Novikov-Thorne model is inadequate. Furthermore, the numerical implementation used in this work will be described in more detail in Section (3).

2.6.6 HARM simulations

All extreme astrophysical phenomena, such as those occurring in the active nuclei of galaxies, quasars, gamma-ray bursts, and even supernova explosions, are likely driven by some rotating compact object that involves strong gravitational and magnetic fields. These kinds of objects are known as relativistic magnetorotators. While the physics governing these objects is well understood, their description involves highly nonlinear equations, which hinder their study both observationally and evolutionarily in astrophysics.

Although the difficulty of studying these objects is evident, approximations can always be made using other physical models that aim to get as close as possible to the conditions in these extreme environments. A first step in understanding these environments is to model them through non-radiative magnetohydrodynamics (MHD), so that the plasma accreting onto these objects is treated as a fluid. This reduces the degrees of freedom of the system and radiation fields can also be ignored.

The code presented below, HARM (High Accuracy Relativistic Magnetohydrodynamics) (Gammie et al., 2003), aims to be a method for numerically integrating the equations of general relativistic magnetohydrodynamic (GRMHD) fluid dynamics and primarily focuses on evolving the ideal MHD equations for a Kerr spacetime. This involves considering a gas torus in hydrostatic equilibrium that is threaded by a weak magnetic field. Here, the magnetorotational instability (Balbus and Hawley, 1990) generates turbulence in the torus, and the resulting stresses transport angular momentum outward, leading to accretion onto the central black hole.

2.6.6.1 Theoretical scheme

Theoretically, the code solves the following fundamental equations: the conservation equation for the particle number, the conservation of the energy-momentum tensor that can be expressed in terms of four equations, and the induction equation. Now, considering $c = 1$, the first equation is the conservation of the particle number,

$$(nu^\mu)_{;\mu} = 0, \quad (2.6.39)$$

where n is the particle number density, u^μ is the four-velocity, and $;$ denotes the covariant derivative of the expression (i.e., $f_{;\mu} = \nabla_\mu f$).

For numerical purposes, n can be rewritten in the coordinate basis as the "rest-mass density" $\rho = mn$, where m is the average rest mass per particle,

$$\frac{1}{\sqrt{-g}} \partial_\mu (\sqrt{-g} \rho u^\mu) = 0, \quad (2.6.40)$$

where g represents the metric determinant.

The equations representing the conservation of the energy-momentum tensor for this model are,

$$T^\mu{}_{\nu;\mu} = 0, \quad (2.6.41)$$

where written in the coordinate basis,

$$\partial_i (\sqrt{-g} T^i{}_\nu) = -\partial_i (\sqrt{-g} T^i{}_\nu) + \sqrt{-g} T^\kappa{}_\lambda \Gamma^\lambda{}_{\mu\kappa}, \quad (2.6.42)$$

where i is the spatial index and $\Gamma^\lambda{}_{\mu\kappa}$ are the Christoffel symbols.

On the other hand, if we write the explicit composition of the energy-momentum tensor for this model, it is given by the perfect fluid part,

$$(T^{\mu\nu})_F = (\rho + u + p)u^\mu u^\nu + pg^{\mu\nu}, \quad (2.6.43)$$

where u is the internal energy and p is the pressure. On the other hand, the electromagnetic part is given by

$$(T^{\mu\nu})_{EM} = F^{\mu\alpha}F^\nu{}_\alpha - \frac{1}{4}g^{\mu\nu}F_{\alpha\beta}F^{\alpha\beta}, \quad (2.6.44)$$

here $F^{\alpha\beta}$ is the electromagnetic field tensor or Faraday tensor (where also for convenience the factor $\sqrt{4\pi}$ is absorbed in the definition of $F^{\alpha\beta}$).

Furthermore, if we adopt the ideal MHD approximation, in which the electric field disappears in the fluid's rest reference frame due to the high conductivity of the plasma (i.e., $\mathbf{E} + \mathbf{v} \times \mathbf{B} = 0$). Likewise, the Lorentz force for a charged particle vanishes in the fluid's reference frame.

$$u_\mu F^{\mu\nu} = 0. \quad (2.6.45)$$

Additionally, defining the magnetic field four-vector as,

$$b^\mu = \frac{1}{2}\epsilon^{\mu\nu\kappa\lambda}u_\nu F_{\lambda\kappa}, \quad (2.6.46)$$

where $\epsilon^{\mu\nu\kappa\lambda}$ is the Levi-Civita tensor. Substituting this into the equation for the electromagnetic field's energy-momentum tensor and given the condition $b_\mu u^\mu = 0$,

$$(T^{\mu\nu})_{EM} = b^2 u^\mu u^\nu + \frac{1}{2}b^2 g^{\mu\nu} - b^\mu b^\nu. \quad (2.6.47)$$

Furthermore, if we sum $(T^{\mu\nu})_F$ and $(T^{\mu\nu})_{EM}$, we obtain the energy-momentum tensor of MHD as

$$(T^{\mu\nu})_{MHD} = (\rho + u + p + b^2)u^\mu u^\nu + \left(\frac{1}{2}b^2 + p\right)g^{\mu\nu} - b^\mu b^\nu, \quad (2.6.48)$$

which is used for describing the matter in this accretion disk model.

Additionally, the evolution of the electromagnetic field is given by the source-free part of Maxwell's equations,⁵

$$F_{\mu\nu,\lambda} + F_{\lambda\mu,\nu} + F_{\nu\lambda,\mu} = 0. \quad (2.6.49)$$

⁵The rest of the equations define the charge $J^\mu = F^\mu{}_{;\nu}$ which are not needed for the evolution of the field, as it happens in non-relativistic MHD.

Taking the dual of this equation, Maxwell's equations can be written in their conservative form as

$$F^{*\mu\nu}{}_{;\nu} = 0, \quad (2.6.50)$$

where $F^*_{\mu\nu} = \frac{1}{2}\epsilon\mu\nu\kappa F^{\kappa\lambda}$ is the dual of the electromagnetic field tensor. In ideal MHD, it can be proven that

$$F^{*\mu\nu} = b^\mu u^\nu - b^\nu u^\mu. \quad (2.6.51)$$

Considering this definition, and since the components of b^μ are not independent, given the condition $b^\mu u_\mu = 0$, the magnetic field vector $B^i = F^{*it}$ can be defined, where the spatial components and the temporal component of the tensor b^μ in terms of B^i are written as

$$b^t = B^i u^t g_{i\mu}, \quad (2.6.52)$$

$$b^i = (B^i + b^t u^i) / u^t, \quad (2.6.53)$$

leading to the spatial and temporal components of the induction equation, given by the expressions

$$\partial_t(\sqrt{-g}B^i) = -\partial_j(\sqrt{-g}(b^j u^i - b^i u^j)), \quad (2.6.54)$$

$$\frac{1}{\sqrt{-g}}\partial_i(\sqrt{-g}B^i) = 0, \quad (2.6.55)$$

respectively. This defines the condition for no monopoles. All these hyperbolic equations define a GRMHD model and are written in their conservative form, allowing their numerical resolution using well-known techniques.

2.6.6.2 Numerical scheme

Since HARM employs a complex theoretical scheme that is not analytically solvable in principle, numerical solutions are necessary to compute the desired physical quantities for the accretion disk model. Therefore, the authors decide to use a conservative scheme to define their variables. While a full understanding of the numerical scheme is not necessary for the purpose of this study, a general explanation of it and how it's implemented is provided

(for more details, refer to (Gammie et al., 2003)).

Firstly, the authors define a vector of conserved variables for each time step in the algorithm, given by

$$\mathbf{U} \equiv \sqrt{-g}(\rho u^t, T^t_t, T^t_i, B^i), \quad (2.6.56)$$

which is updated using the fluxes F . They also define a set of "primitive" variables, which are interpolated to model the flow within zones,

$$\mathbf{P} = (\rho, u, v^i, B^i), \quad (2.6.57)$$

where $v^i = u^i/u^t$ is the 3-velocity.⁶ To evaluate $\mathbf{U}(\mathbf{P})$ and $\mathbf{F}(\mathbf{P})$, one needs to find u^t and b^μ , which can be mathematically obtained from the equations of the theoretical scheme and the condition $g_{\mu\nu}u^\mu u^\nu = -1$.

Since the value that gets updated is \mathbf{U} instead of \mathbf{P} , one must solve for $\mathbf{P}(\mathbf{U})$ at each step. In HARM, this is done using the multidimensional Newton-Raphson method. Given that finding \mathbf{P} defines the core of the algorithm, this calculation is done very meticulously, minimizing numerical errors as much as possible.

To evaluate \mathbf{F} , a MUSCL-type scheme with "HLL" fluxes is used, where the fluxes are defined at the zone faces. This provides values for \mathbf{PR} and \mathbf{PL} , which are the primitive variables on the right and left sides of each zone interface. This allows the "HLL" flux \mathbf{F} to be obtained.

However, the pure "HLL" scheme doesn't preserve any numerical representation of $\nabla \cdot B = 0$. To address this, the authors use a flux-interpolated constrained transport scheme (Tóth, 2000), which can preserve the numerical representation of $\nabla \cdot B = 0$ by smoothing the fluxes with a special operator.

The approximate HLL Riemann solver doesn't require eigenvectors of the characteristic matrix, unlike Roe-type schemes. Nonetheless, it requires the maximum and minimum wave speeds (eigenvalues), which also determine the time step through the Courant conditions. In HARM, to obtain the wave speed, a wavevector $k_\mu = (-\omega, k1, 0, 0)$ is first found that satisfies the dispersion

⁶The functions $\mathbf{U}(\mathbf{P})$ and $\mathbf{F}(\mathbf{P})$ are analytic in principle, but their inverse operations are not, and the expression $\mathbf{F}(\mathbf{U})$ is not simple.

relation $D(k_\mu) = 0$ for the relevant mode. The wave speed is then obtained as ω/k_1 . The authors address this directly in HARM by finding the approximate dispersion relation and the quadrivelocity in the fluid.

2.7 Beyond Einstein Gravity

Although the theory of General Relativity has proven to be effective in describing the universe, it still has some shortcomings and is unable to solve some current physics problems, such as understanding the inflation of the universe, dark matter, dark energy, and its lack of compatibility with quantum theory. For these reasons and more, the study of modified theories of gravity is fascinating and important. In this subsection, I will present two solutions of the slowly-rotating black hole type for two actions of modified gravity that have corrections of high-curvature terms to General Relativity (Gross and Witten, 1986; Maeda et al., 2009). These types of corrections are significant as they inevitably lead to quantum gravity approaches and are a solid prediction of string theory. When considering the low-energy limit of the string theory, higher-order contractions of the Riemann tensor appear naturally. These contractions are present in the action of modified Chern-Simons gravity (Alexander and Yunes, 2009) and α' -corrected gravity (Agurto-Sepúlveda et al., 2023) presented here. We will study these two solutions, focusing on how they behave near the horizon, and compare them with the Kerr solution to measure how quantifiable their deviations are.

2.7.1 Slowly rotating Chern-Simons black hole solution

Following the work developed by (Yunes and Pretorius, 2009) in the theory of modified General Relativity known as modified Chern-Simons gravity (Alexander and Yunes, 2009), it can be observed that in this particular theory, slowly rotating black holes can be found. This implies that they possess a spin parameter, but it is conditioned by $a \ll M$. To obtain this type of solution, one typically starts from the action principle of the theory, which in this case is,

$$S = S_{EH} + S_{SC} + S_\theta + S_{mat}, \quad (2.7.1)$$

where

$$S_{EH} = \kappa \int_{\mathcal{V}} d^4x \sqrt{-g} R, \quad (2.7.2)$$

$$S_{SC} = \frac{\alpha}{4} \int_{\mathcal{V}} d^4x \sqrt{-g} \vartheta *RR, \quad (2.7.3)$$

$$S_{\vartheta} = -\frac{\beta}{2} \int_{\mathcal{V}} d^4x \sqrt{-g} [g^{ab} (\nabla_a \vartheta) (\nabla_b \vartheta) + 2V(\vartheta)], \quad (2.7.4)$$

$$S_{mat} = \int_{\mathcal{V}} d^4x \sqrt{-g} \mathcal{L}_{mat}. \quad (2.7.5)$$

The first term on the right-hand side of the equation (2.7.1) is the standard Einstein-Hilbert term, the second term is the CS correction, the third term is the action for a scalar field, and the last one describes an additional matter source with \mathcal{L}_{mat} being some Lagrangian density of matter.

In these terms, the following conventions are used: $\kappa = 1/(16\pi G)$, α and β are dimensionless coupling constants, g is the determinant of the metric, and R is the Ricci scalar. Additionally, the quantity $*RR$ describes the Pontryagin density, given by

$$*RR = *R^a{}_b{}^{cd} R^b{}_{acd}, \quad (2.7.6)$$

where

$$*R^a{}_b{}^{cd} = \frac{1}{2} \epsilon^{cdef} R^a{}_{bef}, \quad (2.7.7)$$

with ϵ^{cdef} being the Levi-Civita tensor in 4 dimensions.

The field equations of this theory are obtained by varying the action (2.7.1), so they are given by

$$R_{ab} + \frac{\alpha}{\kappa} C_{ab} = \frac{1}{2\kappa} \left(T_{ab} - \frac{1}{2} g_{ab} T \right), \quad (2.7.8)$$

$$\beta \square \vartheta = \beta \frac{dV}{d\vartheta} - \frac{\alpha}{4} *RR, \quad (2.7.9)$$

where C_{ab} is the C-tensor, given by

$$C^{ab} = \nu_c \epsilon^{cde(a} \nabla_e R_d^{b)} + \nu_{cd} *R^{d(ab)c}, \quad (2.7.10)$$

where $v_a = \nabla_a \vartheta$, $v_{ab} = \nabla_a \nabla_b \vartheta$, and R_{ab} is the Ricci tensor, and $\square = \nabla_a \nabla^a$ is the D'Alembert operator.

On the other hand, the energy-momentum tensor in the field equations is defined as follows

$$T_{ab} = T_{ab}^{mat} + T_{ab}^{\vartheta}, \quad (2.7.11)$$

where T_{ab}^{mat} is the contribution of matter to the tensor and T_{ab}^{ϑ} is the contribution of the scalar field, with its expression given by

$$T_{ab}^{\vartheta} = \beta \left[(\nabla_a \vartheta)(\nabla_b \vartheta) - \frac{1}{2}(\nabla_a \vartheta)(\nabla^a \vartheta) - g_{ab} V(\vartheta) \right]. \quad (2.7.12)$$

We note that in the modification of Chern-Simons gravity of Einstein, the strong equivalence principle is preserved (i.e. $\nabla_a T_{mat}^{ab} = 0$). This is because when one takes the divergence of the field equations, the first term on the left-hand side of the first equation vanishes due to the Bianchi identities, while the second term is given by

$$\nabla_a C^{ab} = -\frac{1}{8} v^{b*} RR, \quad (2.7.13)$$

where the equality of this contribution to the energy-momentum tensor leads to the second equation shown in (4.2.1).

There are two different formulations in the theory, the non-dynamic and dynamic formulations. The non-dynamic formulation is obtained by setting $\beta = 0$ in equations (4.2.1), so that

$$R_{ab} + \frac{\alpha}{\kappa} C_{ab} = \frac{1}{2\kappa} \left(T_{ab}^{mat} - \frac{1}{2} g_{ab} T^{mat} \right), \quad (2.7.14)$$

$$0 = {}^*RR. \quad (2.7.15)$$

On the other hand, for the dynamic scheme, β can be arbitrary.

Now, using a perturbative approach, of the form

$$g_{ab} = g_{ab}^{(0)} + \zeta g_{ab}^{(1)}(\vartheta) + \zeta^2 g_{ab}^{(2)}(\vartheta) + \mathcal{O}(\zeta^3), \quad (2.7.16)$$

where $g_{ab}^{(0)}$ is some background metric satisfying the Einstein equations, $g_{ab}^{(1)}(\vartheta)$ and $g_{ab}^{(2)}(\vartheta)$ are first and second-order perturbations of CS in the metric that depend on ϑ . Additionally, the parameter ζ serves as book-keeping to label the small coupling approximation of the theory.

Furthermore, an expansion is performed in terms of the rotation parameter of each component of the metric as follows

$$g_{ab}^{(0)} = \eta_{ab}^{(0,0)} + ah_{ab}^{(1,0)} + a^2h_{ab}^{(2,0)}, \quad (2.7.17)$$

$$\zeta g_{ab}^{(1)} = \zeta h_{ab}^{(0,1)} + \zeta ah_{ab}^{(1,1)} + \zeta a^2h_{ab}^{(2,1)}, \quad (2.7.18)$$

$$\zeta^2 g_{ab}^{(2)} = \zeta^2 h_{ab}^{(0,2)} + \zeta^2 ah_{ab}^{(1,2)} + \zeta^2 a^2h_{ab}^{(2,2)}. \quad (2.7.19)$$

From this expansion, it is possible to find a slow-rotating black hole solution, with the ansatz given by the Hartle-Thorne approximation, where the line element is parameterized by

$$ds^2 = -f[1 + h(r, \theta)]dt^2 + \frac{1}{f}[1 + m(r, \theta)]dr^2 \quad (2.7.20)$$

$$+ r^2[1 + k(r, \theta)]d\theta^2 + r^2 \sin^2 \theta [1 + p(r, \theta)][d\phi - \omega(r, \theta)dt]^2. \quad (2.7.21)$$

Here, $f = 1 - 2M/r$ is the Schwarzschild factor, and the line element is written in Boyer-Lindquist coordinates. From this and the perturbative expansion of the metric, it is possible to find the following line element

$$ds^2 = ds_K^2 + \frac{5}{4}\zeta_{CS} \frac{a}{M} \frac{M^5}{r^4} \left(1 + \frac{12M}{7r} + \frac{27M^2}{10r^2}\right) \sin^2 \theta dt d\phi, \quad (2.7.22)$$

where ds_K^2 is the slow-rotation approximation of the Kerr metric, and furthermore

$$\zeta_{CS} = \frac{\alpha^2}{\kappa\beta M^4}, \quad (2.7.23)$$

is the weak coupling parameter, limited by $\zeta_{CS} \ll 1$ to be an effective gravity theory (Alexander and Yunes, 2009). On the other hand, the scalar field ϑ is

$$\vartheta = \frac{5}{8} \frac{\alpha}{\beta} \frac{a}{Mr^2} \left(1 + \frac{2M}{r} + \frac{18M^2}{5r^2}\right) \cos \theta, \quad (2.7.24)$$

which is the solution to the field equations of the theory to order $\mathcal{O}(a\zeta)$.

Some of the properties of this solution are its separability under the Hamilton-Jacobi equations (Amarilla et al., 2010), and the positions of the event horizon and the ergosphere are the same as in the case of Kerr (see Section 2.5.1.1 and 2.5.1.2). Due to the perturbation decaying as $1/r^4$, it indicates that this solution is also asymptotically flat, and hence, the Arnowitt-Deser-Misner (ADM) formalism's mass and angular momentum remain unchanged. One way to understand this is by calculating the energy for the scalar field outside the horizon, which is given by

$$E_\vartheta = \frac{1685\pi\kappa a^2}{36864 M} \zeta_{CS}. \quad (2.7.25)$$

From this, we can observe that the term $a^2\zeta_{CS}$ goes beyond the perturbative approximation we are working with, hence the contribution of the scalar field to the total energy is zero, leading to the unchanged ADM mass and the horizon area; the same can be done for angular momentum.

On the other hand, since the scalar field ϑ for the perturbation at this order depends on the mass M and the rotation parameter a , we cannot necessarily claim that it constitutes a violation of the no-hair theorem.

An interesting case where there is a deviation in this solution is the location of the ISCO radius, which in CS gravity is given by

$$R_{ISCO} = 6M \mp \frac{4\sqrt{6}a}{3} - \frac{7a^2}{18M} \pm \frac{77\sqrt{6}a\zeta_{CS}}{5184}, \quad (2.7.26)$$

where the upper sign is for co-rotating geodesics, and the lower sign is for counter-rotating geodesics.

2.7.2 Slowly rotating α' theory black hole solution

With the intention of performing the study of Kerr deviations given by another modified gravity theory in (Metsaev and Tseytlin, 1987; Cano et al., 2018, 2020) and (Agurto-Sepúlveda et al., 2023) we studied the following principle of

action related to string theory at low energy

$$S[g_{\mu,\nu}, \phi] = \int_M d^d x \sqrt{-g} e^{-2\phi} [R + 4(\nabla\phi)^2] \quad (2.7.27)$$

$$+ \alpha (R_{\mu\nu\lambda\rho} R^{\mu\nu\lambda\rho}) - 4R_{\mu\nu} R^{\mu\nu} + R^2 - 16(\partial_\mu\phi\partial^\mu\phi)^2 + \mathcal{O}(\alpha^2)]. \quad (2.7.28)$$

Considering the case where $d = 4$ the field equations are

$$G_{\mu\nu} + 4\partial_\mu\phi\partial_\nu\phi - 2g_{\mu\nu}\partial_\rho\phi\partial^\rho\phi + 2S_{\mu\nu} - 2g_{\mu\nu}S^\rho_\rho + \alpha H_{\mu\nu} = 0, \quad (2.7.29)$$

$$R + 4\partial_\rho\phi\partial^\rho\phi + 4S^\mu_\mu + \alpha L_{GB} -$$

$$32\alpha \left(\nabla^\mu (\partial_\rho\phi\partial^\rho\phi) \partial_\mu\phi + (\partial_\rho\phi\partial^\rho\phi) S^\mu_\mu + \frac{1}{2} (\partial_\rho\phi\partial^\rho\phi)^2 \right) = 0, \quad (2.7.30)$$

where $G_{\mu\nu} = R_{\mu\nu} - \frac{1}{2}Rg_{\mu\nu}$ is the Einstein tensor, and where

$$S_{\rho\sigma} \equiv e^{2\phi}\nabla_\rho \left(e^{-2\phi}\nabla_\sigma\phi \right), \quad L_{GB} \equiv R^{\mu\nu\rho\sigma}R_{\mu\nu\rho\sigma} - 4R^{\mu\nu}R_{\mu\nu} + R^2, \quad (2.7.31)$$

and

$$H_{\mu\nu} = S_{\mu\nu}R - 4S^\sigma_{(\mu}R_{\nu)\sigma} + 2S^\sigma_\sigma R_{\mu\nu} + 2S^{\sigma\lambda}R_{\mu\sigma\lambda\nu} \quad (2.7.32)$$

$$- 8(\partial_\rho\phi\partial^\rho\phi) \partial_\mu\phi\partial_\nu\phi + g_{\mu\nu} \left(2(\partial_\rho\phi\partial^\rho\phi)^2 - S^\sigma_\sigma R + 2S^\sigma_\lambda R^\lambda_\sigma \right).$$

Lagrangian L_{GB} is the integrand of the 4-dimensional Chern-Gauss-Bonnet topological invariant which, in the absence of the dilaton and in $d = 4$, yields the Euler characteristic; this is the EGB quadratic gravity Lagrangian.

In this context it is possible to find a static and a slow rotating black hole solution, both of which can be found in (Agurto-Sepúlveda et al., 2023). Slowly rotating approximation can also be found following the similar perturbative method as before. At first order in α and including the rotation parameter in linear and quadratic terms as well as in terms of the form $a\alpha$, the solutions

reads

$$\begin{aligned}
 ds^2 = & - \left(1 - \frac{\mu}{r} + \frac{\mu a^2 \cos^2 \theta}{r^3} + \alpha f_1(r) \right) dt^2 + 2a \left(-\frac{\mu \sin^2 \theta}{r} + \alpha h_{t\varphi}(r, \theta) \right) dt d\varphi + \\
 & \left(\frac{1}{1 - \frac{\mu}{r} + \alpha g_1(r)} - \frac{((\mu - r) \cos^2 \theta + 2r) a^2}{(r - \mu)^2 r} \right) dr^2 + \\
 & (r^2 + a^2 \cos^2 \theta) d\theta^2 + \left((r^2 + a^2) \sin^2 \theta + \frac{a^2 \mu \sin^4 \theta}{r} \right) d\varphi^2,
 \end{aligned} \tag{2.7.33}$$

with

$$f_1(r) = \frac{2\mu^2}{r^4} + \frac{5\mu}{3r^3} + \frac{4}{r^2} - \frac{8}{\mu r}, \tag{2.7.34}$$

$$g_1(r) = -\frac{40}{3r^4} + \frac{\mu}{r^3} + \frac{2}{r^2}, \tag{2.7.35}$$

$$h_{t\varphi}(r) = \sin^2 \theta \left(\frac{\hat{C}}{r} + \frac{2\mu^2 + 3\mu r + 6r^2}{r^4} \right), \tag{2.7.36}$$

and with \hat{C} being a new integration constant that, at this order, comes to renormalize the angular momentum; see (2.7.40) below. The scalar configuration is

$$\phi(r) = \phi_0 - \alpha \left(\frac{2\mu}{3r^3} + \frac{1}{r^2} + \frac{2}{\mu r} \right). \tag{2.7.37}$$

One can verify that, expanding both in the Gauss-Bonnet coupling, α , and in the rotation parameter, a , all the field equations are solved at the right order; namely

$$E_{\mu\nu} = \mathcal{O}(\alpha a^2, \alpha^2). \tag{2.7.38}$$

The angular momentum can be computed by using the Wald formalism, which yields a form

$$J = - \int_{S_{\infty}^2} \mathbf{Q}[\partial_\varphi], \tag{2.7.39}$$

with $\mathbf{Q}[\partial_\varphi]$ representing the Hodge dual of the Noether pre-potential for the Killing vector ∂_φ . The angular momentum of the spacetime is given by

$$J = \frac{a\mu}{2G} \left(1 - \frac{\alpha \hat{C}}{\mu} \right). \tag{2.7.40}$$

Solution (2.7.33)-(2.7.36) gives string theory modification to Kerr geometry.

In particular, we see order $\mathcal{O}(a\alpha)$ modifications to the off-diagonal term in the Boyer-Lindquist coordinates. This will result in deviations from the GR prediction of the Lense-Thirring precession. It will also induce modifications to the spheroidal shape of the shadow of a rotating black hole.

Chapter 3

Computational methods

To better understand our work, in this chapter, we address the numerical and computational methods employed to obtain and analyze images of black holes. We begin with a brief historical overview of black hole imaging and its relationship with ray tracing in obtaining these images. We also describe the ray tracing algorithm in use and the primary code utilized for obtaining the images, offering insights into its internal structure and its application of fluid physics and radiative transfer concepts in image generation. Furthermore, we mention auxiliary methods applied in post-processing the images for analysis and interpretation.

Black holes are fascinating objects that involve extreme physics near them. Until the early 1970s, we only had some theoretical and mathematical ideas about their behavior, especially near their event horizon and beyond. Ten years after Roy Kerr's publication (Kerr, 1963) on the geometry of a rotating black hole, James Bardeen (Bardeen, 1973), based on the analytical work of Brandon Carter, studied how photons followed null geodesics around a black hole, providing an approximation to the shape of the black hole's shadow as seen from a distant observer. At the same time, Chris Cunningham, under Bardeen's supervision (Cunningham and Bardeen, 1973), studied the circular orbit in the equatorial plane of a star around an extreme Kerr black hole, taking into account the relativistic Doppler effect on the star's luminosity.

In 1978, under the guidance of his doctoral advisor Brandon Carter, Luminet studied the appearance of a luminous accretion disk around a Schwarzschild

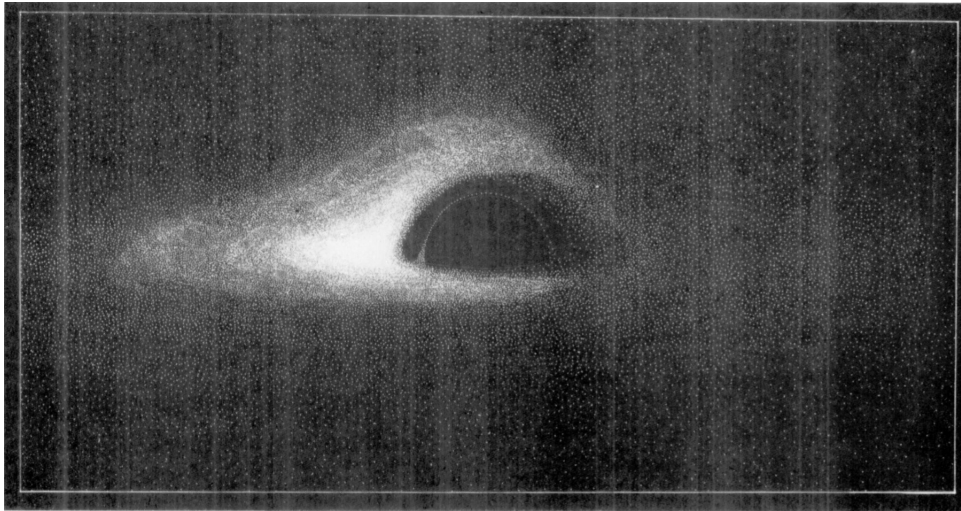


Figure 3.0.1: First simulated image of a thin accretion disk around a Schwarzschild black hole (Luminet, 1979).

black hole (Luminet, 1979). These accretion disks are present in systems with binary stars that have black holes of certain solar masses and in the centers of many galaxies that have black holes with masses ranging from a few to millions of solar masses. Luminet calculated the bolometric appearance (considering all wavelengths) of a thin accretion disk around a stationary black hole, as seen from a distant observer or a photographic plate. Initially, he conducted a geometric calculation, noting that the gravitational lensing effect gave a distinctive quality to the appearance, allowing the entire disk to be seen when observing the black hole head-on from the equatorial plane due to the strong gravity around it. He then performed a numerical calculation, taking into account the thin disk model by (Shakura and Sunyaev, 1973) its relativistic version by (Page and Thorne, 1974), obtaining a historic image of the black hole. Additionally, he observed that the frequency shift caused by Einstein's gravity and the Doppler effect were significant in the image, showing a contrast on both sides of the image depending on the direction of motion of the accreting material.

Later, other authors performed similar analyses, adding colors and obtaining similar figures. However, around 1990, experts in general relativity and computational programming such as Berkeley and Jean-Alain Marck generated the first simulated images of a Schwarzschild black hole (Marck, 1996), expanding on Luminet's work in 1979. These simulations represented a

groundbreaking computational approach to the physics of black holes, and although images were recorded, there were no published details about the algorithms used.

Regarding Ray tracing algorithms, the first work that explicitly used this method to visualize the appearance of Schwarzschild and Kerr black holes was developed by (Fanton et al., 1997). This work marked the beginning of extensive research on the appearance of black holes and accretion disks using different plasma models and improvements in algorithms and computation for Ray tracing simulations.

In our work, we used the publicly available Raptor I code to obtain images of accretion disks around Kerr black holes, considering various deviations from this geometry. We employed two accretion disk models: the numerical HARM model (Gammie et al., 2003) and the analytical Thin Disk model developed by Page and Thorne. We will describe how the Ray tracing algorithm works in general and how it is applied in the Raptor I code (Bronzwaer et al., 2018). Additionally, we will provide a detailed overview of the code's functioning, from its inputs and integration algorithms to the implementation of the disk models and emission models. Finally, we will explain how the code solves the radiative transfer equation to obtain the intensity in each pixel of the final black hole image.

3.1 Ray-Tracing

Ray tracing is an image rendering technique based on simulating the path of light rays and their intersection with objects in a three-dimensional scene to produce images as realistic as possible. The first historical record was given by (Appel, 1968), which was later improved by (Whitted, 1979) and first used in the generation of images of black holes, as mentioned previously by (Fanton et al., 1997).

The algorithm is responsible for generating these realistic images based on the path of the light rays traced back to a screen, where the image is drawn at each pixel and captured by a camera or observer. In Figure 3.1.1, the functioning of the algorithm can be seen schematically.

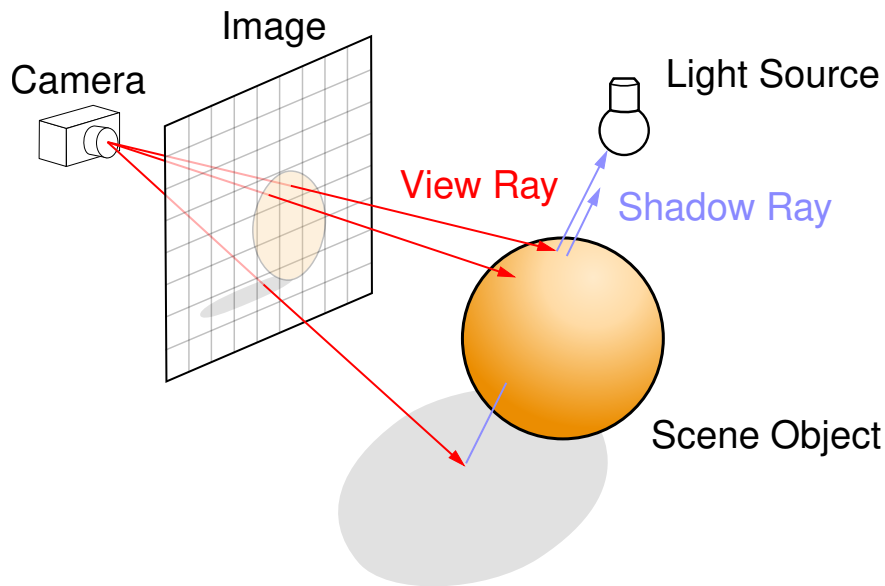


Figure 3.1.1: An esquematic diagram of the ray tracing algorithm (Henrik, 2023).

The process can be divided into several steps,

- First, primary rays are generated from the camera, passing through each pixel on the screen.
- Then, the algorithm checks if these primary rays interact with any object in the scene.
- If the ray intersects, the algorithm proceeds to calculate the position of the intersection with the object in the scene.
- After obtaining this position, the algorithm considers how light from any light source in the scene interacts with this particular point and what properties the light has at that point.
- At the same point, the algorithm verifies if there are other objects in the scene that may cause light attenuation, shadow, or other effects at this position.
- If the material of the object in the scene has been given reflective or refractive properties, these properties are also calculated at that point.
- Finally, all the properties of the light at that point are combined, and the intensity, color, and other properties of the image projected onto the

respective pixel on the screen are obtained, corresponding to the position where the light ray interacted with the object.

- Thus, by repeating this process for each pixel on the screen, the algorithm can obtain the final image viewed from the perspective of the observer or the camera.

This description of the algorithm is general, but it gives us an idea to understand the algorithm used in the Raptor I code, which is used in this study and which I will describe next.

3.2 RAPTOR I

The Raptor I code designed by (Bronzwaer et al., 2018) is an open-source code written in C programming language, was designed with two objectives: minimizing physical assumptions in arbitrary space-times and enabling time-dependent radiative transfer. It efficiently utilizes the GPU and CPU of the system. By employing a ray-tracing algorithm, the code calculates the intensity seen in each pixel of a virtual camera positioned in the observer's frame. The trajectory of photons around the black hole is determined by solving the equation of the null geodesic. Once the photon trajectory values are obtained, the radiative transfer equation is solved to determine the observer intensity and the black hole image is then obtained.

One of the main advantages of RAPTOR I is that it is possible to integrate radiative transfer problems in generic black hole spacetimes, as proposed in alternative theories of gravity, as described in sections (2.5; 2.7). Therefore, the calculation of the geodesic equations and the radiative transfer equation, which will be presented in the following sections, is made independent of the coordinate system or the geometry of the spacetime. Given this, it is important that the coordinate system used in RAPTOR be accurate near the horizon and also compatible with GRMHD simulations; thus, spherical-polar coordinates are commonly used with the radial coordinate in logarithmic scale and a denser polar coordinate mapping near the equatorial plane. These types of coordinate systems are known as modified coordinate systems, see (Gammie et al., 2003). In this work, two coordinate systems are used: the Modified Kerr-Schild (MKS) coordinate system and the Modified Boyer-Lindquist (MBL)

coordinate system, which can be found in Appendix A of (Bronzwaer et al., 2018). Additionally, a change of coordinates from the Kerr-Like metric to the Modified Kerr-Schild-Like (MKSL) coordinates was performed (A) for its use in RAPTOR I.

3.2.1 Inputs and Outputs of the code

The advantage of using RAPTOR for work lies in its great versatility when selecting code inputs. One of its main benefits is the ability to choose the spacetime in which we want to work. This is done directly in the file **parameter.h**, where it's possible to manually change the spacetime. On the other hand, if a spacetime that is not included in the code needs to be used, it can be added manually in the **metric.c** file. In this file, the metric should be added in both its covariant and contravariant forms. Additionally, the initial wave vector function should be modified as necessary for the given spacetime. The connection can be calculated or manually entered in the same file. The code takes care of the rest by itself.

Furthermore, the direct inputs of the code during execution can be modified in the **model.in** file, where they are specified. Furthermore, using the terminal

Inputs
M_{BH} [g]
$\mathcal{M}_{\text{unit}}$ [g]
Absorption [-]
Image grid (N_x, N_y)
Camera size (α, β) [R_g]
Frequency at observer [Hz]
Stepsize

Table 3.2.1: Inputs for RAPTOR code.

when executing RAPTOR, you can select the file **model.in**, the **dump** file to work with, $\mathcal{M}_{\text{unit}}$ (similarly to the **model.in** file), the inclination angle θ_0 , R_{high} , R_{low} , and the initial temporal photon wave vector value.

Moreover, the value of T_p/T_e can be chosen in the **raptor_harm_model.h** file.

Regarding the code's outputs, RAPTOR has three types of outputs. The first is a file containing the image in **.dat** or **.vtk** format, which contains the intensity

values in Jansky [Jy pixel^{-2}]. The next output is a file that contains information about the frequency at the observer and the energy spectrum. Lastly, it is possible to enable, in the `parameters.h` file, the writing of an output file that records the geodesic trajectory for each ray emitted from the camera towards the object.

3.2.2 Virtual camera

Raptor I implements ray tracing by generating a virtual camera, where the inclination of the observer is given by i , where $i = 90^\circ$ is looking at the black hole along the equatorial plane and $i = 0^\circ$, is looking at the black hole along the direction of its rotation axis, further this camera is characterized by the affine parameters α and β (celestial coordinates) defined by (Cunningham and Bardeen, 1973) in the case of Kerr geometry. Where α is the distance from the black hole rotation axis and β is the distance in the direction perpendicular to α . The initial conditions for the wave vector k^α in the Kerr geometry (BL-coordinates) is then constructed following as

$$L = -\alpha E \sqrt{1 - \cos^2 i}, \quad (3.2.1)$$

$$Q = E^2 [\beta^2 + \cos^2 i (\alpha^2 - 1)], \quad (3.2.2)$$

$$k_t = -E, \quad (3.2.3)$$

$$k_\phi = L, \quad (3.2.4)$$

$$k_\theta = \text{sign}(\beta) \sqrt{|Q - L^2 \cot^2 \theta + E^2 \cos^2 \theta|}. \quad (3.2.5)$$

Here, E is the energy of the wave vector, L is the angular momentum of the wave parallel to the black hole's rotation axis, and Q is the Carter constant (Carter, 1968) from equation (2.4.17). The radial component of the wave vector, k^r , is fixed by the condition that it is a null vector, that is, $k^\alpha k_\alpha = 0$ (k^r can be positive or negative depending on whether the light rays are outgoing or ingoing, respectively).

3.2.3 Numerical integration of the geodesic equation

In general relativity and in theories where motion is dominated by metric equations, test particles tend to move along geodesic paths. These trajectories

can be described by the geodesic equation shown in (2.2.8). Massive particles tend to move on timelike geodesics and are governed by the interval ¹

$$g_{\mu\nu} \frac{dx^\mu}{d\tau} \frac{dx^\nu}{d\tau} = -1, \quad (3.2.6)$$

where τ represents the proper time measured by an observer co-moving with the particle. In the case of photons, which are massless particles traveling at the speed of light, they follow null geodesics; hence, we have,

$$g_{\mu\nu} \frac{dx^\mu}{d\lambda} \frac{dx^\nu}{d\lambda} = 0, \quad (3.2.7)$$

where the geodesic equation is parameterized by the affine parameter λ , for which there is no proper time elapsed.

The geodesic equation can be solved analytically or numerically depending on the case. As an analytical example, we have the Schwarzschild and Kerr metrics in specific scenarios. In Raptor I, this equation is solved using numerical algorithms as it transforms into four coupled second-order differential equations

$$\frac{dx^\alpha}{d\lambda} = k^\alpha, \quad (3.2.8)$$

$$\frac{dk^\alpha}{d\lambda} = -\Gamma^\alpha_{\mu\nu} k^\mu k^\nu. \quad (3.2.9)$$

To solve these equations, we initially need appropriate initial conditions and a good numerical integrator such as Runge-Kutta or Verlet, which are algorithms used by Raptor and are described below.

3.2.3.1 Runge-Kutta

The Runge-Kutta algorithm is one of the most popular ones used in a wide variety of fields for solving ordinary differential equations. It has several versions, such as second-order, fourth-order, and even sixth-order Runge-Kutta, each with different levels of precision. The most widely used version within the community and implemented in Raptor is RK4 (fourth-order Runge-Kutta). In the case of the geodesic equation, we must consider eight dependent variables

¹The Lorentzian signature is $(-, +, +, +)$, and we use geometric units (i.e., $G = c = 1$)

defined by x^α and k^α , and we also need to evaluate 32 update coefficients for the integration. Transcribing this into equations, it appears as follows:

$$C_{1,x^\alpha} = \Delta\lambda k^\alpha, \quad (3.2.10)$$

$$C_{2,x^\alpha} = \Delta\lambda \left(k^\alpha + \frac{1}{2}C_{1,x^\alpha} \right), \quad (3.2.11)$$

$$C_{3,x^\alpha} = \Delta\lambda \left(k^\alpha + \frac{1}{2}C_{2,x^\alpha} \right), \quad (3.2.12)$$

$$C_{4,x^\alpha} = \Delta\lambda (k^\alpha + C_{3,x^\alpha}), \quad (3.2.13)$$

$$C_{1,k^\alpha} = \Delta\lambda f^\alpha(x^i, k^i), \quad (3.2.14)$$

$$C_{2,k^\alpha} = \Delta\lambda f^\alpha \left(x^i + \frac{1}{2}C_{1,x^i}, k^i + \frac{1}{2}C_{1,k^\alpha} \right), \quad (3.2.15)$$

$$C_{3,k^\alpha} = \Delta\lambda f^\alpha \left(x^i + \frac{1}{2}C_{2,x^i}, k^i + \frac{1}{2}C_{2,k^\alpha} \right), \quad (3.2.16)$$

$$C_{4,k^\alpha} = \Delta\lambda f^\alpha (x^i + C_{3,x^i}, k^i + C_{3,k^\alpha}), \quad (3.2.17)$$

$$(3.2.18)$$

where the function f^α represents the right-hand side of the geodesic equation, and the index i represents all components, mixing wave vectors with positions, that is, $f^\alpha(x^i, k^i) = f^\alpha(x^1, x^2, x^3, x^4, k^1, k^2, k^3, k^4)$.

Taking this into account, you can update the values of these components, such as,

$$x_{new}^\alpha = x^\alpha + \frac{1}{6}(C_{1,x^\alpha} + 2C_{2,x^\alpha} + 2C_{3,x^\alpha} + C_{4,x^\alpha}) + \mathcal{O}(\Delta\lambda^5), \quad (3.2.19)$$

$$k_{new}^\alpha = k^\alpha + \frac{1}{6}(C_{1,k^\alpha} + 2C_{2,k^\alpha} + 2C_{3,k^\alpha} + C_{4,k^\alpha}) + \mathcal{O}(\Delta\lambda^5). \quad (3.2.20)$$

3.2.3.2 Vervlet

While the RK4 integrator described above is one of the most accurate, there are others that can be even more precise. Calculating the connection coefficients is one of the most computationally expensive tasks. Next, I will present another integration algorithm called Verlet (Swope et al., 1982), used by Raptor I and also employed by other authors such as (Younsi et al., 2016; Dolence et al., 2009), proposing it as a faster alternative to RK4, as it evaluates the connection coefficients fewer times, the algorithm is

$$x_{n+1}^\alpha = x_n^\alpha + k_n^\alpha \Delta\lambda + \frac{1}{2} \left(\frac{dk^\alpha}{d\lambda} \right)_n (\Delta\lambda)^2, \quad (3.2.21)$$

$$k_{n+1,p}^\alpha = k_n^\alpha + \left(\frac{dk^\alpha}{d\lambda} \right)_n \Delta\lambda, \quad (3.2.22)$$

$$\left(\frac{dk^\alpha}{d\lambda} \right)_{n+1} = -\Gamma^\alpha{}_{\mu\nu}(x_{n+1}^\alpha) k_{n+1,p}^\mu k_{n+1,p'}^\nu, \quad (3.2.23)$$

$$k_{n+1}^\alpha = k_n^\alpha + \frac{1}{2} \left[\left(\frac{dk^\alpha}{d\lambda} \right)_n + \left(\frac{dk^\alpha}{d\lambda} \right)_{n+1} \right] \Delta\lambda. \quad (3.2.24)$$

This algorithm improves precision by using Eq. (3.2.24) to calculate the derivative Eq. (3.2.23) with $k^\mu n + 1, p = k^\mu n$ and reevaluating it in Eq. (3.2.24).

The complexity of studying spacetimes with geometries representing black holes is that numerical integrations become difficult near the horizon due to possible coordinate singularities. Given this, the authors (Noble et al., 2007) and (Dolence et al., 2009) introduced an adaptive step-size routine $\Delta\lambda$ to enhance the efficiency of integration algorithms in challenging regions, in this case

$$d\lambda = \frac{1}{|d\lambda_{x^1}|^{-1} + |d\lambda_{x^2}|^{-1} + |d\lambda_{x^3}|^{-1}}, \quad (3.2.25)$$

where

$$d\lambda_{x^1} := \epsilon / (|k^r| + \delta), \quad (3.2.26)$$

$$d\lambda_{x^2} := \epsilon \min(x^\theta, 1 - x^\theta) / (|k^\theta| + \delta), \quad (3.2.27)$$

$$d\lambda_{x^3} := \epsilon / (|k^\phi| + \delta). \quad (3.2.28)$$

Here, δ is a very small positive value that ensures there is no possible division by zero, and ϵ is a positive scaling parameter, which influences the scaling of all the steps.

3.2.4 Radiative transfer

With the null geodesics already calculated for the light rays traveling from the observer to interact with the black hole, it is then necessary to compute the radiative transfer equation along them. The radiative transfer equation in RAPTOR is implemented without accounting for radiation refraction effects due to plasma, which is a good approximation if the radiation frequency is

higher than the plasma frequency (i.e., $\nu_p = 8980n_e^{1/2}$ where n_e is the electron number density). Additionally, all forms of scattering and polarization can be included in simulations with ray tracing, but in this case, they are not included. RAPTOR calculates the radiative transfer equation, taking into account changes in the plasma structure during the light transport, which are usually ignored. The radiative transfer equation for the Lorentz invariant I_ν/ν^3 , where I_ν is the specific intensity of radiation at frequency ν , is thus given by (Lindquist, 1966),

$$\frac{d}{d\lambda} \left(\frac{I_\nu}{\nu^3} \right) = \frac{j_\nu}{\nu^2} - \nu\alpha_\nu \left(\frac{I_\nu}{\nu^3} \right), \quad (3.2.29)$$

where λ is the affine parameter, defined to increase as the ray travels from the plasma to the observer, ν is the frequency of the photon, j_ν is the emission coefficient of the plasma model, and α_ν is the absorption coefficient of the plasma. All these quantities are calculated in the inertial reference frame that is moving with the plasma (i.e., plasma frame). In the case of unpolarized radiation, a change of reference frame is necessary to obtain the intensity in the observer's frame. Therefore, the frequency in the fluid's reference frame is given by,

$$\nu = -k^\alpha u_\alpha, \quad (3.2.30)$$

where k^α is the contravariant wave vector and u_α is the covariant tensor for the four-velocity. Thus, the value of ν is used here to relate the absorption and emission coefficients in the fluid's reference frame to their Lorentz-invariant counterparts, eliminating the need to explicitly construct the fluid's reference frame.

The integration of equation 3.2.29 from λ_0 to λ_{obs} allows us to find the intensity observed by an observer. By relating this intensity to the intensity in the plasma's reference frame, it is possible to derive the following relationship

$$I_{\nu,obs} = \frac{I_\nu}{\nu^3} \nu_{obs}^3. \quad (3.2.31)$$

On the other hand, Equation 3.2.29 can be directly integrated. However, much more accurate results can be achieved numerically by solving the radiative

transfer equation reformulated in terms of the optical depth (see [Dexter and Agol \(2009\)](#)) τ_ν given by,

$$\tau_\nu(\lambda) = \int_{\lambda_0}^{\lambda} \nu \alpha_\nu d\lambda'. \quad (3.2.32)$$

Additionally, it can be noted that the optical depth in this case is a Lorentz invariant. Therefore, the solution to the radiative transfer equation using optical depth is given by the expression,

$$\frac{I_\nu}{\nu^3}(\tau_\nu) = \frac{I_\nu}{\nu^3}(\tau_{\nu,0}) \exp(-\tau_\nu) + \int_{\tau_{\nu,0}}^{\tau_\nu} \exp(-(\tau_\nu - \tau'_\nu)) \frac{j_\nu}{\nu^3 \alpha_\nu} d\tau'_\nu, \quad (3.2.33)$$

where $\tau_{\nu,0}$ describes the starting point of integration along the null geodesic.

It is possible to solve the above equation iteratively for each step of integration, assuming that j_ν remains constant throughout the integration. Thus, the equation becomes

$$\frac{I_\nu}{\nu^3}(\tau_\nu) = \frac{I_\nu}{\nu^3}(\tau_{\nu,0}) \exp(-\tau_\nu) + \frac{j_\nu}{\nu^3 \alpha_\nu} (1 - \exp(-\tau_\nu)). \quad (3.2.34)$$

By integrating in the opposite direction along the null geodesic compared to previous approaches, a numerically more efficient method is achieved for calculating the intensity perceived by the observer. This implies that by splitting Eq. (3.2.34) into two separate equations for intensity and optical depth, from the observer's position toward the plasma, a particularly advantageous approach to the problem is obtained. In this specific direction, it is established as a requirement that the intensity at the observer's position increases monotonically with respect to the affine parameter $\bar{\lambda}$. This parameter is the one describing the trajectory of rays in the opposite direction to λ , as defined in the previous scheme.

In addition to these improvements, this method offers three additional advantages. Firstly, it allows for the simultaneous integration of the null geodesic and specific intensity. Moreover, it enables halting the integration of the null geodesic when the optical depth between the current location and the camera exceeds a threshold value. Secondly, it eliminates the need for a data structure to store the null geodesic in memory before performing radiative

transfer calculations. This is because we simply integrate the observation alongside the geodesic itself. Thirdly, this method enables the calculation of suitable integration step sizes for both the null geodesic and radiative transfer integration, selecting the minimum value between the two. This choice prevents situations where the null geodesic integration, treated separately as if in a vacuum, rapidly advances through a plasma that is densely opaque in a significant frequency range. This can lead to inaccurate calculations and radiative transfer problems.

Then equation can be written as

$$\frac{d}{d\bar{\lambda}} \left(\frac{I_{v,obs}}{v_{obs}^3} \right) = \frac{j_v}{v^2} \exp(-\tau_{v,obs}(\bar{\lambda})), \quad (3.2.35)$$

where

$$\tau_{v,obs}(\lambda) = \int_{\lambda_{obs}}^{\lambda} \alpha_v(\lambda') v d\lambda'. \quad (3.2.36)$$

Thus, with these equations, the total invariant intensity in the observer's reference frame can be obtained, taking into account the redshift effect. In RAPTOR, to solve the differential equation (3.2.35), the corresponding emissivity coefficient is calculated, as well as the absorption-dependent optical depth for each step of the ray's path. This is numerically solved through a simple integration, summing up all the intensities that contribute to each of the pixels.

3.2.5 Emission model

3.2.5.1 Thin disk emission

Since for an analytical description of a thin accretion disk like that of Novikov-Thorne, it is necessary to know all the analytical values of the model in order to control the physical variables and ensure the accuracy of the description. We choose the radiative description of this model to be defined by thermal equilibrium blackbody emission due to its simplicity and effectiveness. Therefore, the flux is related to the disk temperature according to the standard

Stefan-Boltzmann law, as

$$F(r) = \sigma T_{eff}^4(r), \quad (3.2.37)$$

which has a local intensity given by

$$I_\nu = \frac{1}{f_{col}^4} \cdot B_\nu(\nu, T_{col}), \quad (3.2.38)$$

where

$$B_\nu(\nu, T_{col}) = \frac{2h\nu^3}{c^2} \frac{1}{\exp(h\nu/k_B T_{col}) - 1} \quad (3.2.39)$$

where $T_{col}(r) = f_{col} T_{eff}(r)$, f_{col} is the spectral hardening factor, and $B_\nu(\nu, T_{col})$ is the Planck function that describes the behavior of the blackbody spectrum.

Additionally, in this case, it serves as the emission and absorption coefficient, as it relates to them as $B_\nu = j_\nu / \alpha_\nu$.

Thus, in this case, the intensity as seen from the observer's reference frame is given by the expression,

$$I_{\nu,obs} = \frac{\nu_{obs}^3}{\nu^3} I_\nu = \frac{\nu_{obs}^3}{\nu^3} \frac{B_\nu(\nu, T_{col})}{f_{col}^4}. \quad (3.2.40)$$

In RAPTOR, this is implemented in the simplest possible manner, within the radiative transfer equation where direct calculations of these values are used and integrated for each pixel of the image. That is, in each step that follows the wave vector, this total intensity value is calculated.

3.2.5.2 Synchrotron emission

Since the dominant emission in many low-frequency models for black holes, such as the one found in Sgr A*, is synchrotron emission from a magnetized and relativistically hot plasma, it is worthwhile to consider this type of emission for more realistic descriptions of black holes and with much more complex models of accretion disks. In our case, we employ this emission type to perform image calculations using the HARM disk model with the aim of understanding how radiation transport behaves under deviations from the Kerr metric.

Therefore, in this model, we have that

$$\Theta_e = k_B \frac{T_e}{m_e c^2} \geq 1, \quad (3.2.41)$$

with k_B as the Boltzmann constant, T_e being the electron temperature, and m_e its mass, the emission and absorption coefficients of the synchrotron model depend on the electron's distribution function. Assuming that the electron follows a relativistic Maxwell-Jüttner distribution function, it is given by the expression

$$n_e^{TH}(\gamma) = \frac{n_e^{TH} \gamma \sqrt{\gamma^2 - 1} \exp(-\gamma/\Theta_e)}{\Theta_e K_2(1/\Theta_e)}, \quad (3.2.42)$$

where n_e^{TH} is the electron number density acting as a normalization constant, obtained by integrating the distribution function over all possible Lorentz factors for the electron, i.e.,

$$n_e^{TH} = \int_1^\infty n_e^{TH}(\gamma) d\gamma. \quad (3.2.43)$$

Moreover, γ is the Lorentz factor for the electron, and K_2 is the modified Bessel function of the second kind. The emission coefficient j_ν for synchrotron emission is obtained by integrating this coefficient for a single electron over all energies described by the aforementioned distribution function. Since this function involves a Bessel function, direct integration is challenging. Therefore, RAPTOR employs an approximate expression for the emission coefficient provided by (Leung et al., 2011), so that the emission coefficient is

$$j_\nu^{TH}(\nu, \theta) = \frac{\sqrt{2}\pi e^2 n_e^{TH}}{3c K_2(\Theta_e^{-1})} (X^{1/2} + 2^{11/12} X^{1/6})^2 \exp(-X^{1/3}), \quad (3.2.44)$$

where $X := \nu/\nu_s$, and ν_s defines the critical frequency for synchrotron emission, given by

$$\nu_s = \frac{2}{9} \left(\frac{eB}{2\pi m_e c} \right) \Theta_e^2 \sin \theta, \quad (3.2.45)$$

where B is the magnetic field in the inertial reference frame, θ is the angle between the photon wave vector k^μ and the magnetic field four-vector b^μ in the fluid's reference frame, and e is the elementary electric charge. Here, the emission coefficient is given in CGS units, thus having units of $[\text{ergs}^{-1}\text{Hz}^{-1}\text{cm}^{-3}]$.

For the HARM model used, where frequencies $\nu \approx 10^{11}\text{Hz}$, the emission coefficient approximation is quite reliable.

On the other hand, the absorption coefficient for the thermal electron distribution can be derived from Kirchhoff's law, where

$$\alpha_\nu^{TH} = \frac{j_\nu^{TH}}{B_\nu(\nu, T)}, \quad (3.2.46)$$

where $B_\nu(\nu, T)$ is the Planck function (3.2.39), and where the temperature is given by the term solved from equation (3.2.41), which is

$$T = \frac{m_e c^2 \Theta_e}{k_B}. \quad (3.2.47)$$

So the expression becomes,

$$B_\nu(\nu, T) = \frac{2h\nu}{c^2} \frac{1}{\exp(h\nu/(m_e c^2 \Theta_e)) - 1}. \quad (3.2.48)$$

As the GRMHD simulations in the HARM case use geometrical units, the plasma variables need to be rescaled using the scaling factors for the rest mass density, $\rho_0 = \mathcal{M}/\mathcal{L}^3$, and the scaling factor for the magnetic field $B_0 = c\sqrt{4\pi\rho_0}$. Here, $\mathcal{L} = GM/c^2$ and $\mathcal{T} = GM/c^3$ are the scaling factors for length and time, respectively. It's important to note that these are only functions of the black hole mass, where \mathcal{M} is the mass scaling factor and is a free parameter of the model.

On the other hand, the electron number density used in this model is given by the expression,

$$n_e = \rho \frac{\rho_0}{(m_e + m_p)} \text{cm}^{-3}, \quad (3.2.49)$$

where m_e and m_p are the electron and proton mass, respectively.

3.2.6 Fluid model

For the study of this thesis, two fluid models were utilized. The first one is the analytical model of a thin accretion disk studied by (Shakura and Sunyaev, 1973) and its relativistic version by (Page and Thorne, 1974). This model is implemented in RAPTOR in a semi-analytical manner, similar to (Dexter, 2016) for GRTrans, among many other authors. This model will serve us to explore the Kerr, Kerr-Like metrics, and even the metrics studied in section 2.7, given its easy implementation and the ability to control all variables within this model due to its simplicity. On the other hand, we also used a more complex numerical plasma model called HARM, developed by (Gammie et al., 2003), which is dedicated to conducting GRMHD simulations based on the Kerr metric as a background. For this reason, the study conducted on Kerr-Like metrics with this model is more focused on understanding how these types of deviations affect radiative transport in the image of the black hole. In the following two sections, I will present more details about these models and how they are implemented in RAPTOR.

3.2.6.1 Novikov-Thorne Thin disk model

RAPTOR implements the analytical thin disk model by (Shakura and Sunyaev, 1973) and (Novikov and Thorne, 1973) for the accretion disk. In this model, the accretion disk extends from the inner radius $r_{in} = r_{ISCO}$, which is analytically calculated for Kerr and Schwarzschild black holes in RAPTOR, and numerically in our case, to an outer radius $r_{out} = 1000R_g$. Consequently, the particles within the disk move in nearly circular orbits at the equator, gradually being accreted by the black hole. As explained in (2.6.5), this model assumes the absence of torque at the inner edge of the disk.

The pixel intensities in the resulting image are obtained using the radiative transfer equation (3.2.35), while the algorithm determines the plasma frequency using the equation

$$v = -k^\alpha u_\alpha, \quad (3.2.50)$$

where k^α represents the wave vectors originating from the camera, and u_α is the 4-velocity in the plasma's frame within the accretion disk.

Since the model assumes a geometrically thin and optically thick disk, it is inferred that the plasma's 4-velocity is Keplerian, as given by the expression

$$u^\alpha = \{u^t, u^r, u^\theta, u^\phi\} = \{\mathcal{A}, 0, 0, \mathcal{A}\Omega\}, \quad (3.2.51)$$

where

$$\mathcal{A} = \sqrt{\frac{-1}{g_{tt} + 2\Omega g_{t\phi} + \Omega^2 g_{\phi\phi}}}. \quad (3.2.52)$$

Here the components of the metric $g_{\mu\nu}$ are calculated for the corresponding spacetime in Boyer-Lindquist coordinates.

Additionally, if necessary, RAPTOR numerically transforms the 4-velocity to Kerr-Schild coordinates.

With these values already defined, the code calculates the energy flux from the equation

$$F(r) = \frac{\dot{M}}{4\pi M^2} f_{disk}(r), \quad (3.2.53)$$

where \dot{M} is the mass accretion rate and

$$f_{disk}(r) = -\frac{d\Omega}{dr} \frac{M^2}{\sqrt{-g}(E - \Omega L_z)^2} \int_{r_{in}}^r (E - \Omega L_z) \frac{L_z}{d\bar{r}} d\bar{r}, \quad (3.2.54)$$

where g is the determinant of the metric.

This equation, when implemented in RAPTOR, is solved through two distinct approaches: the first one analytically for the Kerr case (Page and Thorne, 1974), and the second one numerically, implemented by us using trapezoidal integration for the Kerr-Like spacetime.

With the energy flux calculation already performed, utilizing the emission model provided by (3.2.5.1) and the radiative transfer equation, it becomes possible to obtain the intensity measured in each pixel of the observer's camera.

Therefore, when the algorithm is applied correctly, it becomes feasible to generate images as shown in Fig. (3.2.1).

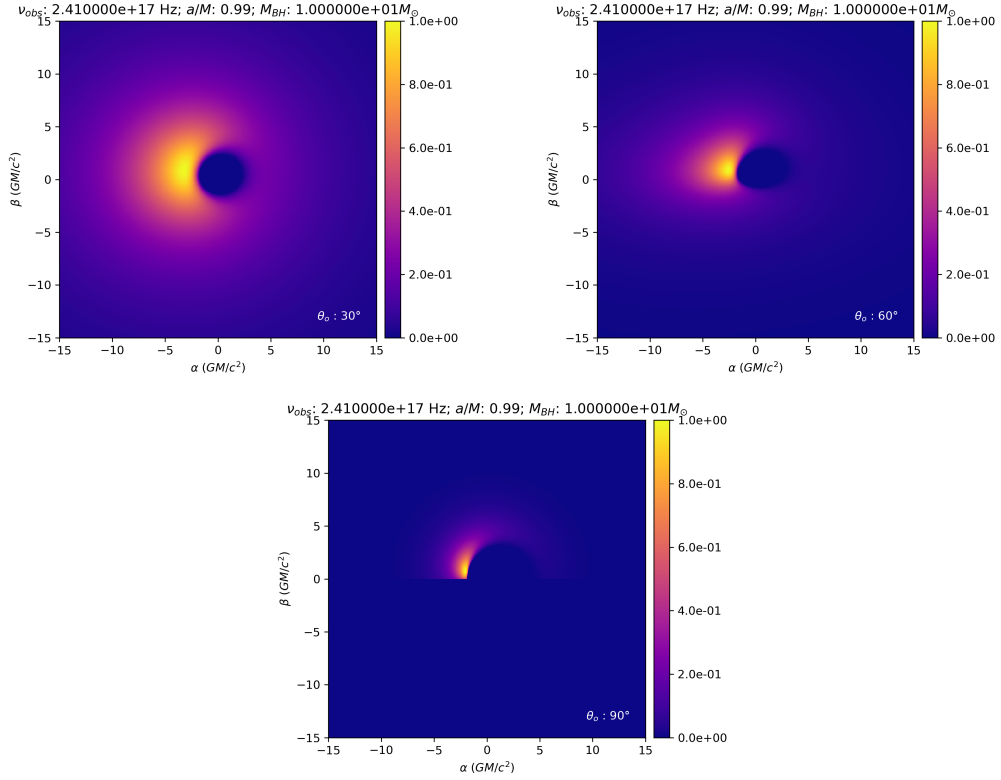


Figure 3.2.1: Thin-disk simulation for BH with a mass $10M_{\odot}$ and spin $a = 0.99 M$. With angle of view $i = 30^{\circ}$, $i = 60^{\circ}$ and $i = 90^{\circ}$.

The input values for test purposes were for the Kerr case:

Parameter	Thin-disk test value
a	$0.99M$
M_{BH}	$10M_{\odot}$
d_{source}	0.05pc
ν_{cam}	$2.41 \times 10^{17}\text{Hz}$
r_{cam}	$10^4 R_g$
Resolution for $[x, y]$	$[300, 300]\text{px}$
Range for $[\alpha, \beta]$	$[-15, 15] R_g$
\dot{M}	$1.399 \times 10^{19}\text{g/s}$
r_{ISCO}	$1.24R_g$
r_{out}	$1000R_g$
stepsize	0.001

Table 3.2.2: Settings extracted from the test using in [Bronzwaer et al. \(2020\)](#).

3.2.6.2 HARM model

RAPTOR includes the possibility to read data from HARM simulations, which contains all the information about the disk model. In this case, as described in Section (2.6.6), the simulation for this type of study was carried out using a hydrostatic equilibrium gas torus crossed by a weak magnetic field. HARM evolves the ideal MHD equations in the Kerr spacetime, where magnetorotational instabilities generate turbulence in the torus, and the resulting stresses transport angular momentum outward, leading to the accretion of plasma around the central black hole.

RAPTOR has the capability to read these GRMHD snapshots formulated by HARM. It is also capable of using a single snapshot, where the temporal coordinate of the geodesic can be ignored (slow-light approximation), or alternatively using a series of snapshots where the temporal geodesic is relevant (fast-light approximation).

In this study, in order to solely analyze how deviations affect the transport of radiation in black hole images for GRMHD simulation cases, we only explore the first option.

The fluid variables in these simulations are saved in modified Kerr-Schild coordinates and geometric units, where $G = c = M = 1$.

In RAPTOR, the implementation of the dump files is done by generating rays from the camera, initially using Boyer-Lindquist coordinates to generate wave vectors, which are later transformed to modified Kerr-Schild coordinates to work correctly with the snapshots extracted from HARM. The fluid data is stored by RAPTOR in dynamic arrays and interpolated for each value of the wave vectors. Then, this data is used for calculating the frequency in the plasma frame $\nu = -k^\alpha u_\alpha$, where u_α is directly extracted from the dump file and interpolated for the proper calculation of ν . The emission and absorption coefficient values are also calculated for a synchrotron emission model, in order to proceed with the calculation of the intensity measured in each pixel by the observer using the radiative transfer equation implemented in RAPTOR.

On the other hand, for GRMHD models, heavy ions are usually simulated. However, these ions are not sources of emission in radiative processes.

Therefore, there is a need to couple the ions to the plasma electrons. RAPTOR implements a single fluid approach, where ions and electrons are related through the expression

$$\frac{T_p}{T_e} = R_{low} \frac{1}{1 + \beta_p^2} + R_{high} \frac{\beta_p^2}{1 + \beta_p^2}, \quad (3.2.55)$$

where $\beta_p = P_{gas}/P_{mag}$, defining the ratio of gas pressure to magnetic field pressure $P_{mag} = B^2/2$, where additionally R_{low} and R_{high} are free parameters.

In magnetically strong plasmas, $\beta_p \ll 1$, thus $T_p/T_e \rightarrow R_{low}$, whereas conversely, in magnetically weak plasmas, $\beta_p \gg 1$, and $T_p/T_e \rightarrow R_{high}$.

For the cases we studied, we decided to set $R_{low} = R_{high} = 1$, as well as keeping T_p/T_e fixed. In Fig. (3.2.2), we can observe a simulation for the Kerr metric, with the sole intention of studying the effect of radiative transport.

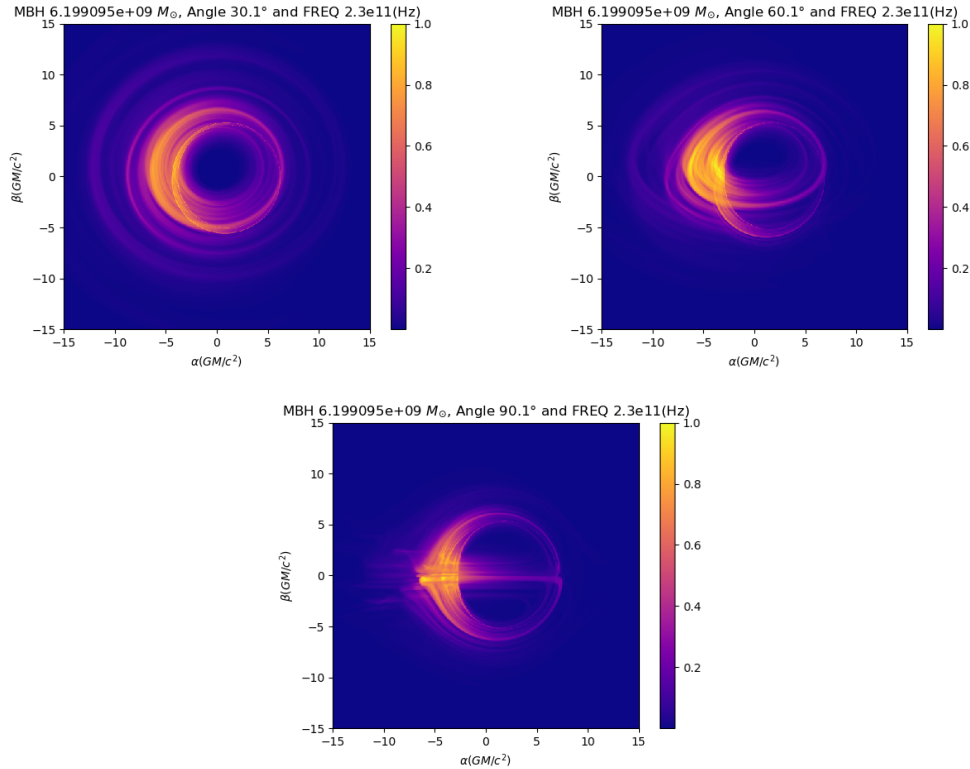


Figure 3.2.2: GRMHD simulation for SMBH with a mass $6.2 \times 10^9 M_\odot$ and spin $a = 0.9375 M$. With angle of view $i = 30^\circ$, $i = 60^\circ$ and $i = 90^\circ$.

The parameters used for this simulation are given in Tab. 3.2.3.

Table 3.2.3: Setup for the simulation of the SMBH with the distance and mass of M87*.

Parameter	Value
M_{BH}	$6.2 \times 10^9 M_{\odot}$
Distance	16.9 Mpc
a	$0.9375 M$
r_{cam}	$10^4 R_g$
Range for $[\alpha, \beta]$	$[-15, 15] R_g$
Resolution $[x, y]$	500 px
Frequency	230 GHz
Inclination ($^{\circ}$)	30, 60, 90
T_p/T_e	1.0

3.3 Kerr-Like metric implementation

Since RAPTOR is capable of utilizing different geometries through the free implementation of various metrics for use in the calculation of the geodesic equations and ultimately obtaining the black hole image through ray tracing, the implementation of the Kerr-Like metric was carried out in a straightforward and efficient manner. However, this was not done without first analytically and numerically verifying its correctness. In this section, I present the steps that were followed for its implementation and the verification of its accuracy.

Firstly, due to the use of plasma models that were numerically calculated (e.g., HARM) as one of the background fluid models, it was necessary to implement this metric in Kerr-Schild-like coordinates (2.5.2). Additionally, the coordinates needed further modification due to the nature of HARM calculations near the event horizon. Therefore, a small transformation of these coordinates to modified Kerr-Schild-like coordinates was required, where the radial coordinate r is of exponential type and the azimuthal coordinate θ is slightly modified by a parameter h . When $h = 1$, the original coordinate is recovered, and as $h \rightarrow 0$, the zones concentrate in the region near the midplane. This type of transformation can be found in Appendix A1.

RAPTOR implements metrics using functions that store values in two-index arrays, introducing the covariant and contravariant metric analytically to accelerate internal code processes. Therefore, one of the initial steps, in addition to the change of coordinates for the Kerr-Like metric, was to calculate

its contravariant form. From Eq. (2.5.95), one obtains

$$g^{tt} = \frac{\left[(-2Mr - a^2 - r^2) A_1(r)^2 - a^2 (\cos^2(\theta)) + a^2\right] F}{\left[(a^2 + r^2) A_1(r) + A_2(r) a^2 (\cos(\theta) - 1) (\cos(\theta) + 1)\right]^2 \tilde{\Sigma}'}, \quad (3.3.1)$$

$$g^{tr} = \frac{2rMA_1(r) F \sqrt{A_5(r)}}{\left[(\cos^2(\theta)) A_2(r) a^2 + (a^2 + r^2) A_1(r) - A_2(r) a^2\right]^2 \tilde{\Sigma}'}, \quad (3.3.2)$$

$$g^{t\phi} = -\frac{a (A_1(r) A_2(r) - 1) F}{\left[(\cos^2(\theta)) A_2(r) a^2 + (a^2 + r^2) A_1(r) - A_2(r) a^2\right]^2 \tilde{\Sigma}'}, \quad (3.3.3)$$

$$g^{rr} = \frac{\Delta A_5(r) F}{\left[(\cos^2(\theta)) A_2(r) a^2 + (a^2 + r^2) A_1(r) - A_2(r) a^2\right]^2 \tilde{\Sigma}'}, \quad (3.3.4)$$

$$g^{r\phi} = \frac{\sqrt{A_5(r)} F A_2(r) a}{\left[(\cos^2(\theta)) A_2(r) a^2 + (a^2 + r^2) A_1(r) - A_2(r) a^2\right]^2 \tilde{\Sigma}'}, \quad (3.3.5)$$

$$g^{\theta\theta} = \frac{1}{\tilde{\Sigma}'}, \quad (3.3.6)$$

$$g^{\phi\phi} = \frac{F}{\left[\cos^2(\theta) A_2(r) a^2 + (a^2 + r^2) A_1(r) - A_2(r) a^2\right]^2 \tilde{\Sigma}' \sin^2(\theta)^2}, \quad (3.3.7)$$

where $F = [(r^2 + a^2)A_1(r) - a^2A_2(r)\sin^2(\theta)]^2$.

This was calculated analytically using the symbolic computation software MAPLE and the GRTENSOR III package. Verification of the correct implementation of this metric was done using a Python script in which the covariant and contravariant expressions of the metric were compared with the expressions for the Kerr metric. To perform this comparison, we took the Kerr-Like metric to the limit where it reduces to the usual Kerr metric, so that $A_1(r) = A_2(r) = A_5(r) = 1$ and $f(r) = 0$.

In Fig. (3.3.1), comparisons of the components can be seen. First, a comparison was made with Kerr when the Kerr-Like metric reduces to it, and then tests were conducted by activating the free deviation functions.

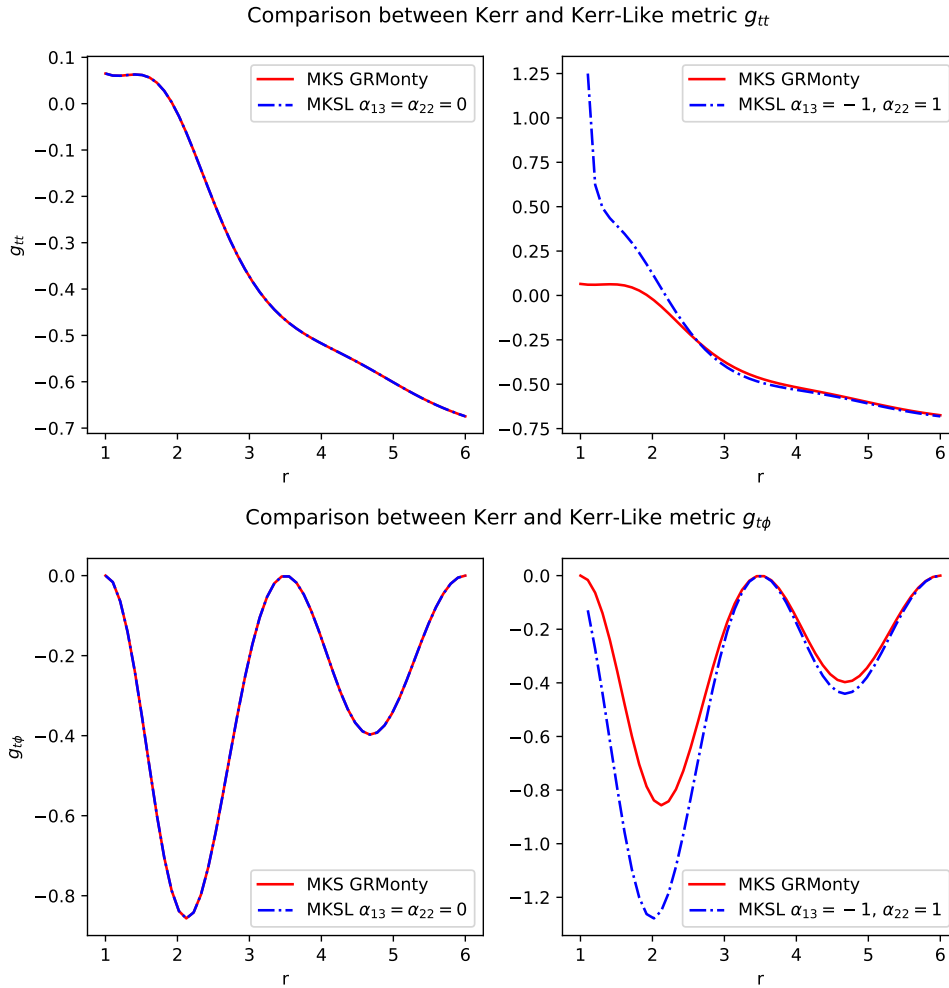


Figure 3.3.1: Comparison between the covariant components g_{tt} and $g_{t\phi}$ of the Kerr and Kerr-Like metrics. In the left panel of the figures, the comparison can be observed when the Kerr-Like metric has its free deviations set to zero (i.e., $\alpha_{13} = \alpha_{22} = 0$), thus reducing it to the Kerr metric. In the right panel of the figure, the difference can be seen when turning on the free deviations to first order in both functions $A_1(r)$ and $A_2(r)$, such that they have their maximum deviation values (i.e., $\alpha_{13} = -1$ and $\alpha_{22} = 1$).

In this figure, we can also observe that the labels of the lines indicate the name "MKS," where I am referring to the coordinates used for the comparison, which were the modified Kerr-Schild coordinates. The expression of the Kerr metric in these coordinates was also extracted from the GRMonty code (Dolence et al., 2009), which is also used in RAPTOR for describing the Kerr metric. Furthermore, it was decided to display the comparison of these metric components since deviations in these components result in a noticeable change in the figures. The same analysis was performed for the rest of the components

to ensure a proper metric implementation.

Similarly, the comparison of the contravariant metric components is performed in Fig. (3.3.2), where a similar analysis to the previous one is carried out.

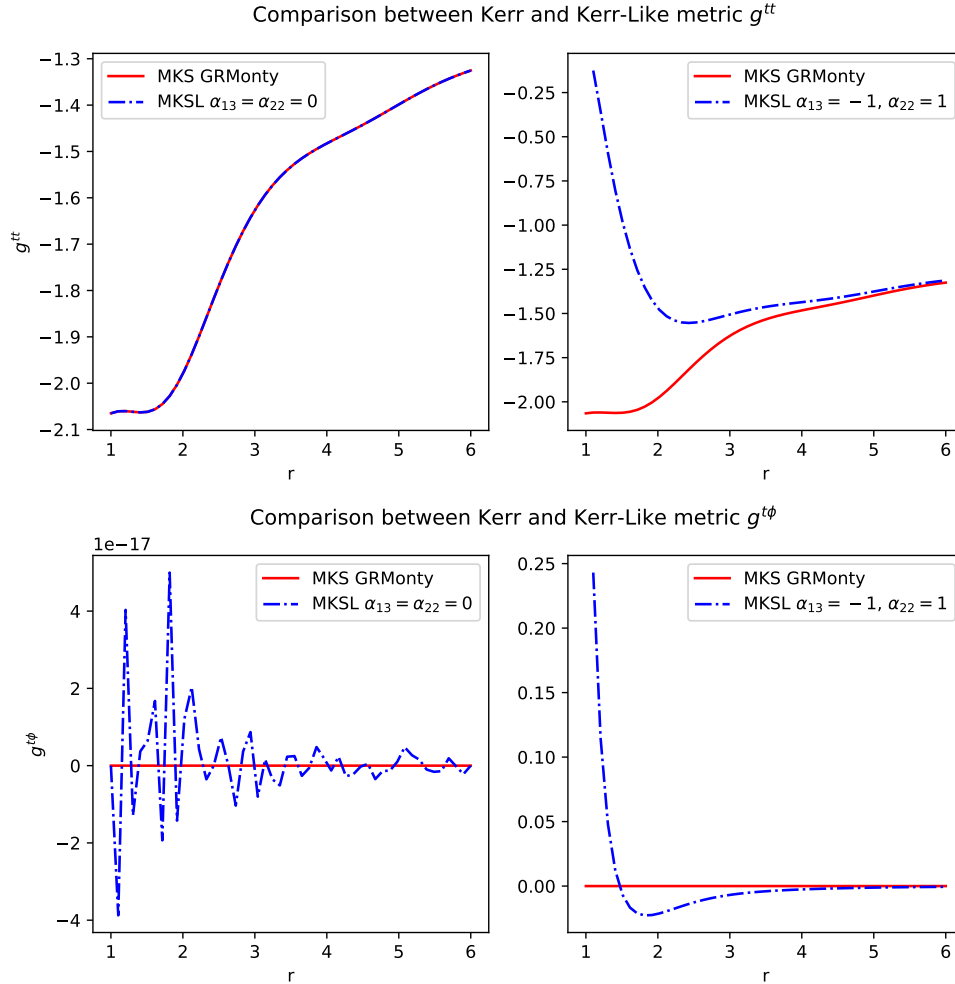


Figure 3.3.2: Comparison between the contravariant components g^{tt} and $g^{t\phi}$ of the Kerr and Kerr-Like metrics. In the left panel of the figures, the comparison can be observed when the Kerr-Like metric has its free deviations set to zero (i.e., $\alpha_{13} = \alpha_{22} = 0$), reducing it to the Kerr metric. In the right panel of the figure, the difference is evident when the free deviations are activated to first order in both functions $A_1(r)$ and $A_2(r)$, such that they have their maximum deviation values (i.e., $\alpha_{13} = -1$ and $\alpha_{22} = 1$).

On the other hand, RAPTOR features an algorithm for performing the calculation of the connection (i.e., Christoffel symbols in this case) numerically. We initially used this algorithm to test the proper functioning of image simulations with the implementation of the metric described earlier. While the

numerical calculation of the connection yielded good results, it proved to be inefficient, causing the simulation to consume excessive computational time and preventing us from working with high resolutions. Therefore, considering the favorable analytical behavior of the Kerr-Like metric, we calculated its connection analytically for implementation in RAPTOR. This expression can be found in Appendix A2. This significantly accelerated the code, enabling us to conduct numerous tests with free deviation parameters, resulting in images similar to those observed in Figure (3.3.3).

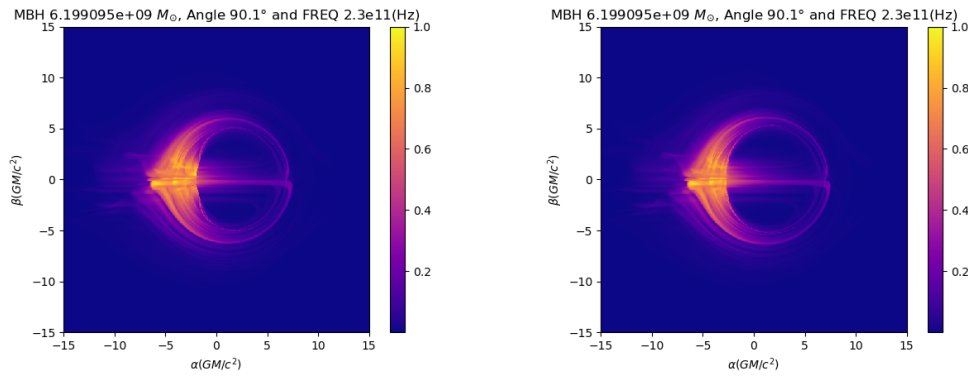


Figure 3.3.3: GRMHD simulation for a SMBH with a mass similar to M87* and spin $a = 0.9375 M$. In the left part of the figure a simulation of the Kerr-Like metric with deviation parameter $\alpha_{13} = -1$ and to compare this in the right part of the figure a simulation of a Kerr metric, with angle of view $i = 90^\circ$ (i.e edge-on).

Tests that will be shown in Chapter (4), where a subsequent analysis of these will be conducted through the study of their intensity profile, allowing us to calculate quantifiable shadow characteristics such as its diameter, displacement, and asymmetry. The methodology for performing these calculations will be presented in the following two sections.

3.4 Intensity profile

In the current section, I will present the use of intensity profiles for analyzing images of black holes. Given the nature of accretion disks, where intensity varies significantly from outside the black hole to the event horizon and is affected by effects such as gravitational redshift and disk velocity, quantification of this variation becomes essential. Particularly because ray tracing simulations

for black holes provide us with comprehensive intensity information around the black hole in each pixel of the image.

Therefore, drawing inspiration from works conducted by (Gralla et al., 2019, 2020; Narayan et al., 2019; Bronzwaer et al., 2021; Bandyopadhyay et al., 2021, 2023), we conducted a study of intensity profiles using a Python script developed by Javier Lagunas and Javier Pedreros for utilization with the output of GRTrans (Dexter, 2016), which was modified to work with the output of the RAPTOR code. The algorithm operates as follows: it reads the intensity output of the image in each pixel, extracts its values along a minimally sized rectangle following a straight line across the two-dimensional image of the black hole. The straight line representing the rectangle is set to a specific value for the β axis in the image, along with all possible values of α . In this case, for a given $\beta = 0$, an angle $\varphi = 0$ is assigned to the straight line defining the angle of the rectangle with respect to the abscissa (see the plots in the below part of the Fig. (3.4.1)).

To perform a thorough analysis of these intensity profiles, a study was conducted across different angles φ in order to understand the behavior of the total image intensity from different axes. This allows us to quantify the location of the event horizon, identify its peak intensity value associated with redshift, as well as examine the shadow's diameter, its displacement from the central image axis, and the image deformation by quantifying its asymmetry.

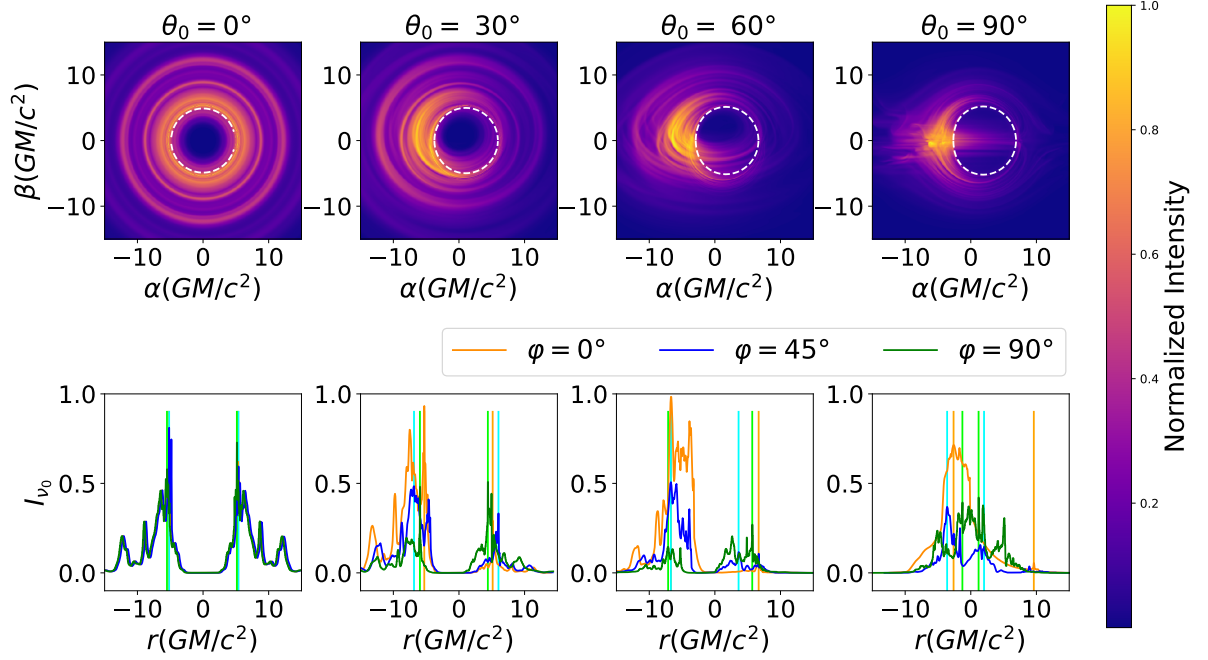


Figure 3.4.1: An Example of four simulated images of a Kerr BH with the mass of Sgr A* (*Above images*) with the normalized intensity color bar and below each image the intensity profiles for three different angles of intensity measurement values. The *white dashed line* represents the circular orbit of the photon ring for a Kerr BH, included for the purpose of comparison with the shadow.

In the following section, I will explain how values of asymmetry, displacement, and shadow diameter are quantified using intensity profiles and the equations found in the literature for these values.

3.4.1 Displacement, Diameter, and Asymmetry

In order to quantify the shadows of the black holes through the intensity profiles and to observe how much this shadow changes while studying the Kerr-Like spacetime with certain deviation parameters in comparison with the Kerr spacetime, the definition of displacement in the x -axis, given by [Johannsen \(2013a\)](#), is

$$D \equiv \frac{|x_{max} - x_{min}|}{2}, \quad (3.4.1)$$

where x_{max} and x_{min} , are the locations of the two maximum peaks for the normalized intensity in a horizontal intensity profile. Similarly, it is possible to define an offset in the vertical direction. From here the average radius can be defined as,

$$\langle \bar{R} \rangle \equiv \frac{1}{2\pi} \int_0^{2\pi} \bar{R} d\alpha, \quad (3.4.2)$$

where

$$\bar{R} \equiv \sqrt{(x' - D_x)^2 + (y' - D_y)^2}. \quad (3.4.3)$$

Therefore the average diameter is given by $L \equiv 2\langle \bar{R} \rangle$. Thus, the asymmetry of the photon ring is

$$A \equiv 2\sqrt{\frac{\int_0^{2\pi} (\bar{R} - \langle \bar{R} \rangle)^2 d\alpha}{2\pi}}. \quad (3.4.4)$$

Given the diameter, asymmetry, and displacement equations used by Johanssen, we are aware that this theoretical description is exclusively constructed and calculated under the assumption that the exterior of the black hole is surrounded by infinite light sources. This is distinct from our framework, where the luminous source is an accretion disk with its own dynamics around the black hole. While this holds true, it is possible to employ these equations in the images to obtain an approximate quantification of these values, thus providing us with an insight into how well a simple theoretical framework aligns with practical measurements in observations or simulations of a black hole. This also offers an approximate understanding of more fundamental values such as the black hole's spin and mass.

These values were computed for the images obtained in RAPTOR by studying intensity profiles across all angles of the image, ranging from $[0, 360]$ degrees. This approach allows us to calculate the approximate diameter of the image by identifying the points of maximum and minimum intensity in the profile, which define the inflection point where the black hole's shadow and hence event horizon initially appear. Averaging these values for each angle yields an approximate image diameter.

Furthermore, with the diameter value established, it becomes feasible to calculate the image displacement and asymmetry for each angle φ , enabling us to average these values and derive an overall approximate value for each of them (see Fig. (3.4.2)).

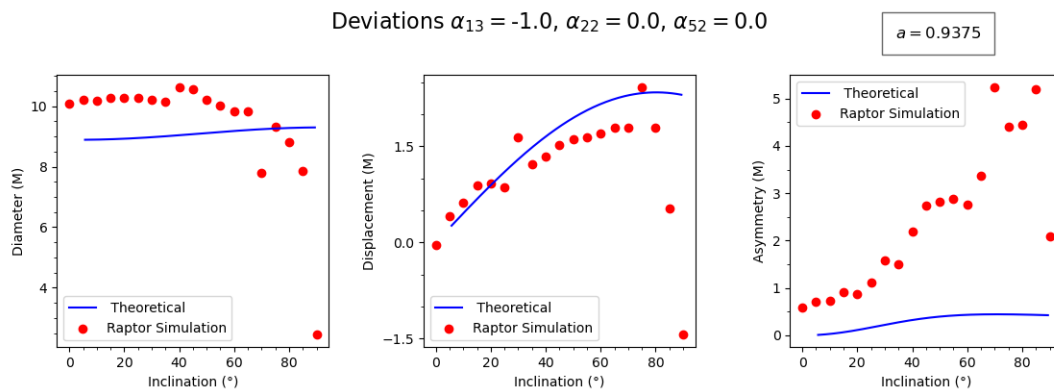


Figure 3.4.2: (Blue line) is the fit calculated by Johanssen and the (Red dots) are the values obtained by a post-processing data of the SMBH with the mass of $M87^*$ and spin $a = 0.9375M$ of the GRMHD simulated image.

In the following section, these values and intensity profiles will be analyzed more comprehensively, associating them with specific cases in order to quantify different metric deviations and compare them with the Kerr metric. This aims to gauge the effectiveness of measuring these deviations in simulations and potential observations.

Chapter 4

Effects of the deviations from the Kerr metric and GRMHD simulations

With the intention of studying and quantifying deviations from the Kerr metric in black hole images, this section presents a diverse range of simulations to quantify how these deviations affect the shadow. The study begins by examining the shape of the photon ring around the Kerr-Like black hole for deviation parameters $\alpha_{13} = [-1, 1]$, $\alpha_{22} = [-1, 1]$, and $\alpha_{52} = [-1, 1]$. Simulated images using RAPTOR for these deviations are generated for both a HARM-type disk model and an analytical thin disk model by Novikov-Thorne. The intensity profiles, diameter, displacement, and asymmetry are quantified and compared with the photon ring results calculated and adjusted by (Johannsen, 2013a). These are further compared with potential observations.

Additionally, a similar analysis is conducted for a slowly rotating solution of a black hole in modified Chern-Simons gravity theory, considering different values of the coupling parameter $\zeta_{CS} = [0, 1]$, noting that the theory is effective only for $\zeta_{CS} \ll 1$. Coupling values associated with observational measurements of extreme objects like quasars and AGN (Active Galactic Nuclei) are also considered. This section associates the analysis with the Kerr-Like metric and presents thin disk simulations for different coupling parameters of the theory.

Lastly, a new perturbative result for a slowly rotating black hole is shown in the context of α' -corrected gravity, which is a low-energy limit of string theory. The metric is obtained in Boyer-Lindquist and Kerr-Schild coordinates, and the possibility of separability for the Hamilton-Jacobi equations is introduced. This sets the stage for future work involving the analytical integration of null geodesics and conducting thin disk simulations to analyze different coupling parameter values.

4.1 Kerr-Like metric simulations

To show you how deviations from the Kerr metric can affect the shadow of the black hole, first, we analyze the effect of the Kerr Like metric at the first order in the free deviation functions for a circular photon ring orbit. This shadow can be obtained under the assumption that there are infinite light sources and solving the equations

$$R(r) = 0 \quad \text{and} \quad \frac{dR(r)}{dr} = 0, \quad (4.1.1)$$

where

$$R(r) = [(r^2 + a^2)A_1(r) - aA_2(r)\tilde{\xi}]^2 - \Delta[(\tilde{\xi} - a)^2 + \eta], \quad (4.1.2)$$

and where the axis for the image are $[\alpha, \beta]$ when $r_0 \rightarrow \infty$, such that

$$\alpha = -\frac{\tilde{\xi}}{\sin i'}, \quad (4.1.3)$$

$$\beta = \pm \sqrt{\Theta(i)}, \quad (4.1.4)$$

here $\Theta(i) = \eta + a^2 \cos^2 i - \tilde{\xi}^2 \cot^2 i$ and η and $\tilde{\xi}$ can be obtained by solving the equations (4.1.1) with $R(r)$ given for (4.1.2).

Considering the low minimum limit of the deviations like (Johannsen, 2013a), i.e, when:

$$\alpha_{13} > -\frac{(M + \sqrt{M^2 - a^2})^3}{M^3}, \quad (4.1.5)$$

$$\alpha_{22} > -\frac{(M + \sqrt{M^2 - a^2})^2}{M^2}, \quad (4.1.6)$$

$$\alpha_{52} > -\frac{(M + \sqrt{M^2 - a^2})^2}{M^2}, \quad (4.1.7)$$

$$\epsilon_3 > -\frac{(M + \sqrt{M^2 - a^2})^3}{M^3}. \quad (4.1.8)$$

In the case of the spin value $a = 0.9375$, these values are $\epsilon_3 = \alpha_{13} > -2.45$ and $\alpha_{22} = \alpha_{52} > -1.82$.

The photon rings can be graphically represented for these deviations as shown in Figs. (4.1.1-4.1.2).

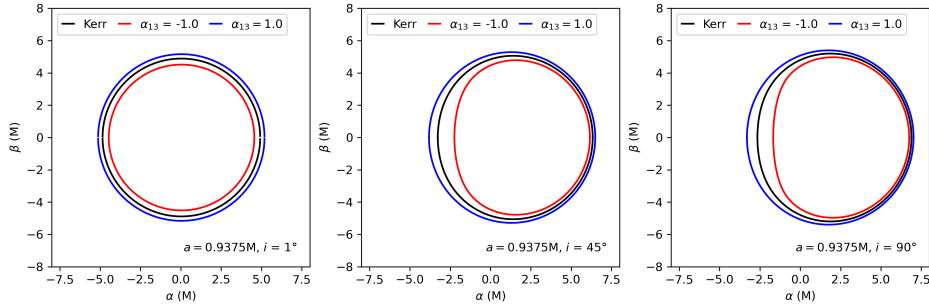


Figure 4.1.1: Comparison between a Kerr photon ring for a circular orbit (*black line*) for a BH with spin $a = 0.9375 M$ and Kerr-Like with the deviation parameters $\alpha_{13} = [-1, 1]$ (*red and blue line*), respectively and angle of view $i = [1^\circ, 45^\circ, 90^\circ]$.

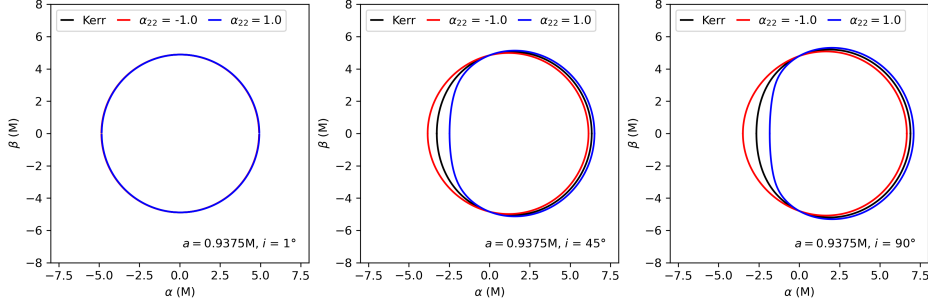


Figure 4.1.2: Comparison between a Kerr photon ring for a circular orbit (*black line*) for a BH with spin $a = 0.9375 M$ and Kerr-Like with deviation parameters $\alpha_{22} = [-1, 1]$ (*red and blue line*), respectively and angle of view $i = [1^\circ, 45^\circ, 90^\circ]$.

This case is for the limit deviations values $\alpha_{13} = [-1, 1]$ and $\alpha_{22} = [-1, 1]$. We consider just these two deviation parameters because the Keplerian orbits of the circular photon rings around the BH (i.e Eq. (4.1.2)) is independent of the deviation function $A_5(r)$ and also because all terms that are affected by the parameter ϵ_3 also contain the rest mass of the particle which are vanish for photons geodesics.

4.1.1 HARM model simulations

To study and understand the impact of Kerr deviations on radiation transport in GRMHD-type simulations, where snapshots of physical quantities from the disk model are used based on the dump file extracted from HARM, it is necessary to utilize the same input file. This is regardless of the fact that deviations from Kerr geometry also alter the structure of the accretion disk and the observable image.

Therefore, for the purpose of our study, we used the same dump file for both the Kerr and Kerr-Like metrics.

We conducted multiple simulations of a supermassive black hole with the mass of M87* in Kerr-Like spacetime, employing a synchrotron model for emissivity, where the absorption coefficient follows the Kirchhoff's law.

The deviation functions for these simulations were truncated to the first order in deviation, with the intention of comparing them to the work done by Tim Johannsen (Johannsen, 2013a). The free deviation parameters used in the test were $\alpha_{13} \in [-1, 1]$, $\alpha_{22} \in [-1, 1]$, and $\alpha_{52} \in [-1, 1]$. The values of these parameters are slightly larger than the lower limits for these parameters to first order, as given by the expression Eqs. (4.1.5).

The simulations carried out to observe the effect of the deviations were conducted for deviation values α ranging from -1 to 1 , with steps of 0.1 between each of these values.

I will present below the results in two different ways, with the intention of better illustrating the simulations, avoiding redundancy, and preventing overly extensive outcomes. I will display the simulations of the images for two different deviation values, namely, $[-1, 1]$, considering that the lower value is close to the previously calculated lower limit. On the other hand, to observe the differences produced by the simulations, I will compare the values of diameter, displacement, and asymmetry for four different deviation values, which are $[-1, -0.5, 0.5, 1]$.

The table (4.1.1) displayed below shows the input values used in RAPTOR to perform the simulation of these images.

Table 4.1.1: Setup for the simulation of the SMBH with the distance and mass of M87*

Parameter	Value
M_{BH}	$6.2 \times 10^9 M_{\odot}$
Distance	16.9 Mpc
a	$0.9375 M$
r_{cam}	$10^4 R_g$
Range for $[\alpha, \beta]$	$[-15, 15] R_g$
Resolution $[x, y]$	500 px
Frequency	230 GHz
Inclination ($^{\circ}$)	0, 30, 60, 90
T_p/T_e	1.0

4.1.1.1 Deviation parameter α_{13}

Starting with the value of $\alpha_{13} = -1$ and taking cues from the intuitive mental visualization provided in (4.1.1). The simulations are displayed in Fig. (4.1.3).

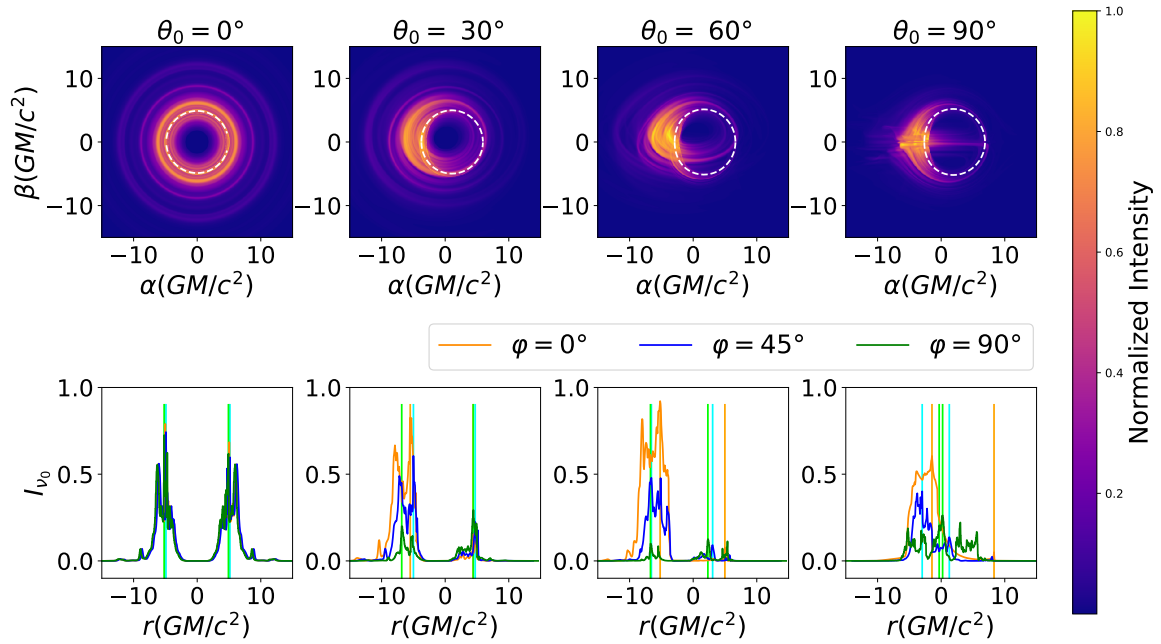


Figure 4.1.3: This figure displays a GRMHD simulation of a Kerr-Like black hole, which has a mass similar to that of $M87^*$ (with a spin of $a = 0.9375M$ and a deviation parameter $\alpha_{13} = -1$). In the upper panel, intensity maps are presented from four different viewing angles ($0, 30, 60, 90$ degrees). These maps show us how the shape of the black hole’s shadow and the intensity of the disk change as we vary the viewing angle. The white line on each map represents the contour of the photon ring in a Kerr SMBH, allowing us to compare it with the shadow in this Kerr-Like metric. In the lower panel, intensity profiles corresponding to the upper images are shown. Each image has three intensity profiles taken from different angles. By observing how the height and location of the peak points change along the x-axis in these profiles, we can perform subsequent analysis of the diameter, displacement, and asymmetry of the black hole’s shadow.

For a direct analysis of these images, it is useful to examine them based on Figure (4.1.3), as it can be observed that the upper panel contains images of the SMBH from 4 different viewing angles, ranging from face-on to edge-on. In these images, a color map of intensities in each pixel of the black hole image, as seen by the observer, is depicted. What is visible is the accretion disk around this black hole, and the intensity is normalized with respect to its maximum value. The *white dashed line* represents the circular orbit of the photon ring for a Kerr BH, included for the purpose of comparison with the shadow in our

simulation of the Kerr-like metric.

Additionally, the lower section displays normalized intensity profiles obtained from data captured at three angles φ , namely, from a vertical line, a horizontal line, and one at 45° , in each of the upper images. Vertical lines mark the intensity peaks, allowing for the calculation of x_{max} and x_{min} .

Now, for the parameter $\alpha_{13} = 1.0$, the simulations are displayed in Fig. (4.1.4).

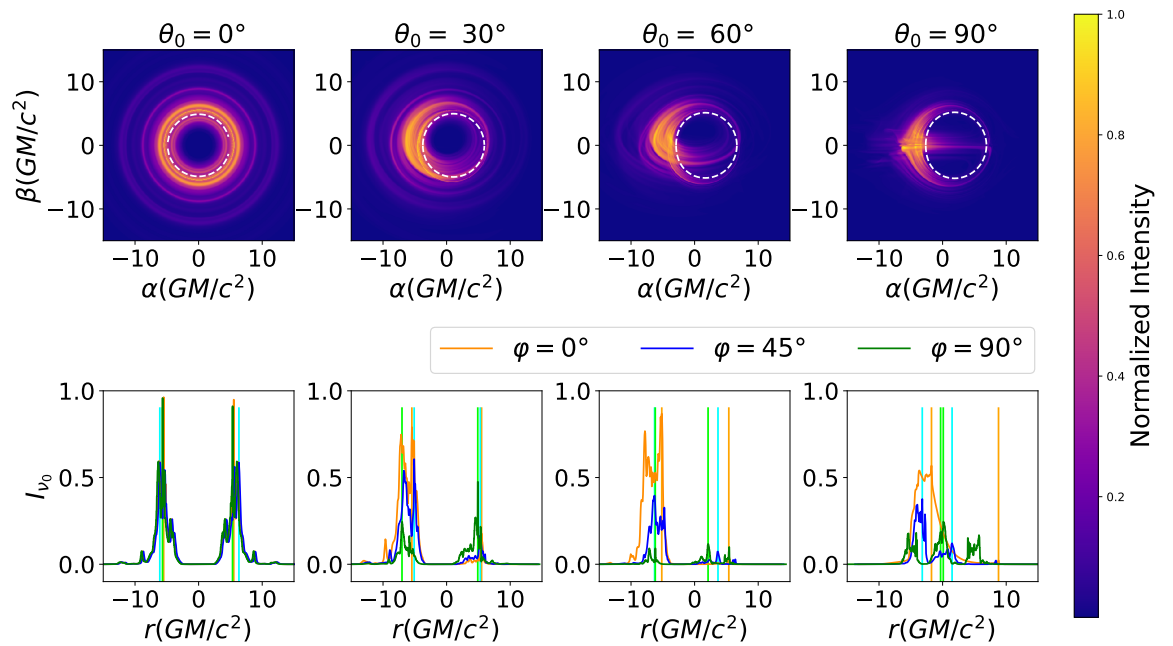


Figure 4.1.4: GRMHD simulation of a Kerr-Like black hole, which has a mass similar to that of $M87^*$ (with a spin of $a = 0.9375M$ and a deviation parameter $\alpha_{13} = 1$). In the upper panel, intensity maps are presented from four different viewing angles ($0, 30, 60, 90$ degrees). These maps show us how the shape of the black hole's shadow and the intensity of the disk change as we vary the viewing angle. The white line on each map represents the contour of the photon ring in a Kerr SMBH, allowing us to compare it with the shadow in this Kerr-Like metric. In the lower panel, intensity profiles corresponding to the upper images are shown. Each image has three intensity profiles taken from different angles. By observing how the height and location of the peak points change along the x-axis in these profiles, we can perform subsequent analysis of the diameter, displacement, and asymmetry of the black hole's shadow.

The two previously shown figures display two different axes of the same deviation parameter. If examined closely, one can discern the effect on the

geometry of the black hole's shadow. This effect is as expected when relating it to the analysis of photon rings shown in Fig. (4.1.1 - 4.1.2).

We notice that, in comparison to the Kerr photon ring, the difference is slight but nonetheless significant. To perceive the effect of these deviations more clearly, we conduct a subsequent analysis of these images, calculations for asymmetry, diameter, and displacement were performed based on intensity profiles, as described in section (3.4.1), and then compared with the fittings computed by Tim Johannsen (Johannsen, 2013a) for the Kerr-like metric. In following figures (4.1.5), these values can be observed for each viewing angle towards the black hole, spanning from $[0^\circ, 90^\circ]$ with steps of 5° between each value.

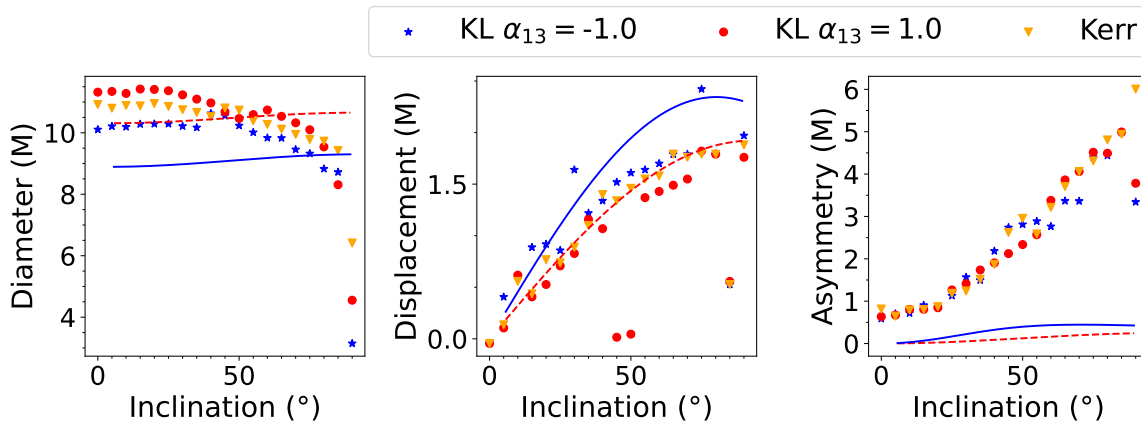


Figure 4.1.5: Comparison of diameter, displacement, and asymmetry values. It includes the fit calculated by Johannsen (2013a) (Blue line) for a Kerr-Like black hole with a deviation parameter $\alpha_{13} = -1$ (Red dashed line), $\alpha_{13} = 1$, and a Kerr-Like simulation (Red dots and Blue stars) of a black hole with these deviation parameters, respectively, alongside the simulation of a Kerr black hole (Orange triangles). The graph illustrates how these values change as the viewing angle varies from 0 to 90 degrees. It shows that the first two cases exhibit similar trends, while the last one behaves differently. It is noteworthy that there is a clear distinction in the values that consider deviations from the standard Kerr metric.

Firstly, in Figure (4.1.5), we highlight that in the case of the diameter and displacement of the shadow, the values are close to obtained by the fits from (Johannsen, 2013a). However, this is not the case for asymmetry, where we

notice that in the simulations its value increases significantly compared to the fitting as we change the viewing angle.

Regarding the comparison with simulations performed for the Kerr metric, a clear difference can be observed between the diameters and displacements of the shadow. In the case of the diameter, these values are closer to each other when viewing the black hole at an angle of approximately 45° , with the greatest difference noticeable at 90° . On the other hand, concerning the displacement of the shadow from the center of the image, we notice that the values overlap more frequently than for the diameter. A greater displacement is presented for $\alpha_{13} = -1$ as we approach the view in the plane of the disk, and for $\alpha_{13} = 1$, a lesser displacement, in comparison to the corresponding values for the Kerr metric, which lie right between these two deviations.

Furthermore, we observe that for the displacement, there are many values that deviate from the naturally projected curve. This is likely due to the fact that as we change the viewing angle from a face-on angle to an edge-on angle, the structure of the disk starts to obstruct the sampling of intensity, consequently affecting the geometry of the viewed shadow. Therefore, this aspect becomes particularly important when quantifying these shadow values.

Interestingly, in this model, the viewing angle towards the black hole seems not to influence the diameter values significantly and only slightly affects the case of asymmetry.

Finally, we observe that the differences in asymmetry values for angles near face-on are minimal. However, as we approach the edge-on angle, these differences become more evident and significant. We also notice that asymmetry tends to increase as we change the view of the black hole towards the plane of the disk. It is deduced that in this view, we will encounter more pronounced differences in the geometry of the shadow, thus indicating that this is where the most significant variations in shadow characteristics will be observed.

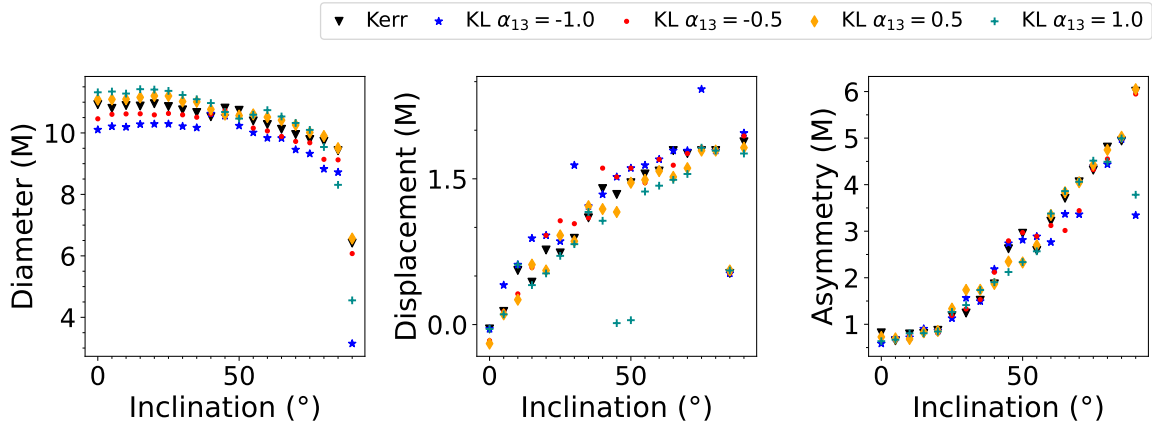


Figure 4.1.6: Comparison of how the values of diameter, displacement, and asymmetry change as the viewing angle varies from 0 to 90 degrees in simulations of a Kerr-Like black hole with deviation parameters $\alpha_{13} = -1$ (Blue stars), $\alpha_{13} = -0.5$ (Red dots), $\alpha_{13} = 0.5$ (Orange diamonds), $\alpha_{13} = 1$ (Dark cyan plus sign), and in the simulation of a Kerr black hole (Black triangles). Noticeable differences are observed between the deviated values and the background value for the Kerr simulation, although all differences are slight compared to Kerr.

In Figure (4.1.6), the values of diameter, displacement, and asymmetry are compared for the four deviations $\alpha_{13} = [-1, -0.5, 0.5, 1]$. It is clear that for the diameter, the difference among the four deviations is evident, with the shadow's diameter increasing as the deviation grows. On the other hand, in terms of displacement, the difference between each of the values is less pronounced, although we can still notice a distinction between the values $[-1, 1]$. The value of -1 exhibits a more shifted shadow compared to the center of the image, while the value of 1 displays a lesser degree of displacement. Specifically, the initial angles ranging from $0 - 45^\circ$ are the ones with less displacement when compared to the data analyzed for angles greater than these.

4.1.1.2 Deviation parameter α_{22}

In order to continue with the simulations for the different deviation parameters of the Kerr-Like metric, we proceed to conduct similar simulations to the previous ones. However, this time, we focus on the deviation parameter

α_{22} . We use values of $[-1, 1]$ to showcase the simulations and values of $[-1, 0.5, -0.5, 1]$ for a subsequent analysis of the diameter, displacement, and asymmetry values of the shadow.

Therefore, for $\alpha_{22} = -1$, the simulation would appear as displayed in Fig. (4.1.7).

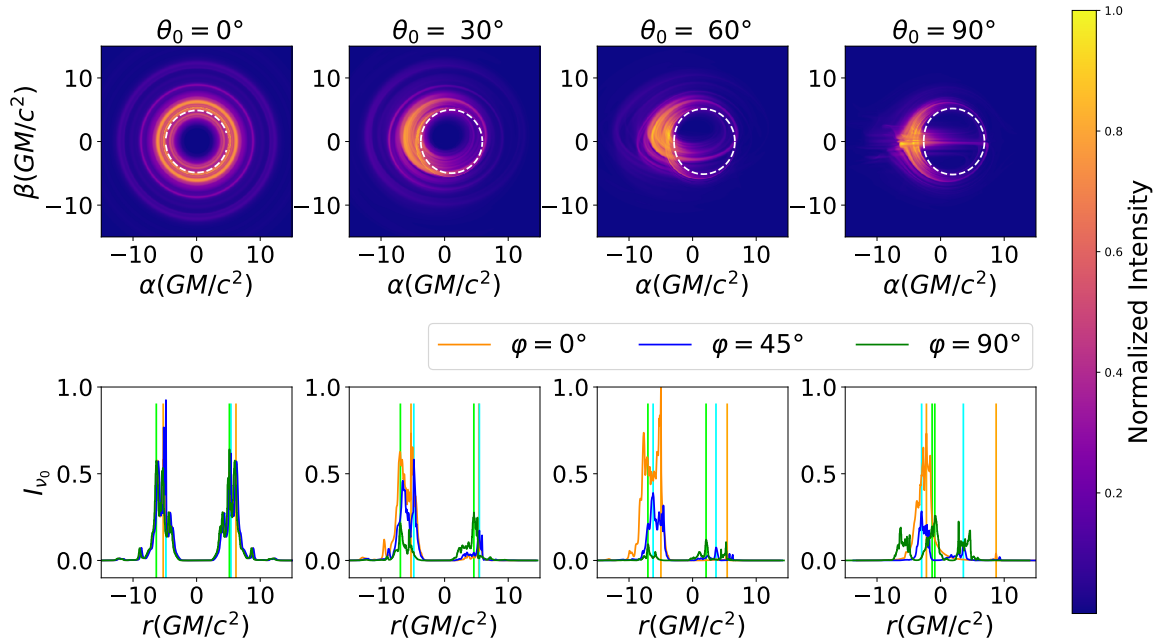


Figure 4.1.7: GRMHD simulation of a Kerr-Like black hole, which has a mass similar to that of M87* (with a spin of $a = 0.9375M$ and a deviation parameter $\alpha_{22} = -1$). In the upper panel, intensity maps are presented from four different viewing angles (0, 30, 60, 90 degrees). These maps show us how the shape of the black hole's shadow and the intensity of the disk change as we vary the viewing angle. The white line on each map represents the contour of the photon ring in a Kerr SMBH, allowing us to compare it with the shadow in this Kerr-Like metric. In the lower panel, intensity profiles corresponding to the upper images are shown. Each image has three intensity profiles taken from different angles. By observing how the height and location of the peak points change along the x-axis in these profiles, we can perform subsequent analysis of the diameter, displacement, and asymmetry of the black hole's shadow.

And also, for $\alpha_{22} = 1$ value, we obtain the results as shown in Fig. (4.1.8).

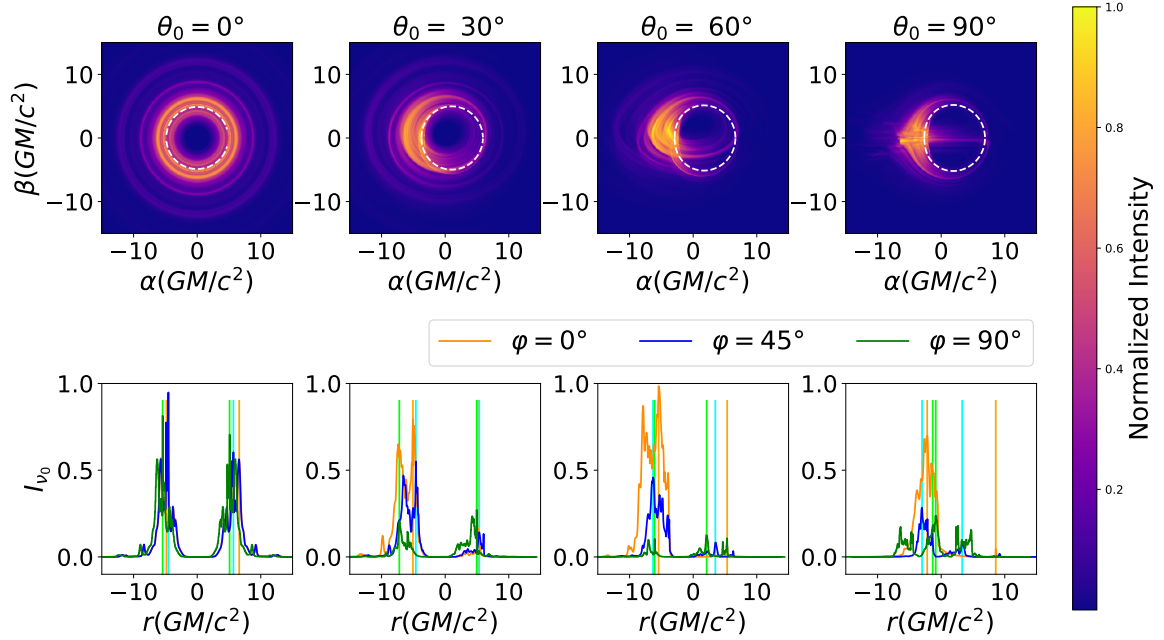


Figure 4.1.8: GRMHD simulation of a Kerr-Like black hole, which has a mass similar to that of $M87^*$ (with a spin of $a = 0.9375M$ and a deviation parameter $\alpha_{22} = 1$). In the upper panel, intensity maps are presented from four different viewing angles (0, 30, 60, 90 degrees). These maps show us how the shape of the black hole’s shadow and the intensity of the disk change as we vary the viewing angle. The white line on each map represents the contour of the photon ring in a Kerr SMBH, allowing us to compare it with the shadow in this Kerr-Like metric. In the lower panel, intensity profiles corresponding to the upper images are shown. Each image has three intensity profiles taken from different angles. By observing how the height and location of the peak points change along the x-axis in these profiles, we can perform subsequent analysis of the diameter, displacement, and asymmetry of the black hole’s shadow.

Here we can observe a similar effect to the case of α_{13} for the BH shadow and the deviation parameters $\alpha_{22} = [-1, 1]$.

However, by analyzing this through the values of diameter, displacement, and asymmetry, we notice that the differences among them are smaller. The change in the image’s diameter is almost imperceptible at low viewing angles under 60° . Similarly, the displacement is minor compared to the Kerr metric.

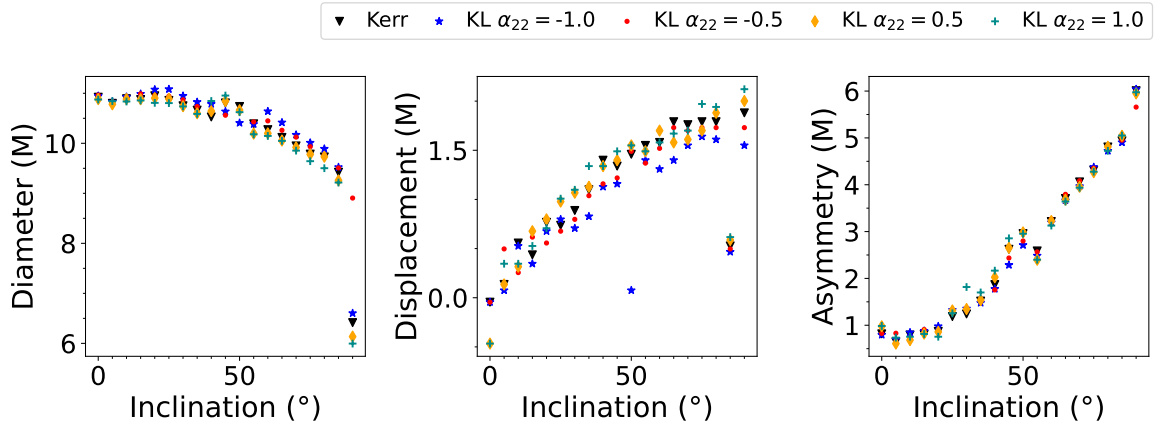


Figure 4.1.9: Comparison of the diameter, displacement, and asymmetry values for a Kerr-Like BH simulations with deviation parameters $\alpha_{22} = -1$ (Blue stars), $\alpha_{22} = -0.5$ (Red dots), $\alpha_{22} = 0.5$ (Orange diamonds), $\alpha_{22} = 1$ (Dark cyan plus sign), and in the simulation of a Kerr black hole (Black triangles) and how these values change as the viewing angle varies from 0 to 90 degrees, showing noticeable differences between the deviated values and the background value for the Kerr simulation, although all differences are slight compared to Kerr.

We notice that while the displacements for $\alpha_{22} = -1$ and $\alpha_{22} = 1$ can be distinguishable, with one having a smaller displacement than the other. In comparison to Kerr, $\alpha_{22} = 1$ behaves quite similarly at angles less than 50° , and $\alpha_{22} = -1$ tends to behave similarly to Kerr for angles greater than 50° .

On the other hand, the asymmetry values for either of the deviations closely resemble the values found for the simulations of the Kerr metric.

4.1.1.3 Deviation parameter α_{52}

As mentioned earlier, the deviations provided by the free function $A_5(r)$ do not, at first glance, affect the shadow image for circular photon orbits. Therefore, in practical terms, we have chosen to study it only for the value that approaches the lower limit, in order to see if non-circular photon orbits exhibit any significant changes in the image. Thus, for $\alpha_{52} = -1$, the image appears as shown in Fig. (4.1.10).

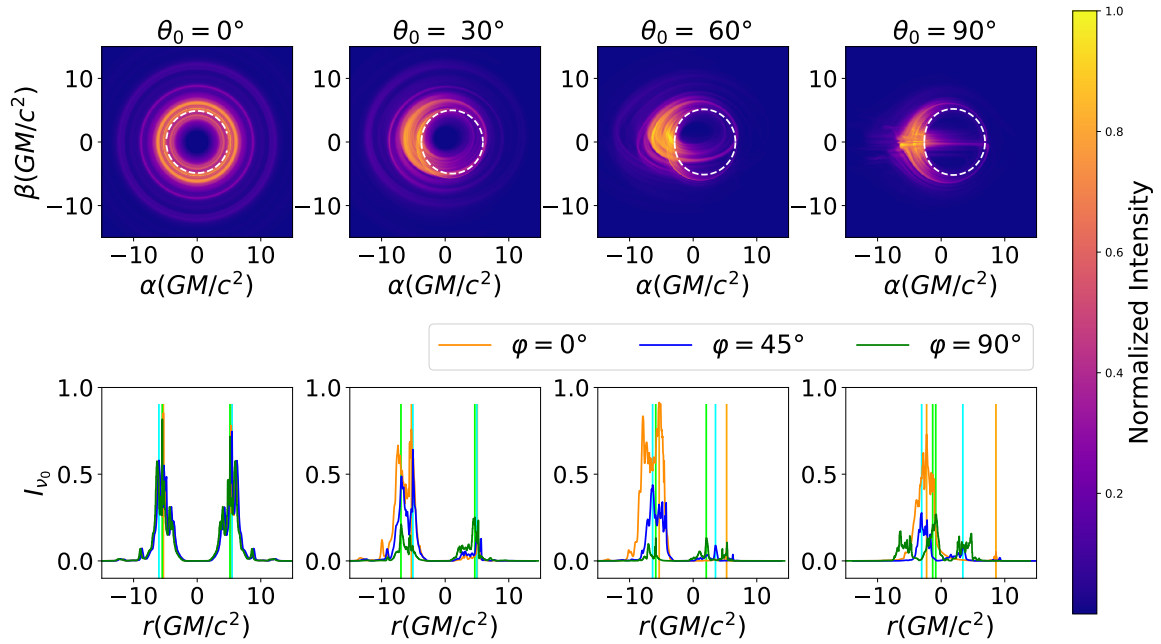


Figure 4.1.10: GRMHD simulation of a Kerr-Like black hole, which has a mass similar to that of $M87^*$ (with a spin of $a = 0.9375M$ and a deviation parameter $\alpha_{52} = -1$). In the upper panel, intensity maps are presented from four different viewing angles ($0, 30, 60, 90$ degrees). These maps show us how the shape of the black hole's shadow and the intensity of the disk change as we vary the viewing angle. The white line on each map represents the contour of the photon ring in a Kerr SMBH, allowing us to compare it with the shadow in this Kerr-Like metric. In the lower panel, intensity profiles corresponding to the upper images are shown. Each image has three intensity profiles taken from different angles. By observing how the height and location of the peak points change along the x -axis in these profiles, we can perform subsequent analysis of the diameter, displacement, and asymmetry of the black hole's shadow.

Upon conducting further analysis for the values of diameter, displacement, and asymmetry, in cases where $\alpha_{52} = [-1, -0.5, 0.5, 1]$, it can be observed that non-circular orbits do have an impact on these values (see Fig. 4.1.11). However, these effects are not substantial enough to yield a significant difference compared to the values obtained for the Kerr metric.

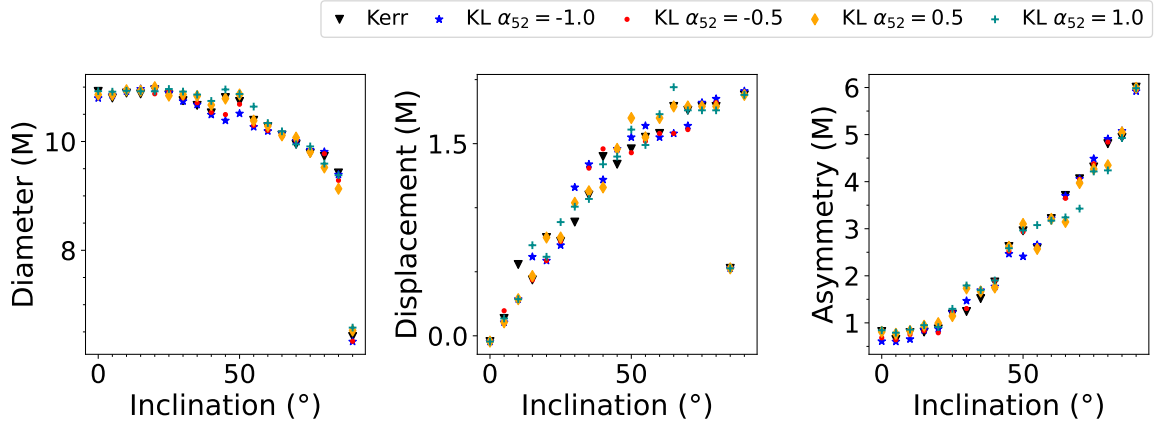


Figure 4.1.11: Comparison of how the values of diameter, displacement, and asymmetry change as the viewing angle varies from 0 to 90 degrees in simulations of a Kerr-Like black hole with deviation parameters $\alpha_{52} = -1$ (*Blue stars*), $\alpha_{52} = -0.5$ (*Red dots*), $\alpha_{52} = 0.5$ (*Orange diamonds*), $\alpha_{52} = 1$ (*Dark cyan plus sign*), and in the simulation of a Kerr black hole (*Black triangles*). Noticeable differences are observed between the deviated values and the background value for the Kerr simulation, although all differences are slight compared to Kerr.

4.1.1.4 Sgr A* case

Now, with the intention of studying this model from a more realistic perspective, the input parameters are reconfigured to attempt to model the SMBH of Sgr A*. This aligns well with the GRMHD model we are using, so the parameters are based on (Mościbrodzka et al., 2009) for the tests, as they suggest that this modeling profile is more related to the sub-mm spectral observations (α).

Therefore, we proceed to conduct the same previous analysis, this time using the appropriate input parameters for the Sgr A* model as given in Tab. (4.1.2).

Table 4.1.2: Setup for the simulation of the SMBH with the distance and mass of Sgr A*

Parameter	Value
M_{BH}	$4.5 \times 10^6 M_{\odot}$
Distance	8.5 kpc
a	$0.9375 M$
r_{cam}	$10^4 R_g$
Range for $[\alpha, \beta]$	$[-15, 15] R_g$
Resolution $[x, y]$	500 px
Frequency	230 GHz
Inclination ($^{\circ}$)	0, 30, 60, 90
T_p/T_e	3.0

The essential differences between this case and the previous one are that the mass and distance to the black hole are different, particularly in this scenario, drawing from (Mościbrodzka et al., 2009) and using data from the Sgr A* SMBH. Additionally, the parameter altered for the Harm model is the ratio of proton temperature to electron temperature, which is set to $T_p/T_e = 3.0$ which makes the simulation be dominated by the disk.

With the previous results in mind, and noticing that the deviations in the Kerr metric where the change in the shadow's geometry becomes more pronounced are $\alpha_{13} = [-1, 1]$ and $\alpha_{22} = [-1, 1]$, as α_{52} only slightly affects the shadow's geometry, we will focus on the lower limits of these deviations. Our intention is to quantify and compare these lower limits with the results previously obtained for M87*.

So, first for $\alpha_{13} = -1$ and $\alpha_{13} = 1$, we obtain the results given in Figs. (4.1.12-4.1.13)

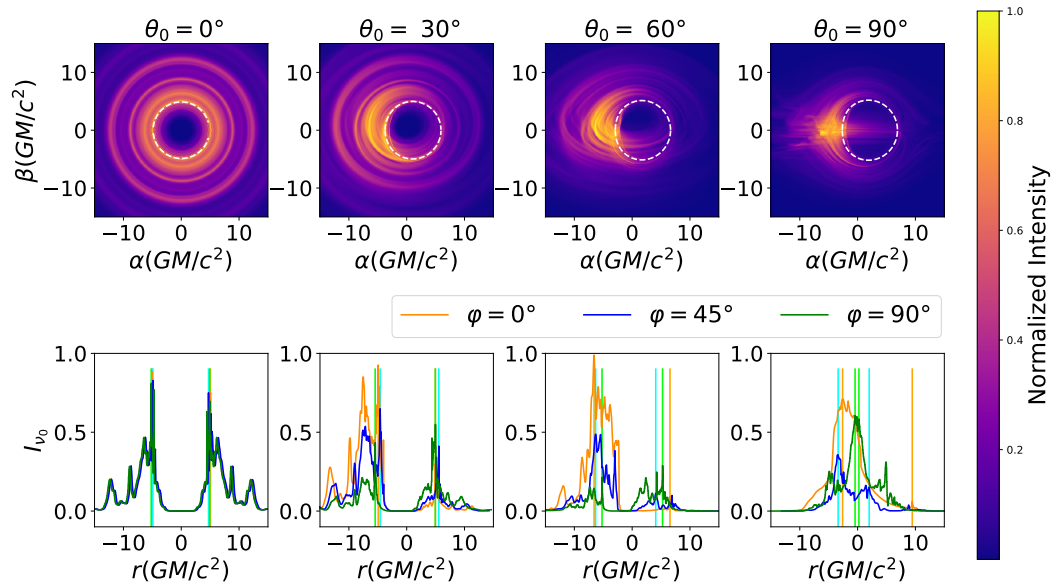


Figure 4.1.12: GRMHD simulation of a Kerr-Like black hole, which has a mass of $SgrA^*$ (with a spin of $a = 0.9375M$ and a deviation parameter $\alpha_{13} = -1$). In the upper panel, intensity maps are presented from four different viewing angles ($0, 30, 60, 90$ degrees). These maps show us how the shape of the black hole's shadow and the intensity of the disk change as we vary the viewing angle. The white line on each map represents the contour of the photon ring in a Kerr SMBH, allowing us to compare it with the shadow in this Kerr-Like metric. In the lower panel, intensity profiles corresponding to the upper images are shown. Each image has three intensity profiles taken from different angles. By observing how the height and location of the peak points change along the x-axis in these profiles, we can perform subsequent analysis of the diameter, displacement, and asymmetry of the black hole's shadow.

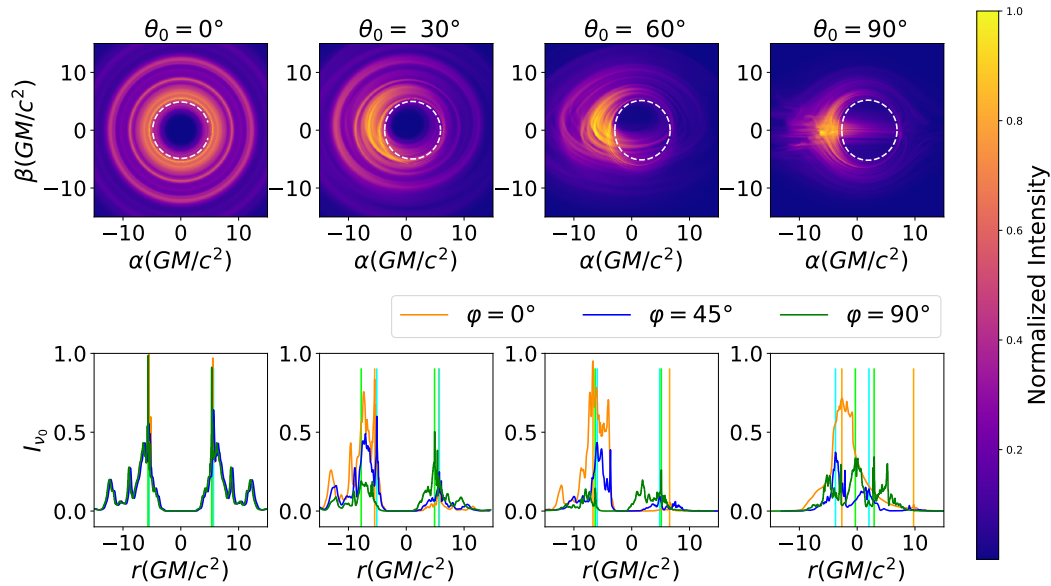


Figure 4.1.13: GRMHD simulation of a Kerr-Like black hole, which has a mass of $5grA^*$ (with a spin of $a = 0.9375M$ and a deviation parameter $\alpha_{13} = 1$). In the upper panel, intensity maps are presented from four different viewing angles ($0, 30, 60, 90$ degrees). These maps show us how the shape of the black hole's shadow and the intensity of the disk change as we vary the viewing angle. The white line on each map represents the contour of the photon ring in a Kerr SMBH, allowing us to compare it with the shadow in this Kerr-Like metric. In the lower panel, intensity profiles corresponding to the upper images are shown. Each image has three intensity profiles taken from different angles. By observing how the height and location of the peak points change along the x-axis in these profiles, we can perform subsequent analysis of the diameter, displacement, and asymmetry of the black hole's shadow.

And now for $a_{22} = -1$ and $a_{22} = 1$. These simulations are displayed in Figs. (4.1.14 - 4.1.15).

In these four figures (4.1.12 - 4.1.15), in the upper panel, we can find color maps of SMBH intensities from four different viewing angles, ranging from a frontal view to an edge-on view. These maps reveal the accretion disk around the black hole and its intensity normalized relative to its maximum value. It's also noticeable that, in contrast to the figures for the previous $M87^*$ model (4.1.3 - 4.1.8), the structure of the disk becomes more prominent, causing increased obstruction in the view as we approach the edge-on viewing angle.

In the lower section of the image, as in the previous cases, normalized intensity profiles from each of these color maps are shown, based on data captured at three different angles φ . The most significant difference between the two cases is the presence of the disk in this model, which also results in greater brightness throughout. As for the presence of deviations in these images, they remain noticeable to the naked eye; however, their presence is influenced by the disk's structure, and compared to the images for $M87^*$, the presence of these deviations is affected by the disk as well.

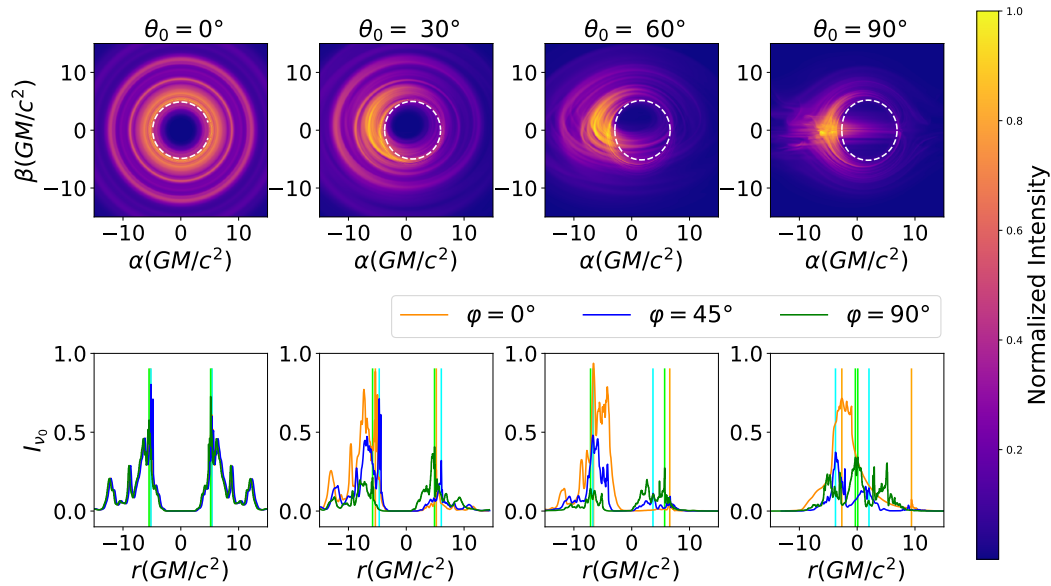


Figure 4.1.14: GRMHD simulation of a Kerr-Like black hole, which has a mass of $SgrA^*$ (with a spin of $a = 0.9375M$ and a deviation parameter $\alpha_{22} = -1$). In the upper panel, intensity maps are presented from four different viewing angles ($0, 30, 60, 90$ degrees). These maps show us how the shape of the black hole's shadow and the intensity of the disk change as we vary the viewing angle. The white line on each map represents the contour of the photon ring in a Kerr SMBH, allowing us to compare it with the shadow in this Kerr-Like metric. In the lower panel, intensity profiles corresponding to the upper images are shown. Each image has three intensity profiles taken from different angles. By observing how the height and location of the peak points change along the x-axis in these profiles, we can perform subsequent analysis of the diameter, displacement, and asymmetry of the black hole's shadow.

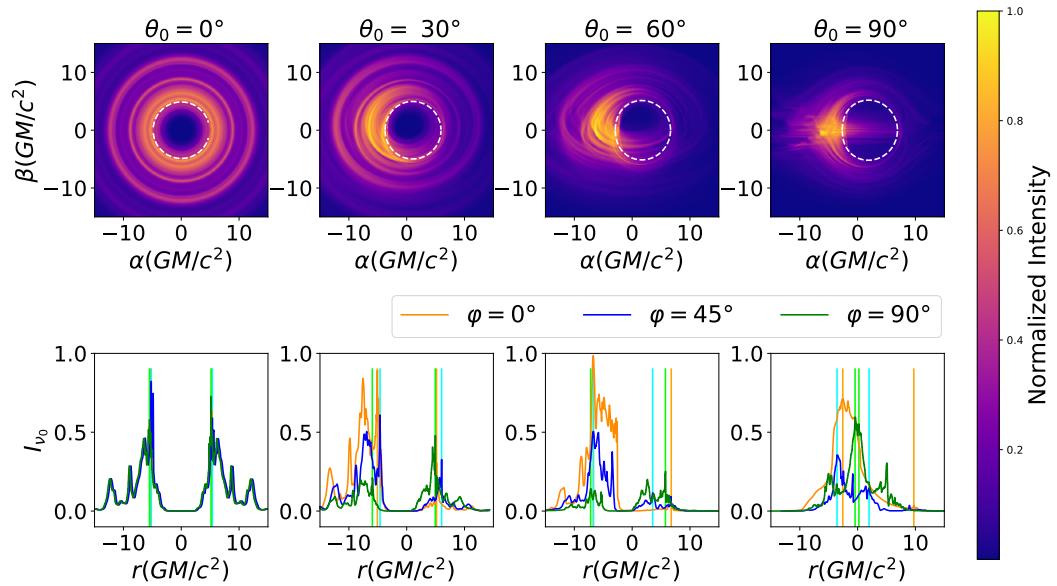


Figure 4.1.15: GRMHD simulation of a Kerr-Like black hole, which has a mass of $SgrA^*$ (with a spin of $a = 0.9375M$ and a deviation parameter $\alpha_{22} = 1$). In the upper panel, intensity maps are presented from four different viewing angles ($0, 30, 60, 90$ degrees). These maps show us how the shape of the black hole's shadow and the intensity of the disk change as we vary the viewing angle. The white line on each map represents the contour of the photon ring in a Kerr SMBH, allowing us to compare it with the shadow in this Kerr-Like metric. In the lower panel, intensity profiles corresponding to the upper images are shown. Each image has three intensity profiles taken from different angles. By observing how the height and location of the peak points change along the x-axis in these profiles, we can perform subsequent analysis of the diameter, displacement, and asymmetry of the black hole's shadow.

Now, conducting the analysis of the diameter, displacement, and asymmetry of these four figures (4.1.12 - 4.1.15), we obtain the Fig. (4.1.16).

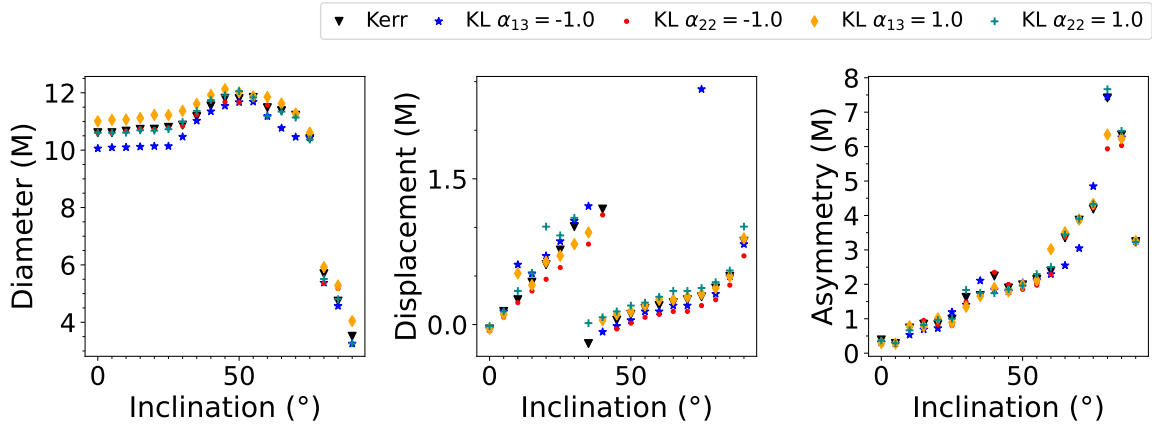


Figure 4.1.16: Comparison of the diameter, displacement, and asymmetry values for a Kerr-Like BH simulations with the mass of $SgrA^*$ and with deviation parameters $\alpha_{13} = -1$ (Blue stars), $\alpha_{22} = -1$ (Red dots), $\alpha_{13} = 1$ (Orange diamonds), $\alpha_{22} = 1$ (Dark cyan plus sign), and in the simulation of a Kerr black hole (Black triangles). This comparison highlights how these values change as the viewing angle varies from 0 to 90 degrees, revealing significant differences between the deviated values and the background value for the Kerr simulation. Furthermore, distinct differences are observed compared to the previously shown deviations for the mass of $M87^*$, particularly notable are the more abrupt and larger changes as the viewing angle increases, especially in diameter and displacement, changes expected to be caused by the structure of the disk.

We can observe that in this case, the values obtained for diameter, displacement, and asymmetry are greatly influenced by the disk. Additionally, a clear difference in the diameter values among the different deviations is noticeable. Here, we can see that the deviation with the greatest influence on the diameter value is given by the free function $A_1(r)$, while $A_2(r)$ barely changes its diameter compared to Kerr, showing a more noticeable difference at angles of view near edge-on.

On the other hand, we notice that in the case of displacement, the free function $A_2(r)$ plays a more significant role, being more prominent than $A_1(r)$ in comparison to simulations of the Kerr metric.

Finally, the asymmetry behaves similarly in all three cases: for $A_1(r)$, $A_2(r)$, and the Kerr case. The most substantial differences between these values are

found at angles close to 90° .

4.1.2 Thin-disk model simulations

As mentioned earlier, changes in the geometry of spacetime inevitably lead to alterations in the structure of the accretion disk. To address this point similarly, an analysis of ray-tracing simulations is carried out for a black hole in an environment where the disk model is semi-analytic, using the Novikov-Thorne model as a foundation and reference.

The purpose of this analysis is to observe the impact of Kerr deviations on the structure of the disk itself and on radiation transport. Additionally, it aims to confirm the accuracy of the effects observed in simulations with the HARM model.

In this model, it is possible to control more parameters of both the disk and the black hole itself, as for metrics derived from Kerr, factors such as R_{ISCO} , the Keplerian plasma velocity Ω , etc., change in conjunction with the spacetime geometry.

Consequently, simulations were conducted following the input parameters below for the thin disk model according to Tab. (4.1.3)

Parameter	Thin-disk test value
a	$0.93M$
M_{BH}	$10M_\odot$
d_{source}	0.05pc
v_{cam}	$2.41 \times 10^{17}\text{Hz}$
r_{cam}	$10^4 R_g$
Resolution for $[x, y]$	$[300, 300]\text{px}$
Range for $[\alpha, \beta]$	$[-20, 20] R_g$
\dot{M}	$1.399 \times 10^{19}\text{g/s}$
r_{out}	$1000R_g$
stepsize	0.001

Table 4.1.3: Setting inspired in the test values used in [Bronzwaer et al. \(2020\)](#)

We approach the analysis similarly to the previous cases, considering free deviations in the range $[-1.0, 1.0]$ for the images, and $[-1.0, -0.5, 0.5, 1.0]$ for quantifying the diameter, displacement, and asymmetry values. However, this

time, we only focus on the deviation parameters α_{13} and α_{22} , as previously deduced that α_{52} loses relevance in affecting radiation transport and the black hole's geometry. In the conducted tests, the R_{ISCO} for this deviation tended to coincide with the metric without deviations, and its effect on the structure and geometry of the disk and shadow was also negligible.

4.1.2.1 Deviation parameter α_{13}

Therefore, for $\alpha_{13} = -1$ and $\alpha_{13} = 1$, the simulations yield the following results given in Figs. (4.1.17-4.1.18).

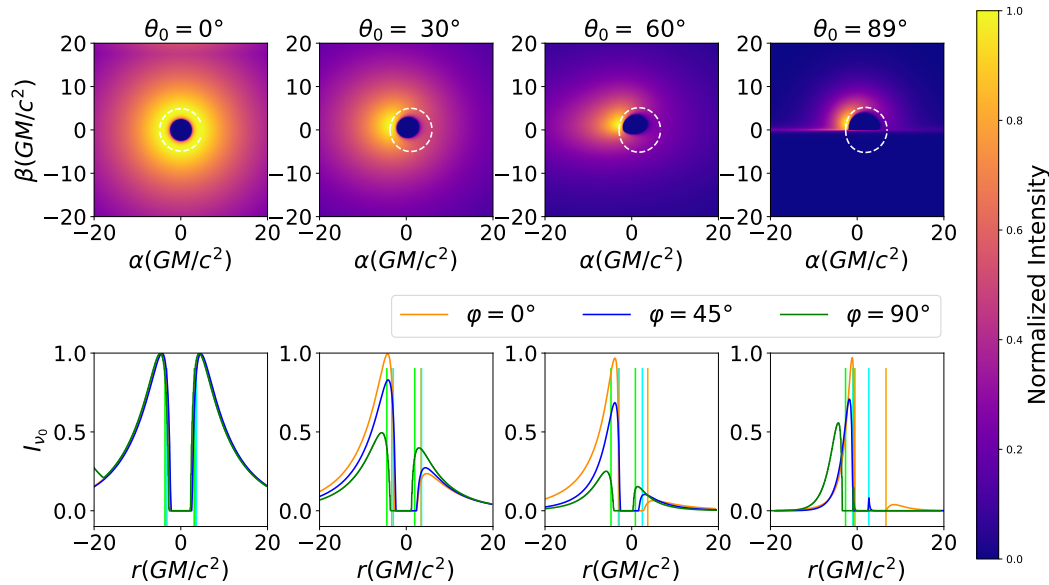


Figure 4.1.17: Thin accretion disk simulation of a Kerr-Like black hole with a mass of $10M_\odot$ (with a spin of $a = 0.93M$ and a deviation parameter $\alpha_{13} = -1$). In the upper panel, intensity maps are presented from four different viewing angles ($0, 30, 60, 89$ degrees). These maps show us how the shape of the black hole's shadow and the intensity of the disk change as we vary the viewing angle. The white line on each map represents the contour of the photon ring in a Kerr BH, allowing us to compare it with the shadow in this Kerr-Like metric. In the lower panel, intensity profiles corresponding to the upper images are shown. Each image has three intensity profiles taken from different angles. By observing how the height and location of the peak points change along the x-axis in these profiles, we can perform subsequent analysis of the diameter, displacement, and asymmetry of the black hole's shadow.

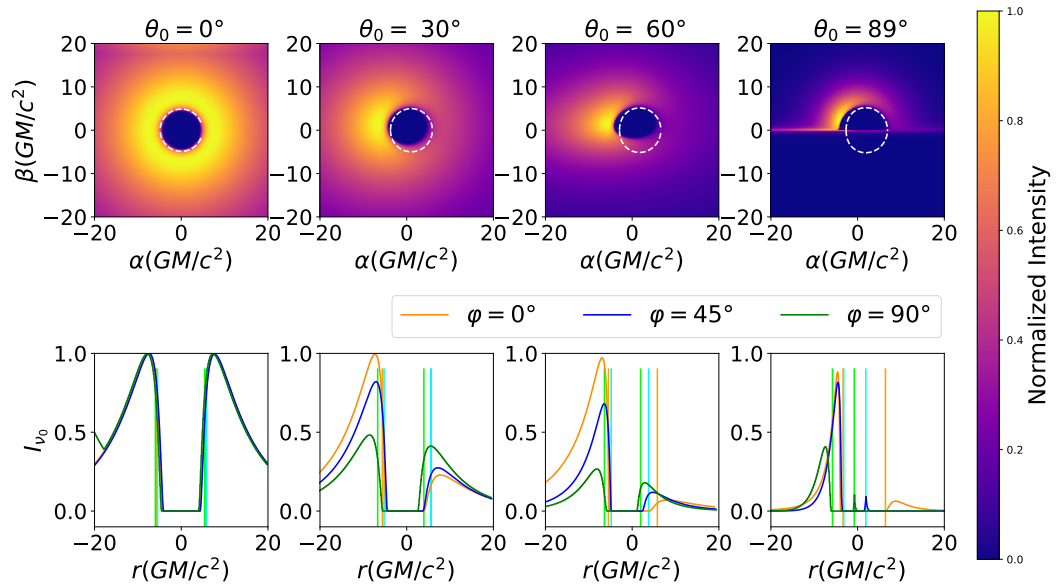


Figure 4.1.18: Thin accretion disk simulation of a Kerr-Like black hole with a mass of $10M_\odot$ (with a spin of $a = 0.93M$ and a deviation parameter $\alpha_{13} = 1$). In the upper panel, intensity maps are presented from four different viewing angles ($0, 30, 60, 89$ degrees). These maps show us how the shape of the black hole's shadow and the intensity of the disk change as we vary the viewing angle. The white line on each map represents the contour of the photon ring in a Kerr BH, allowing us to compare it with the shadow in this Kerr-Like metric. In the lower panel, intensity profiles corresponding to the upper images are shown. Each image has three intensity profiles taken from different angles. By observing how the height and location of the peak points change along the x-axis in these profiles, we can perform subsequent analysis of the diameter, displacement, and asymmetry of the black hole's shadow.

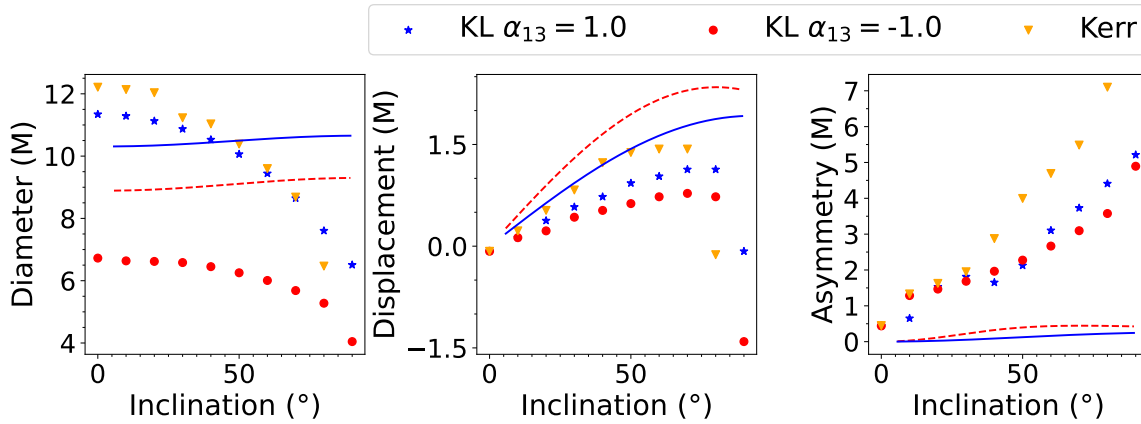


Figure 4.1.19: Comparison of the diameter, displacement, and asymmetry values for a $10M_{\odot}$ BH in a thin disk simulation between the fit calculated by Johannsen (*Blue line*) for a Kerr-Like BH with a deviation parameter $\alpha_{13} = -1$ (*Red dashed line*), $\alpha_{13} = 1$ and a Kerr-Like simulation (*Blue stars and Red dots*) of a BH with these deviation parameters, respectively, and with the Kerr BH simulation (*Orange triangles*). This illustrates how these values change as the viewing angle towards the BH changes, noticing a notable shift as we approach edge-on angles. Here, the diameter consistently decreases in comparison to the fits, and the displacement increases until decreasing abruptly near 90° , while the asymmetry always grows. These changes induced by the deviations are quite pronounced in comparison to Kerr in this model.

Something that we can notice almost immediately in the simulations of thin accretion disks, compared to the previous ones and in comparison with the photon ring calculated for the Kerr metric (*white dashed line* in the figures), is the change in the size of the shadow or its diameter depending on the deviations. In Fig. (4.1.17), we observe that the black hole’s shadow is significantly smaller in relation to its respective photon ring for the Kerr metric. One reason for this occurrence is likely that in the simulations of thin accretion disks, unlike the simulations conducted for radiative transport analysis based on HARM, the location of R_{ISCO} is taken into account as the starting point of the disk’s structure. Its value in the Kerr-Like metric differs from the Kerr metric, and it is numerically calculated based on the minima of the effective potential, or

rather in this case, based on the minimum energy

$$\frac{dE}{dr} = 0. \quad (4.1.9)$$

To verify the correctness of this simulation, it is possible to compare its image with the one calculated by (Johannsen, 2014). They conducted a study of their metric for thin disk simulations but did not compare it with the Kerr metric in the same way as we did in this study.

Furthermore, upon comparison with the fits calculated by Johannsen (Johannsen, 2013a), we observe how the shadow's diameter significantly differs from these calculations, decreasing as the angle approaches 90° . On the other hand, the displacement behaves in a contrary manner to our expectations; for the $\alpha_{13} = -1$ values, the displacement is smaller than expected compared to the fit, and also when compared to the $\alpha_{13} = 1$ deviation.

Lastly, we note that the asymmetry values are lower than those of the Kerr metric, which might appear counterintuitive, as deviations are expected to induce changes in the shadow's geometry. However, the asymmetry value is directly related to the diameter. Thus, establishing a relationship between these two values is necessary to better understand how the shadow's geometry differs from Kerr's.

4.1.2.2 Deviation parameter α_{22}

Now, with the parameters $\alpha_{22} = -1$ and $\alpha_{22} = 1$. These simulations are displayed in Figs. (4.1.20-4.1.21).

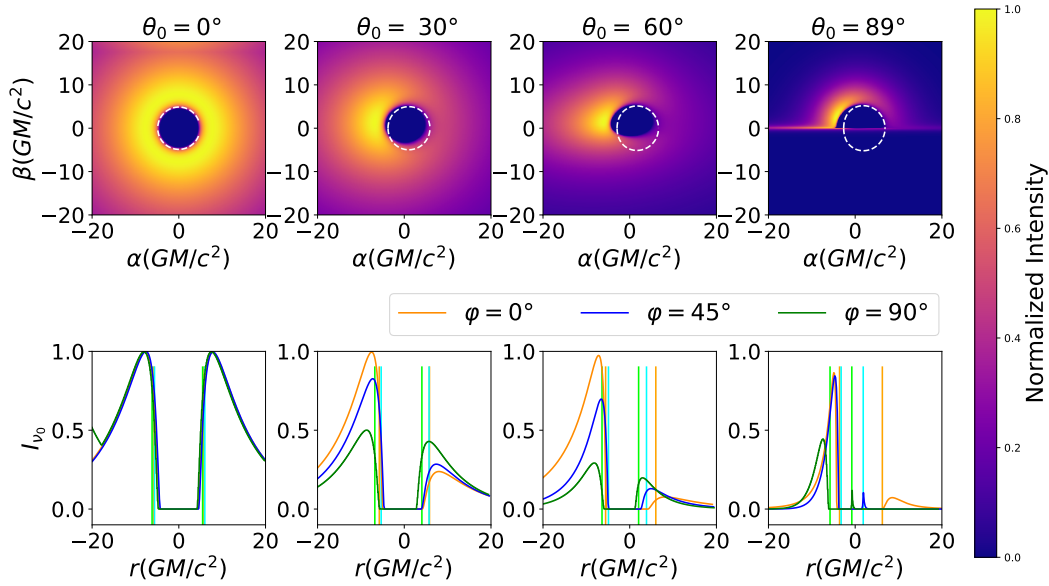


Figure 4.1.20: Thin accretion disk simulation of a Kerr-Like black hole with a mass of $10M_\odot$ (with a spin of $a = 0.93M$ and a deviation parameter $\alpha_{22} = -1$). In the upper panel, intensity maps are presented from four different viewing angles ($0, 30, 60, 89$ degrees). These maps show us how the shape of the black hole's shadow and the intensity of the disk change as we vary the viewing angle. The white line on each map represents the contour of the photon ring in a Kerr BH, allowing us to compare it with the shadow in this Kerr-Like metric. In the lower panel, intensity profiles corresponding to the upper images are shown. Each image has three intensity profiles taken from different angles. By observing how the height and location of the peak points change along the x-axis in these profiles, we can perform subsequent analysis of the diameter, displacement, and asymmetry of the black hole's shadow.

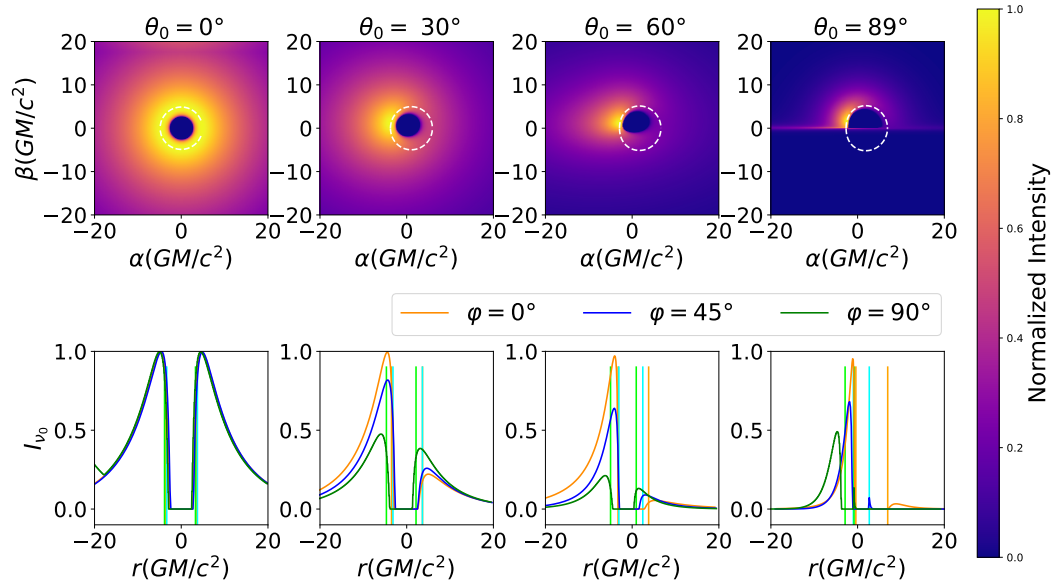


Figure 4.1.21: Thin accretion disk simulation of a Kerr-Like black hole with a mass of $10M_\odot$ (with a spin of $a = 0.93M$ and a deviation parameter $\alpha_{22} = 1$). In the upper panel, intensity maps are presented from four different viewing angles ($0, 30, 60, 89$ degrees). These maps show us how the shape of the black hole's shadow and the intensity of the disk change as we vary the viewing angle. The white line on each map represents the contour of the photon ring in a Kerr BH, allowing us to compare it with the shadow in this Kerr-Like metric. In the lower panel, intensity profiles corresponding to the upper images are shown. Each image has three intensity profiles taken from different angles. By observing how the height and location of the peak points change along the x-axis in these profiles, we can perform subsequent analysis of the diameter, displacement, and asymmetry of the black hole's shadow.

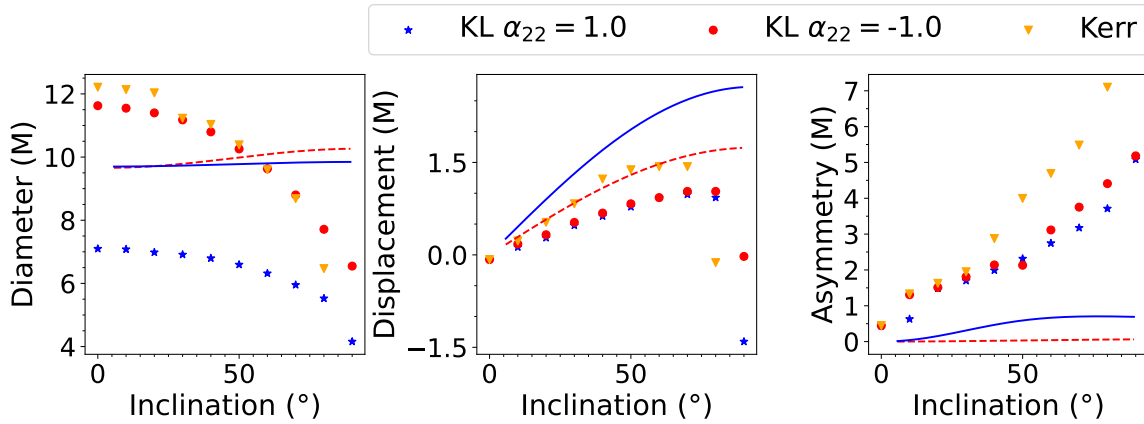


Figure 4.1.22: Comparison of the diameter, displacement, and asymmetry values for a $10M_{\odot}$ BH in a thin disk simulation between the fit calculated by Johannsen (*Blue line*) for a Kerr-Like BH with a deviation parameter $\alpha_{22} = -1$ (*Red dashed line*), $\alpha_{22} = 1$ and a Kerr-Like simulation (*Blue stars and Red dots*) of a BH with these deviation parameters, respectively, and with the Kerr BH simulation (*Orange triangles*). This illustrates how these values change as the viewing angle towards the BH changes, noticing a notable shift as we approach edge-on angles. Here, the diameter consistently decreases in comparison to the fits, and the displacement increases until decreasing abruptly near 90° , while the asymmetry always grows. These changes induced by the deviations are quite pronounced in comparison to Kerr in this model.

For the case of deviations α_{22} , we once again notice a similarity in the shadow deviations compared to α_{13} , with the difference that upon analyzing the diameter, displacement, and asymmetry parameters, we observe that for $\alpha_{22} = -1$, the shadow's diameter closely resembles the Kerr case and significantly deviates from the fits, decreasing as the angle grows. On the other hand, the diameter for $\alpha_{22} = 1$ is nearly two times smaller than for $\alpha_{22} = -1$. This stands in stark contrast to the results obtained from HARM simulations and the expectations for photon rings, where the diameter for α_{22} should change only by small amounts.

Regarding the displacement, its value differs from the fits and from Kerr, being smaller and equal between the $\alpha_{22} = -1$ and $\alpha_{22} = 1$ parameters.

Finally, the asymmetry exhibits a similar behavior to the previous cases.

And if we compare the simulations for these two deviation parameters, we have in the Fig. (4.1.23) a comparison for the diameter, displacement and asymmetry.

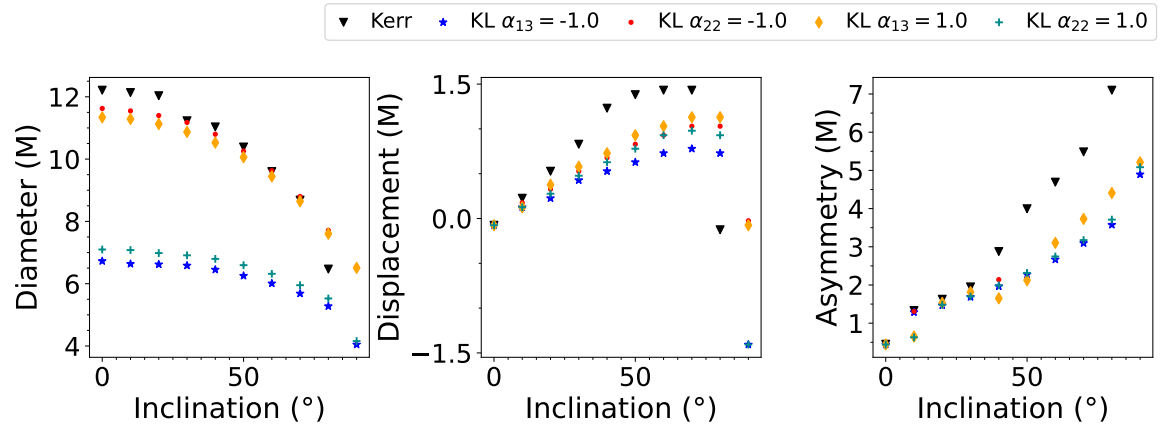


Figure 4.1.23: Comparison of how the values of diameter, displacement, and asymmetry change as the viewing angle varies from 0 to 90 degrees in simulations of thin accretion disk around a Kerr-Like BH with mass of $10M_{\odot}$ and with deviation parameters $\alpha_{13} = -1$ (Blue stars), $\alpha_{22} = -1$ (Red dots), $\alpha_{13} = 1$ (Orange diamonds), $\alpha_{22} = 1$ (Dark cyan plus sign), and in the simulation of a Kerr black hole (Black triangles). This comparison reveals significant differences between the deviated and the Kerr simulation's background values. Furthermore, it shows a significant difference compared to the simulations carried out with the HARM model. In this case, apart from the disk's effect on these values, a notable difference is observed due to the geometry altering the position of R_{ISCO} .

Now, if we analyze the deviations α_{13} and α_{22} together, we notice that they exhibit quite similar behaviors in terms of diameter for the values $\alpha_{13} = -1$ and $\alpha_{22} = 1$, as well as for $\alpha_{13} = 1$ and $\alpha_{22} = -1$. In the case of displacement, we observe that the most differing value is $\alpha_{13} = -1$, having a smaller displacement than the other deviations and significantly smaller than for the Kerr case, with all deviations being smaller than this.

Similarly, something occurs for the asymmetry, although the behavior of all deviations is similar to each other.

Finally, it's evident that for the thin disk model, the values in general differ

from the fit calculated by Johannsen, in contrast to what we obtained for the HARM case. When comparing with the Kerr metric, in the case of the thin disk, the deviations seem to have a greater influence on the shadow, causing more measurable changes compared to the HARM simulations. This might be closely related to the shift in the position of the R_{ISCO} for the Kerr-Like metric with different deviations.

Therefore, we notice that the geometry, nature, and structure of the disk play a significant role in measuring the black hole shadow and quantifying observable values. Deviations from Kerr are observable and have an impact on the structure of the disk itself and on the radiation transport around this spacetime. Johannsen's fits, while serving as a reference to highlight differences produced by the Kerr-Like metric in the shadow, could provide us with an intuitive way of understanding how they affect reality, always with the disk and its structure underlying this description.

4.1.2.3 Implications of the Kerr-Like simulations

Another fundamental feature presented by this metric is the possibility of producing a similar image to a Kerr black hole for two completely different spin parameters, which would tell us that in this case, the black hole cannot be fully described by just its mass and rotation parameter. In the following Figure (4.1.24), we can observe two thin disk simulations. The first one corresponds to a black hole with a mass of $10M_{\odot}$ and a rotation parameter $a = 0.71M$ in the Kerr spacetime. The second simulation is performed in the Kerr-Like spacetime with a deviation parameter $\alpha_{22} = -1$, a mass of $10M_{\odot}$, and a spin parameter of $a = 0.93M$.

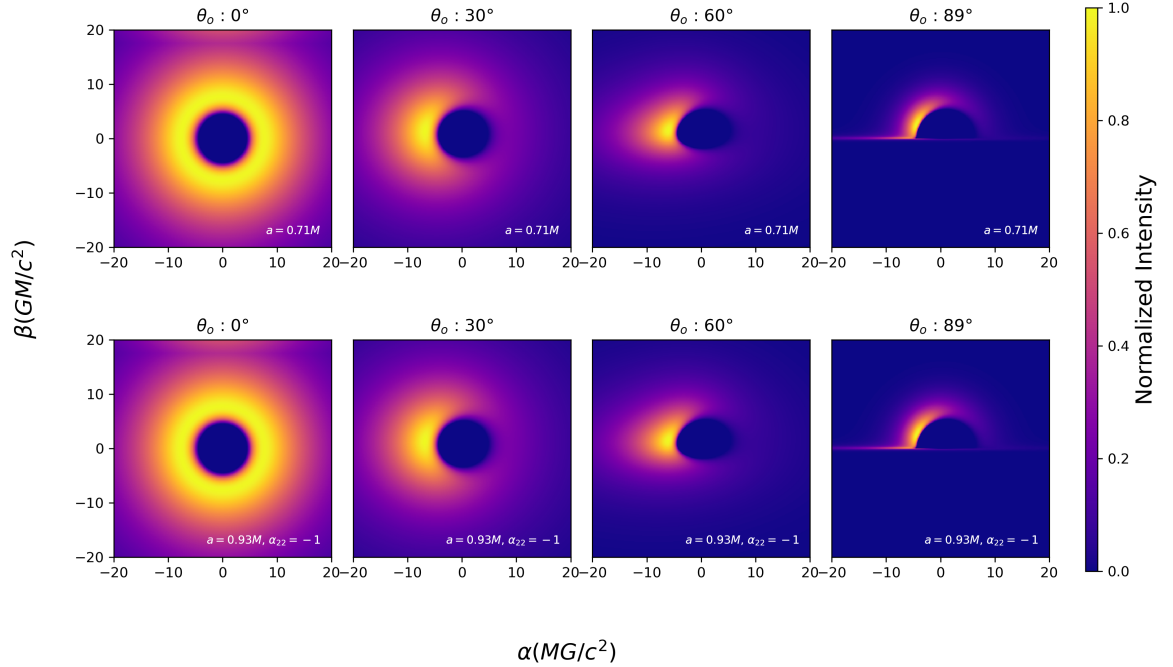


Figure 4.1.24: Comparison between two intensity maps of a thin accretion disk simulations, one for a BH in a Kerr space-time with a spin parameter $a = 0.71M$ and mass $M = 10M_{\odot}$ and the second one is for a BH in a Kerr-Like space-time with a spin parameter $a = 0.93M$ with the same mass $M = 10M_{\odot}$ and the deviation parameter of $\alpha_{22} = -1$, both for a four different angles of view, from face-on to edge-on, and the intensity values normalized and shown in the side color bar.

If we analyze the shadow using measurements of diameter, displacement, and asymmetry (see Fig. 4.1.25) for these two simulations, we observe that they are practically identical. This contradicts the description given by the theorem, as in this case, the black hole cannot be solely described by its mass and spin parameter; it also depends on the deviation parameter.

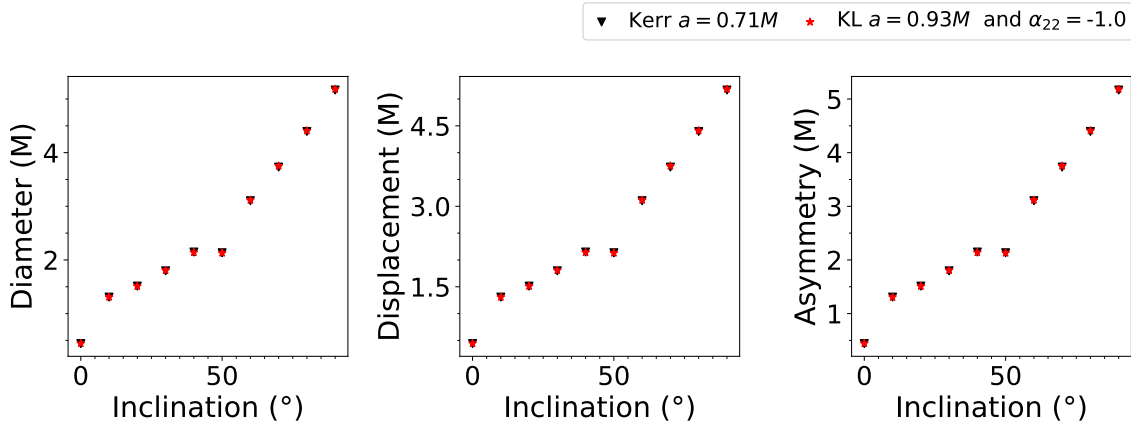


Figure 4.1.25: Comparison of diameter, displacement, and asymmetry values between a Kerr BH simulation with a spin parameter of $a = 0.71M$ (*Black triangles*) and a Kerr-Like BH simulation with a deviation parameter $\alpha_{22} = -1$ and a spin parameter of $a = 0.93M$ (*Red dots*), both with a mass of $10M_{\odot}$. This illustrates how these parameters change as the viewing angle varies from 0 to 90 degrees. It's also worth noting that there are no apparent differences between both simulations despite having different spin parameters.

4.2 Beyond Einstein gravity

While the Kerr-Like metric is a well-behaved spacetime that possesses three constants of motion, it is not a specific solution of any particular theory of gravity due to its high generality and freely adjustable deviation parameters.

Considering this, a particular focus of our study is also to understand how deviations from metrics resembling the Kerr metric in modified gravity theories can impact the images of supermassive black holes (SMBHs). In the following section, we will investigate a specific solution within the framework of the Chern-Simons modified gravity theory. We will demonstrate its derivation in Kerr-Schild coordinates following the derivation shown by (Yunes and Pretorius, 2009) in Boyer-Lindquist coordinates, as well as its effects on the photon ring for circular orbits. These effects will be explored through simulations of thin accretion disks, thereby highlighting its direct connection to the Kerr-Like metric.

Furthermore, I will present a solution for a rotating black hole obtained within

the context of the α' -corrected theory. I will discuss its separability in the Hamilton-Jacobi equations, which may potentially allow for the analytical integration of null geodesics. This has implications for the future possibility of obtaining the shadow and simulating thin accretion disks for this solution.

4.2.1 Slowly rotating Chern-Simons black hole solution

Given that for numerical simulations of black holes involving ray tracing to obtain images of them, it is more feasible to utilize the metric in Kerr-Schild coordinates, as these remain regular at the event horizon. In this section, following the derivation of the slowly rotating black hole solution conducted by (Yunes and Pretorius, 2009), which we also presented in section (2.7), we derive the same solution for Chern-Simons gravity but expressed in Kerr-Schild coordinates. The metric in these coordinates was obtained by integrating the field equations, as performing a direct coordinate transformation is not trivial.

To do this we will present the field equations again in an illustrative way

$$R_{ab} + \frac{\alpha}{\kappa} C_{ab} = \frac{1}{2\kappa} \left(T_{ab} - \frac{1}{2} g_{ab} T \right), \quad (4.2.1)$$

$$\beta \square \vartheta = \beta \frac{dV}{d\vartheta} - \frac{\alpha}{4} {}^*RR, \quad (4.2.2)$$

where C_{ab} is the C-tensor, given by

$$C^{ab} = \nu_c \epsilon^{cde(a} \nabla_e R_d^{b)} + \nu_{cd} {}^*R^{d(ab)c}, \quad (4.2.3)$$

where $\nu_a = \nabla_a \vartheta$, $\nu_{ab} = \nabla_a \nabla_b \vartheta$, and R_{ab} is the Ricci tensor, and $\square = \nabla_a \nabla^a$ is the D'Alembert operator.

4.2.1.1 Kerr-Schild form

To obtain the solution in Kerr-Schild form first using the perturbative approach, of the form

$$g_{ab} = g_{ab}^{(0)} + \zeta g_{ab}^{(1)}(\vartheta) + \zeta^2 g_{ab}^{(2)}(\vartheta), \quad (4.2.4)$$

where

$$g_{ab}^{(0)} = \eta_{ab}^{(0,0)} + ah_{ab}^{(1,0)} + a^2h_{ab}^{(2,0)}, \quad (4.2.5)$$

$$\zeta g_{ab}^{(1)} = \zeta h_{ab}^{(0,1)} + \zeta ah_{ab}^{(1,1)} + \zeta a^2h_{ab}^{(2,1)}, \quad (4.2.6)$$

$$\zeta^2 g_{ab}^{(2)} = \zeta^2 h_{ab}^{(0,2)} + \zeta^2 ah_{ab}^{(1,2)} + \zeta^2 a^2h_{ab}^{(2,2)}, \quad (4.2.7)$$

defining the space-time based on the line element

$$ds^2 = g_{\mu\nu} dx^\mu dx^\nu, \quad (4.2.8)$$

we start with the following ansatz to write the metric

$$ds^2 = - \left(1 - \frac{2M}{r}\right) (1 + h(r, \theta)) dt^2 + 2 \left(\frac{2M}{r}\right) (1 + m(r, \theta)) dt dr \quad (4.2.9)$$

$$+ 2k(r, \theta) dt d\phi + \left(\frac{2M}{r} + 1\right) (1 + l(r, \theta)) dr^2 \quad (4.2.10)$$

$$+ 2 \left(\sin(\theta)^2 n(r, \theta)\right) dr d\phi + r^2 (1 + s(r, \theta)) d\theta^2 \quad (4.2.11)$$

$$+ r^2 \sin(\theta)^2 (1 + w(r, \theta)) d\phi^2, \quad (4.2.12)$$

in terms of the free functions

$$h(r, \theta) = ah^{(1,0)} + a\zeta h^{(1,1)} + a^2h^{(2,0)}, \quad (4.2.13)$$

$$m(r, \theta) = am^{(1,0)} + a\zeta m^{(1,1)} + a^2m^{(2,0)}, \quad (4.2.14)$$

$$k(r, \theta) = ak^{(1,0)} + a\zeta k^{(1,1)} + a^2k^{(2,0)}, \quad (4.2.15)$$

$$l(r, \theta) = al^{(1,0)} + a\zeta l^{(1,1)} + a^2l^{(2,0)}, \quad (4.2.16)$$

$$n(r, \theta) = an^{(1,0)} + a\zeta n^{(1,1)} + a^2n^{(2,0)}, \quad (4.2.17)$$

$$s(r, \theta) = as^{(1,0)} + a\zeta s^{(1,1)} + a^2s^{(2,0)}, \quad (4.2.18)$$

$$w(r, \theta) = aw^{(1,0)} + a\zeta w^{(1,1)} + a^2w^{(2,0)}, \quad (4.2.19)$$

here

$$h^{(1,0)}(r, \theta) = m^{(1,0)}(r, \theta) = l^{(1,0)}(r, \theta) = s^{(1,0)}(r, \theta) = w^{(1,0)}(r, \theta) = 0, \quad (4.2.20)$$

$$k^{(2,0)}(r, \theta) = n^{(2,0)}(r, \theta) = 0, \quad (4.2.21)$$

$$n^{(1,0)}(r, \theta) = -\frac{(2M+r)a}{r}, \quad (4.2.22)$$

$$k^{(1,0)}(r, \theta) = -\frac{2M(\sin^2(\theta))a}{r}, \quad (4.2.23)$$

$$h^{(2,0)}(r, \theta) = -\frac{2(\cos^2(\theta))Ma^2}{r^2(2M-r)}, \quad (4.2.24)$$

$$m^{(2,0)}(r, \theta) = -\frac{(\cos^2(\theta))a^2}{r^2}, \quad (4.2.25)$$

$$s^{(2,0)}(r, \theta) = \frac{(\cos^2(\theta))a^2}{r^2}, \quad (4.2.26)$$

$$l^{(2,0)}(r, \theta) = -\frac{2(\cos^2(\theta))Ma^2}{r^2(2M+r)}, \quad (4.2.27)$$

$$w^{(2,0)}(r, \theta) = -\frac{(2(\cos^2(\theta))M - 2M - r)a^2}{r^3}. \quad (4.2.28)$$

By introducing these values into the field equations, the following functions are obtained as solutions

$$\psi^{(1,0)}(r, \theta) = \frac{\alpha(18M^2 + 10Mr + 5r^2)}{8r^4\beta M} \cos \theta, \quad (4.2.29)$$

$$k^{(1,1)}(r, \theta) = C_6 r^2 (\sin^2(\theta)) + \frac{\alpha^2(189M^2 + 120Mr + 70r^2)(\sin^2(\theta))}{112K\beta r^6 \zeta}, \quad (4.2.30)$$

$$n^{(1,1)}(r, \theta) = N_1(r), \quad (4.2.31)$$

$$m^{(1,1)}(r, \theta) = \frac{G_2(\theta)r^2 + 2G_1(r)M - G_1(r)r}{2M - r}. \quad (4.2.32)$$

$$(4.2.33)$$

Where, without loss of generality $\psi^{(1,1)}(r, \theta) = \psi^{(2,0)}(r, \theta) = 0$, $h^{(1,1)}(r, \theta) = B \cdot m^{(1,1)}(r, \theta)$, $w^{(1,1)}(r, \theta) = s^{(1,1)}(r, \theta) = 0$ and $l^{(1,1)}(r, \theta) = L_1(r)$, also we can

assume the following values for the free functions

$$G_1(r) = \frac{4M^2 A_1(r) - A_1(r) r^2 + M_1 r^2}{8M^2}, \quad (4.2.34)$$

$$A_1(r) = \frac{\hat{M}_1 r^2}{(2M - r)(2M + r)}, \quad (4.2.35)$$

$$L_1(r) = \frac{C_1 r^2}{(2M - r)(2M + r)}. \quad (4.2.36)$$

$$(4.2.37)$$

Here we select $C_6 = B = M_1 = \hat{M}_1 = C_1 = 0$, $G_2(\theta) = 0$ and

$$N_1(r) = \frac{\alpha^2 (189M^2 + 120Mr + 70r^2) (\sin^2(\theta))}{112K\beta r^6}. \quad (4.2.38)$$

Then the slowly rotating Chern-Simons solution in Kerr-Schild coordinates is

$$g_{tt} = - \left(-1 + \frac{2M}{r} - \frac{2M \cos^2 \theta a^2}{r^3} \right), \quad (4.2.39)$$

$$g_{tr} = \frac{2M}{r} - \frac{2M \cos^2 \theta a^2}{r^3}, \quad (4.2.40)$$

$$g_{t\phi} = -\frac{2M \sin^2 \theta a}{r} + \frac{a\alpha^2 (189M^2 + 120Mr + 70r^2) \sin^2 \theta}{112K\beta r^6}, \quad (4.2.41)$$

$$g_{rr} = 1 + \frac{2M}{r} - \frac{2M \cos^2 \theta a^2}{r^3}, \quad (4.2.42)$$

$$g_{r\phi} = -a \sin^2 \theta - \frac{2M \sin^2 \theta a}{r} + \frac{a\alpha^2 (189M^2 + 120Mr + 70r^2) \sin^2 \theta}{112K\beta r^6}, \quad (4.2.43)$$

$$g_{\theta\theta} = r^2 + a^2 \cos^2 \theta, \quad (4.2.44)$$

$$g_{\phi\phi} = \frac{(-2a^2 \cos^2 \theta + (r + 2) a^2 + r^3) \sin^2 \theta}{r}. \quad (4.2.45)$$

4.2.1.2 Relation with the Kerr-Like metric

On the other hand, in (Johannsen, 2013b), it is proposed that the solution of a slowly rotating black hole in Chern-Simons gravity can be mapped to the Kerr-Like metric using the following expressions:

$$\alpha_{24} = \frac{5}{8}\zeta_{CS}, \quad (4.2.46)$$

$$\alpha_{25} = \frac{15}{14}\zeta_{CS}, \quad (4.2.47)$$

$$\alpha_{26} = \frac{27}{16}\zeta_{CS}. \quad (4.2.48)$$

This is carried out for Boyer-Lindquist coordinates, where

$$g_{t\phi} = g_{t\phi}^{\text{SLK}} + \frac{5}{8}\zeta_{CS} \frac{a}{M} \frac{M^5}{r^4} \left(1 + \frac{12M}{7r} + \frac{27M^2}{10r^2} \right) \sin^2 \theta, \quad (4.2.49)$$

where $\zeta_{CS} = \frac{\alpha^2}{\kappa\beta M^4}$ and $g_{t\phi}^{\text{SLK}}$ is the (t, ϕ) component of the slowly rotating Kerr metric.

It is straightforward to demonstrate that this mapping works equally well for the metric in Kerr-Schild coordinates that we obtained. The new contribution that arises in the metric due to the mapping is in the (r, ϕ) component, therefore

$$g_{r\phi} = g_{r\phi}^{\text{SLK}} + \frac{5}{8}\zeta_{CS} \frac{a}{M} \frac{M^5}{r^4} \left(1 + \frac{12M}{7r} + \frac{27M^2}{10r^2} \right) \sin^2 \theta, \quad (4.2.50)$$

and all others deviation parameters vanish.

4.2.1.3 Thin-disk simulations and analysis

The fact that the obtained metric is of the slowly rotating type implies that this metric is restricted to spin with a small parameter, as we work within a perturbative framework where the rotation parameter is limited up to order 2, discarding terms of $\mathcal{O}(a^3)$ and higher. On the other hand, it is not clear what the upper limit is for this rotation parameter. (Ayzenberg et al., 2016) studied the Kerr metric within this scheme and attempted to establish an upper limit based on its behavior in electromagnetic observations of black holes, concluding that it should be $a < 0.6M$. In this part of the section, we attempt to find an upper limit for the spin parameter value from first principles, i.e., through geometric scalars, considering the Kerr metric for this calculation.¹ If we calculate the Kretschmann scalar for this metric, we find that

¹This makes sense as we use it as a background metric when performing the perturbative calculation of solutions in modified gravity theories.

$$K = - \frac{48M^2 (a^6 \cos^6 \theta - 15 \cos^4 \theta a^4 r^2 + 15 \cos^2 \theta a^2 r^4 - r^6)}{(r^2 + a^2 \cos^2 \theta)^6}, \quad (4.2.51)$$

where, if we do a expansion around a , then

$$K \approx \frac{48M^2}{(M + \sqrt{M^2 - a^2})^6} - \frac{1008M^2 \cos^2 \theta a^2}{(M + \sqrt{M^2 - a^2})^8} + \mathcal{O}(a^3), \quad (4.2.52)$$

here, if we require that the first term of the expansion be strictly smaller than the second term, we obtain that

$$a < 0.416M, \quad (4.2.53)$$

a value that allows us to establish the framework for analyzing the shadow in this theory.

We will begin by studying the behavior of the photon ring, just as we did for the Kerr-Like metric. Given that both metrics are compatible and it is possible to map the Chern-Simons metric to the Kerr-Like metric, we can use the expressions (4.1.1 - 4.1.3) previously used with the given mapping for the function $A_2(r)$ given by the equations (4.2.46). Therefore, the photon rings in this metric compared to the usual Kerr metric appear as follows:

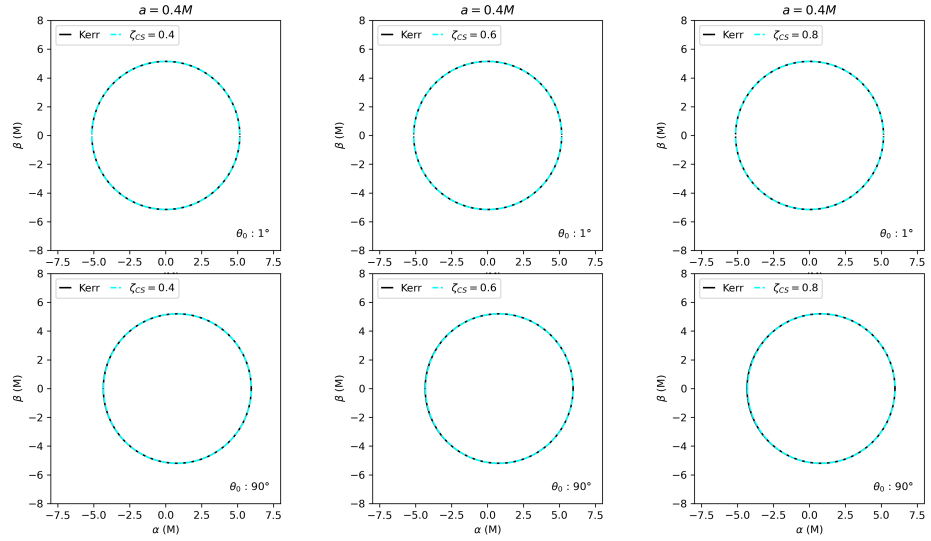


Figure 4.2.1: Comparison between photon rings for Kerr black hole (*black line*) and for a Slowly rotating Chern-Simons black hole (*cyan line*) with a spin parameter $a = 0.4M$ (to work well in the slowly rotating limit) and with a coupling values of $\zeta_{CS} = [0.4, 0.6, 0.8]$. The upper panel of the figure shows an angle of view face-on (i.e 1°) and the lower panel of the figure shows an edge-on angle of view (i.e 90°). This shows that initially there is no difference between the photon rings for these two viewing angles and the different coupling parameters for the theory.

One thing that can be directly concluded from the images of the photon rings is that it is not possible to observe a significant difference compared to the Kerr metric. Even if we approach the coupling value close to its maximum, it does not exhibit a substantial deviation of the shadow as the Kerr-Like metric does. This is likely due to the fact that the deviation in the Kerr metric occurs for terms that scale as r^{-4} or higher powers, which indicates that since the deviation value is in the numerator and also small, the deviations will be insignificant at that order.

However, while this applies to the photon rings, which are defined by solving null geodesics for circular orbits, it is not immediately clear if the same happens for non-circular orbits and for physical situations where the luminosity source around the black hole is more realistic, as in an accretion disk, for example. At this point, it is beneficial to use ray-tracing simulations to observe the black hole shadow in a more realistic approach. Therefore, we proceed to employ

thin accretion disk simulations based on the Novikov-Thorne model, as done previously, for coupling values $\zeta_{CS} = [0., 0.4, 0.6, 0.8]$. Subsequently, we will analyze the diameter, displacement, and asymmetry values to quantify the shadow and compare with simulations conducted for the Kerr metric. The inputs used in RAPTOR are summarized in Table (4.2.1).

Parameter	Thin-disk test value
a	$0.4M$
M_{BH}	$10M_{\odot}$
d_{source}	0.05pc
ν_{cam}	$2.41 \times 10^{17}\text{Hz}$
r_{cam}	$10^4 R_g$
Resolution for $[x, y]$	$[300, 300]\text{px}$
Range for $[\alpha, \beta]$	$[-20, 20] R_g$
\dot{M}	$1.399 \times 10^{19}\text{g/s}$
r_{out}	$1000R_g$
stepsize	0.001

Table 4.2.1: Settings based on previously for a thin accretion disk but with a spin parameter $a = 0.4M$ to works well in the slowly rotating limit.

Then the thin accretion disk simulations for a slowly rotating Chern-Simons black hole solution with different values of the coupling parameter are displayed in Fig. (4.2.2).

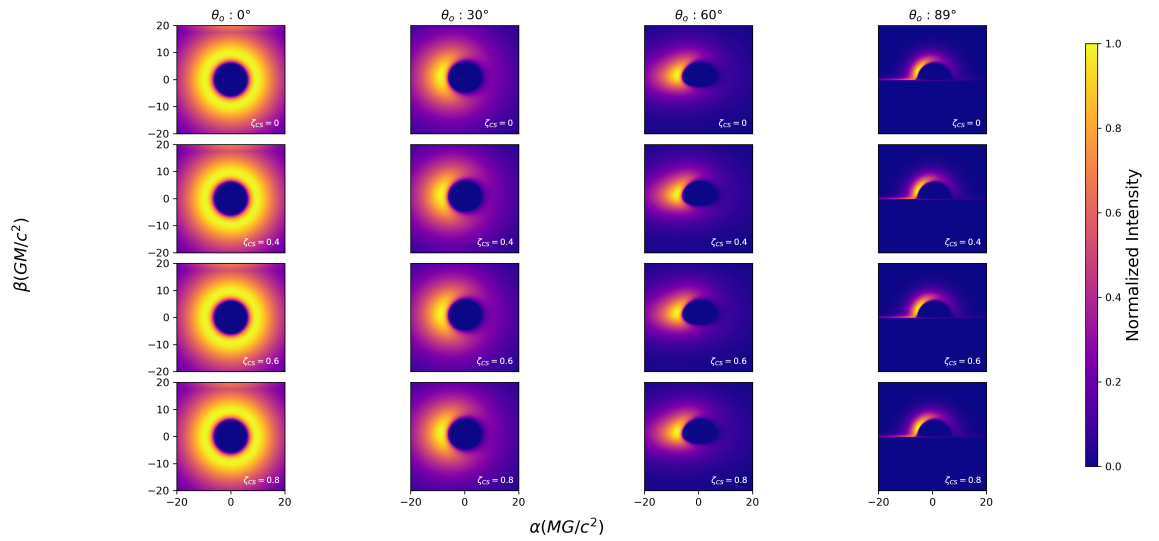


Figure 4.2.2: Comparison of intensity maps in thin-disk simulations within the slowly rotating Chern-Simons black hole solution. This is conducted for a black hole with a mass of $10M_{\odot}$ and coupling values of $\zeta_{CS} = [0., 0.4, 0.6, 0.8]$, a spin parameter of $a = 0.4M$, and viewing angles of $\theta_0 = [0, 30, 60, 89]^{\circ}$. The normalized intensity is represented in the side color bar.

From these simulations, if we compare their diameter, displacement, and asymmetry values, we obtain the figure (4.2.3).

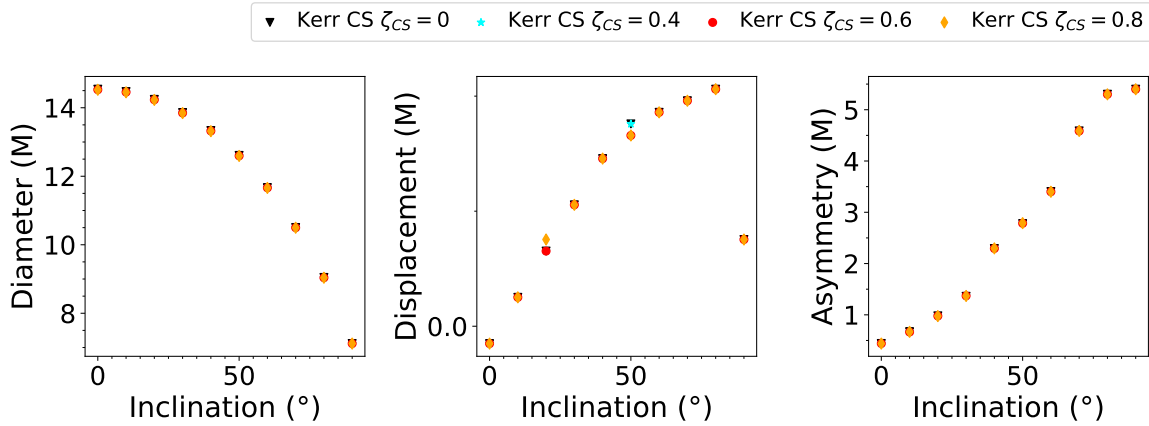


Figure 4.2.3: Comparison between diameter, displacement and asymmetry taking for a different inclinations angles from the simulations of a Kerr black hole and for a Chern-Simons Slowly rotating solution with a coupling values of $\zeta_{CS} = [0.4, 0.6, 0.8]$. Here it is shown how these parameters change as the viewing angle varies from 0 to 90 degrees. This reveals that there is no apparent change in these values for the different coupling values, namely 0.4 (Cyan stars), 0.6 (Red dots), and 0.8 (Yellow diamonds).

Here in the figure 4.2.3, we note that there is almost no observable difference between the three simulations for the rotating black hole solution in the Chern-Simons theory and the Kerr solution of General Relativity, except for a slight difference in the displacement value at an observation angle of 50° where we notice that the shadow displacement is slightly smaller for coupling values of $\zeta_{CS} = 0.6$ and $\zeta_{CS} = 0.8$. However, this difference occurs only at this specific angle, so we could deduce that it might be a measurement error from the algorithm or a potential area to explore possible deviations, a task that will require further investigation in the future.

Another thing to consider when conducting the analysis of the black hole shadow for this particular metric is that the value of $\zeta_{CS} \ll 1$ (Ayzenberg and Yunes, 2018) for the Chern-Simons modified gravity theory to be effective.. However, when studying this limit and attempting to determine a value through the use of observational data, it significantly deviates from the effective theory limit. Thus, taking into account the upper limit defined by (Yunes and Pretorius, 2009), for which

$$\zeta^{1/4} \approx 10^4 \text{ km}, \quad (4.2.54)$$

where, by studying the variation of the orbital elements of a binary system averaged over a period, (Yunes and Pretorius, 2009) derived the equation

$$\zeta \leq \frac{64}{25} M r_{sm}^3 \delta, \quad (4.2.55)$$

which was used with the data derived from observations of PSR J0737-3039 A/B (Burgay et al., 2003) to establish the upper limit as previously shown. Where the mass used was $M = 1.476M_{\odot}$, $r_{ms} = 4.2410^5 \text{ km}$.

If we calculate this bound in the dimensionless form of the coupling parameter, we obtain

$$\zeta_{CS} = 4.51 \times 10^{14}, \quad (4.2.56)$$

for the same mass $M = 1.476M_{\odot}$. This is completely beyond the upper limit for the theory to be effective.

This leads us to the question of how far we can explore the value of this parameter. To address this, an analysis was conducted on the values of diameter, displacement, and asymmetry of the photon rings to understand at what point the deviations become significant. Looking at Fig. (4.2.4), it's noticeable that when the spin is close to the maximum for this metric (i.e. $a = 0.4M$), the deviation becomes substantial for values of $\zeta_{cs} \geq 1$. When we visualize these as photon rings (4.2.5), we observe that significant differences compared to Kerr exist for these values. This could motivate the exploration of other theories that don't have such restrictions or where the coupling can be much more flexible. However, in the realistic scenario, the conclusion remains that the differences are minimal compared to the results obtained from General Relativity. At least in measurements of the environment around black holes, these deviations are not visible, especially considering the current resolution of the EHT.

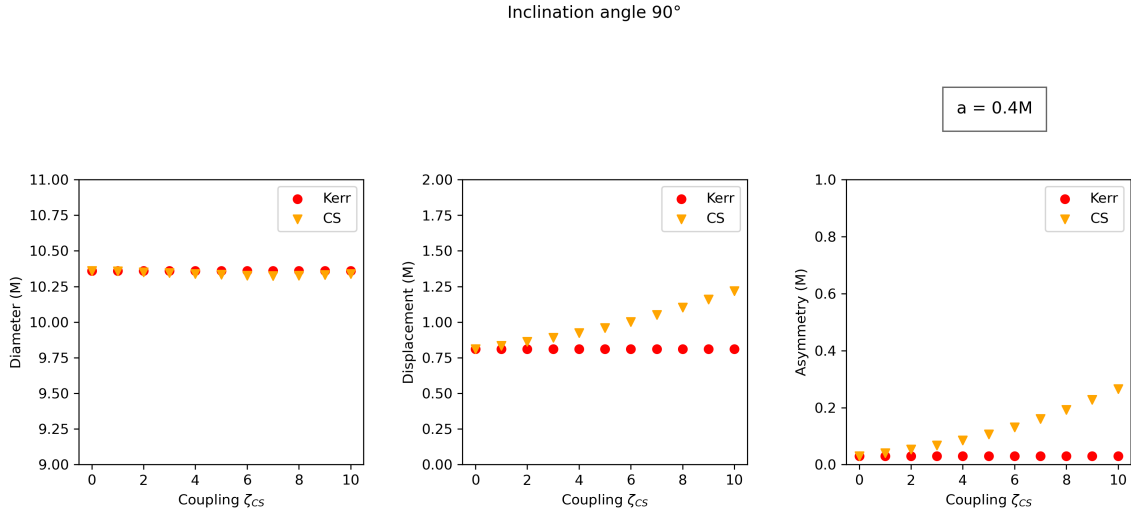


Figure 4.2.4: Comparison of diameter, displacement, and asymmetry calculated by the photon rings for different values of the coupling term $\zeta_{CS} = [0, 10]$ with a constant angle of view of 90° . In this scenario, it should be possible to observe more significant changes compared to the Kerr metric, where these parameters remain constant, along with a spin parameter of $a = 0.4M$. We notice that as the coupling term exceeds 1, changes in the diameter, displacement, and asymmetry parameters in the photon ring start to appear, in the hypothetical case where $\zeta_{CS} > 1$.

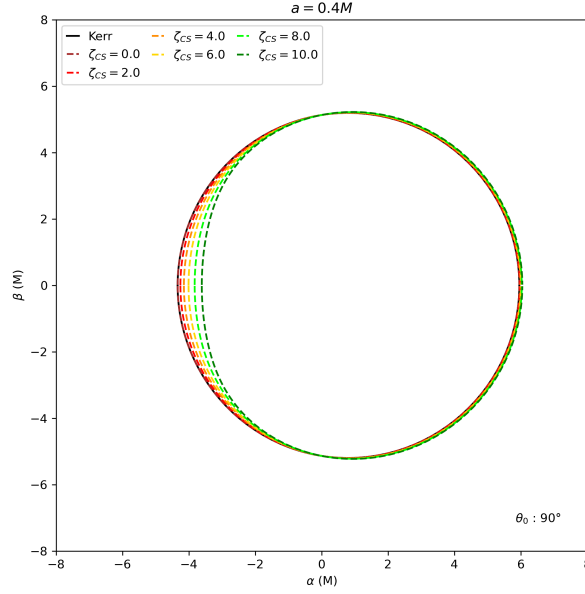


Figure 4.2.5: Comparison of the photon rings for a different values of $\zeta_{CS} \geq 1$ and the Kerr metric photon ring both with a 90° angle of view and spin parameter $a = 0.4M$. Here, a noticeable difference in the shape of the ring is observed on the left side, where there is a flattening towards the center as the coupling value ζ_{CS} increases.

4.2.2 Slowly rotating α' -corrected black hole solution

We are interested to study the shadow of a rotating black hole, then it is natural to study deformations of the Kerr metric due to the higher curvature and the scalar field. In this approach there are two perturbative parameters, namely three relevant parameters, namely the mass of the black hole M the rotation parameter a which must be compared with the perturbative parameter α of the theory. The most general solution in this form is in the following form

$$g_{\mu\nu} = g_{\mu\nu}^{\text{Kerr}}(M, a) + \alpha g_{\mu\nu}^{(1)}(M, a) . \quad (4.2.57)$$

However, it is not clear that such a solution can be integrated analytically. It was obtained in (Agurto-Sepúlveda et al., 2023) a slowly rotating version of

(4.2.57) where expansion of the metric is of the form

$$g_{\mu\nu} = g_{\mu\nu}^{[0,0]} + \alpha g_{\mu\nu}^{[1,0]} + a g_{\mu\nu}^{[0,1]} + \alpha a g_{\mu\nu}^{[1,1]} + a^2 g_{\mu\nu}^{[0,2]} + \mathcal{O}(a^3, \alpha a^2, \alpha^2) \quad (4.2.58)$$

$$\phi = \phi_0 + \alpha \phi_1(r) + \mathcal{O}(a^3, \alpha a^2, \alpha^2) ,$$

where terms of the form αa^2 was neglected, note that the system of equations is consistent with considering corrections of the type αa not a^2 in the scalar field.

4.2.2.1 Kerr-Schild form

As mentioned earlier, black hole simulations are better suited to Kerr-Schild coordinates. Therefore, we will adapt the solution found in (Agurto-Sepúlveda et al., 2023) to obtain the metric in Kerr-Schild coordinates which are regular at the black hole horizon. The components of the solution are given by ²

$$g_{tt} = -1 + \frac{2M}{r} - \alpha f_1(r) - a^2 \frac{2 \cos^2 \theta M}{r^3} , \quad (4.2.59)$$

$$g_{tr} = \frac{2M}{r} + \alpha X(r) - a^2 \frac{2M}{r^3} , \quad (4.2.60)$$

$$g_{t\varphi} = a \frac{2M \sin^2 \theta}{r} + \alpha h_{t\varphi}(r, \theta) , \quad (4.2.61)$$

$$g_{rr} = 1 + \frac{2M}{r} + \alpha g_1(r) + a^2 \frac{2(M + \frac{r}{2}) \cos^2 \theta - 4M - r}{r^3} , \quad (4.2.62)$$

$$g_{r\varphi} = \frac{2aM}{r} \sin^2 \theta , \quad (4.2.63)$$

$$g_{\theta\theta} = r^2 + a^2 \cos^2 \theta , \quad (4.2.64)$$

$$g_{\varphi\varphi} = r^2 \sin^2 \theta - a^2 \frac{\sin^2 \theta (2M \cos^2 \theta - 2M - r)}{r} ,$$

the function $X(r)$ is a "pure gauge function" and consequently arbitrary so we can set this $X(r) = 0$, The functions at order α are given by where we turned

²We use the notation $G = c = 1$

off each integration constant

$$f_1(r) = \frac{4}{r^2} + \frac{10M}{3r^3} + \frac{8M^2}{r^4}, \quad (4.2.65)$$

$$g_1(r) = 2 \frac{(24M^4 + 22M^3r + 33M^2r^2 + 15Mr^3 + 6r^4)}{[3(2M - r)Mr^4]}, \quad (4.2.66)$$

$$h_{t\varphi}(r, \theta) = -\sin^2\theta \left(\frac{8M^2}{r^4} + \frac{6M}{r^3} - \frac{6}{r^2} \right) \quad (4.2.67)$$

$$\phi_1(r) = -\frac{1}{Mr} - \frac{1}{r^2} - \frac{4M}{3r^3}. \quad (4.2.68)$$

Finally, the set of these equations (4.2.59 - 4.2.68) results in the Kerr-Schild coordinates version of the slowly rotating black hole solution obtained in (Agurto-Sepúlveda et al., 2023).

4.2.2.2 Separability of Hamilton-Jacobi equations and implications

A first step in obtaining the shape of a black hole's shadow is to consider the null geodesic problem, which can be solved by integrating the geodesic equations for photons. However, solving the geodesic equations in modified gravity theories is not straightforward, just as it is not for the solutions in general. To tackle this problem, two approaches can be taken. One approach entails using numerical methods to integrate the geodesic equations, thereby obtaining the shape of the photon rings (representing the shadow's shape in theoretical terms) for the black hole. The other approach depends on whether the spacetime possesses sufficient constants of motion to allow for an analytical solution.

Here we tried this second way, by defining space-time as

$$ds^2 = g_{\mu\nu} dx^\mu dx^\nu, \quad (4.2.69)$$

where the components are

$$\begin{aligned}
g_{tt} &= -\frac{2M \cos^2 \theta a^2 + 2r^2 M - r^3}{r^3} - \frac{2}{3Mr^4} \left(12M^3 + 5M^2 r + 6r^2 M - 6r^3 \right) \alpha , \\
g_{rr} &= \frac{-a^2 (2M - r) \cos^2 \theta - 2r^2 M - a^2 r + r^3}{r (2M - r)^2} + \frac{40M^2 - 6Mr - 6r^2}{3(2M - r)^2 r^2} \alpha , \\
g_{\theta\theta} &= r^2 + a^2 \cos^2 \theta , \\
g_{\varphi\varphi} &= \frac{\sin^2 \theta}{r} \left(2a^2 M \sin^2 \theta + a^2 r + r^3 \right) , \\
g_{t\varphi} &= -\frac{2aM \sin^2 \theta}{r} + \frac{a \sin^2 \theta}{r^4} \left(8M^2 + 6Mr + 6r^2 \right) \alpha .
\end{aligned}$$

This is the α' -corrected slowly rotating Kerr up to $\mathcal{O}(\alpha a^2)$. This is written in the notation and form of (Agurto-Sepúlveda et al., 2023).

As we mentioned earlier in (Agurto-Sepúlveda et al., 2023), we have derived E and L for this solution, representing the energy and angular momentum, respectively. However, having only two constants is insufficient to solve the geodesic equations. Drawing inspiration from a reference (Amarilla et al., 2010), we proceed to investigate the separability of the Hamilton-Jacobi equation in order to obtain a tool to solve the null geodesics equations, namely

$$\frac{\partial S}{\partial \lambda} = \frac{1}{2} g^{\mu\nu} \frac{\partial S}{\partial x^\mu} \frac{\partial S}{\partial x^\nu} , \quad (4.2.70)$$

where S is the Jacobi action. The components of $g^{\mu\nu}$ are calculated up to order $\mathcal{O}(\alpha a)$. Then if the problem is separable, the Jacobi action S can be written in the form

$$S = \frac{1}{2} \delta \lambda - Et + L\varphi + S_r + S_\theta , \quad (4.2.71)$$

where E is the energy, L is the angular momentum, S_r is a function only depends on the r coordinate and S_θ is only a function of θ . We are interested only in null geodesics, therefore we consider $\delta = 0$. In that case the equations reduced to

$$g^{tt} E^2 - 2g^{t\varphi} EL + g^{\varphi\varphi} L^2 + g^{rr} \left(\frac{dS_r}{dr} \right)^2 + g^{\theta\theta} \left(\frac{dS_\theta}{d\theta} \right)^2 = 0 . \quad (4.2.72)$$

Replacing the contravariant for of the metric here, this equation can be written

like

$$\begin{aligned} & \left(\Delta_{(0)} + \alpha \Delta_{(1)} \right) \frac{1}{E^2} \left(\frac{dS_r}{dr} \right)^2 + \frac{1}{E^2} \left(\frac{dS_\theta}{d\theta} \right)^2 + a^2 \left(-\cos^2 \theta + \frac{L^2 (2M - r) + 4rE^2 M^2}{E^2 r (2M - r)^2} \right) \\ & + \frac{1}{E} \frac{4LMa}{r - 2M} - \frac{r^3}{r - 2M} + \frac{1}{E^2} \frac{L^2}{\sin^2 \theta} \\ & + \alpha \left[\frac{2(12M^3 + 5M^2 r + 6Mr^2 - 6r^3)}{3M(r - 2M)^2} - \frac{1}{E} \frac{4a(4M^2 + 3Mr - 3r^2)L}{3(2M - r)^2 r^2} \right] = 0, \end{aligned} \quad (4.2.73)$$

where

$$\Delta_{(0)} \equiv r^2 - 2Mr + a^2, \quad (4.2.74)$$

$$\Delta_{(1)} \equiv 2 + \frac{2M}{r} - \frac{40M^2}{3r^2}. \quad (4.2.75)$$

Here we observe that the Hamilton-Jacobi equation separates and depends solely on the r coordinate. Therefore, it is possible to reduce it to two equations with the separation constant η . Then³

$$\begin{aligned} & \left(\Delta_{(0)} + \alpha \Delta_{(1)} \right) \frac{1}{E^2} \left(\frac{dS_r}{dr} \right)^2 \\ & = -a^2 \left(\frac{\xi^2 (2M - r) + 4rM^2}{r(2M - r)^2} \right) - \frac{4\xi Ma}{r - 2M} + \frac{r^3}{r - 2M} - \eta - \xi^2 \\ & - \alpha \left(\frac{2(12M^3 + 5M^2 r + 6Mr^2 - 6r^3)}{3M(r - 2M)^2} - \frac{4a(4M^2 + 3Mr - 3r^2)\xi}{3(2M - r)^2 r^2} \right), \end{aligned} \quad (4.2.76)$$

$$\frac{1}{E^2} \left(\frac{dS_\theta}{d\theta} \right)^2 = a^2 \cos^2 \theta - \xi^2 \cot^2 \theta + \eta, \quad (4.2.77)$$

where $\xi = L/E$. Now we can separate

$$S_r = S_r^{(0)} + \alpha S_r^{(1)}, \quad S_\theta = S_\theta^{(0)} + \alpha S_\theta^{(1)}, \quad (4.2.78)$$

replace this splitting into (4.2.76) and (4.2.77), collecting in α we will obtain the α' -corrections of S_r and S_θ of Kerr.

³Note that we sum and subtract ξ that gives that $\cot^2 \theta$

$$\frac{1}{E^2} \left(\frac{dS_\theta}{d\theta} \right)^2 = a^2 \cos^2 \theta - \frac{\xi^2}{\sin^2 \theta} + \eta + \xi^2 = a^2 \cos^2 \theta - \xi^2 \frac{\cos^2 \theta}{\sin^2 \theta} + \eta$$

Finally, this outcome suggests that the equations for null geodesics can be solved using analytical methods. This potentially allows us to determine the shape of the shadow for the slowly rotating solution of a black hole in α' -corrected. It also opens up the opportunity to explore it through ray tracing simulations, employing models already demonstrated, such as the thin disk model. This objective is on the horizon and is being prepared for investigation at the time of writing this thesis.

Chapter 5

Summary and discussion

Throughout this research, we delved into deviations from the Kerr metric with the aim of clarifying their theoretical functioning, from the analysis of their photon rings to their potential observability or measurability in supermassive black hole (SMBH) observations. We do this by exploring the radiative transport and the structure of the accretion disk in the vicinity of these objects, using simulations of General Relativistic Magnetohydrodynamics (GRMHD) and ray-tracing algorithms, particularly using the RAPTOR code.

We focused on deviations from Kerr metrics, particularly the Kerr-Like and slowly rotating Chern-Simons metrics, further a slowly-rotating solution for the α' -corrected theory, establishing a foundation for future investigations. We compared simulations of these metrics with simulations based on the Kerr metric to quantify their differences.

We observed that some deviations can significantly alter the morphology of photon rings and the black hole shadow. This is particularly evident in the Kerr-Like metric, in the first-order deviation parameters α_{13} and α_{22} , which influence the intensity profiles, diameter, displacement, and asymmetry of the shadow. These deviations are maximized when the spin parameter approaches its highest value ($a \approx M$), and the inclination angle of the black hole is closer to edge-on ($i \approx 90^\circ$). This is where a significant difference in the shadow geometry compared to that produced by a Kerr black hole without these deviations has been observed, particularly in its diameter and asymmetry, at least for the cases we have studied, especially for the Kerr-Like metric.

On the other hand, the structure of the accretion disk plays a crucial role in quantifying the black hole shadow. Depending on the fluid model in the vicinity of the horizon, shadow measurements can be distorted by the structure itself, especially when the viewing angle of the black hole is perpendicular to its rotation axis (edge-on), assuming that the disk is distributed along this axis. We also note that in simulations where the disk dominates, the theoretical adjustments calculated by [Johannsen \(2013a\)](#) for the diameter, displacement, and asymmetry of the photon ring do not accurately reflect reality. However, they provide information about the deviations.

We conclude that, in terms of the effect of radiative transport around these deviant Kerr-like metrics, differences from the Kerr metric can be noticeable, especially when the disk's structure is also affected. Quantification based on diameter, displacement, and asymmetry, derived from intensity profiles, appears effective for measuring these deviations.

We note that the Kerr-like metric can produce similar images of a Kerr black hole with different spin parameter. Deviations from the Kerr metric such as $\alpha_{22} = 1$ with a certain rotation parameter can produce changes in the shadow for thin-disk simulations such that it is indistinguishable from the shadow for a Kerr black hole with a completely different rotation parameter. As well as coupling values $\zeta_{CS} \leq 1$ in the slowly rotating black hole solution for the Chern-Simons dynamic theory do not produce any significant effect on the shadow of a black hole compared to the usual Kerr metric.

Our findings contribute to the literature on Kerr metric deviations and modified gravity. They align with previous studies such as ([Johannsen, 2013a,b, 2014](#)) for Kerr-Like and ([Yunes and Pretorius, 2009; Ayzenberg and Yunes, 2018](#)) for the Chern-Simons solution. Our work expands the study of these theories and explores new ones, like the α' -corrected theory.

This study opens the door to a deeper analysis of deviant Kerr metrics and their impact on SMBH images. While our simulations focused on specific disk models and theories, we aim to broaden our scope to include more complex radiative transport models. We also emphasize the potential of this method to distinguish deviations from the Kerr metric from the Kerr metric through observations of black hole shadows.

Our findings enrich theoretical understanding and could have observational implications that could be measured by the Event Horizon Telescope (EHT). We emphasize that ideal SMBHs for measuring these possible deviations in observations are those with high spin values and inclination angles such that we observe them through an axis perpendicular to their rotation axis. Currently, the results obtained by the EHT (Akiyama et al., 2019, 2022), which show images of SMBHs at the center of our galaxy and in the center of Messier 87, suggest that when contrasted with GRMHD simulations, both sources seem to have high spin parameters ($a > 0.5M$), but low inclinations ($i < 50^\circ$) or rather near face-on inclinations. This indicates that these objects might be where these deviations could be measurable, but only slightly. For stronger tests, it would be useful to have sources that meet both characteristics. In this context, additionally, the new ngEHT project (Next Generation Event Horizon Telescope) will bring rapid advancements in improving the visibility of these sources and new sources. By using advances in Very Long Baseline Interferometry (VLBI) techniques, it will be able to create a virtual telescope the size of the Earth, enhancing the resolution and sensitivity of observations. This will allow capturing images and even videos of black holes, quantifying photon rings, and improving the precision in measuring BH properties. It will also enable advances in the study of magnetic fields in accretion disks and the origin of jets. Ultimately, this will allow for a more accurate comparison of Kerr-deviated images with the real image of a black hole.

Finally, these results inspire me to delve further into the intricacies of the deviations from Kerr metrics and their effects on black hole images. My comprehension of these enigmatic objects has deepened, and I am excited to continue exploring and contributing to scientific advancement in this field.

Bibliography

- Abbott, B. P., Abbott, R., Abbott, T., Abernathy, M., Acernese, F., Ackley, K., Adams, C., Adams, T., Addesso, P., Adhikari, R., et al. (2016). Observation of gravitational waves from a binary black hole merger. *Physical review letters*, 116(6):061102.
- Adams, W. S. (1925). The relativity displacement of the spectral lines in the companion of sirius. *Proceedings of the National Academy of Sciences*, 11(7):382–387.
- Agurto-Sepúlveda, F., Chernicoff, M., Giribet, G., Oliva, J., and Oyarzo, M. (2023). Slowly rotating and accelerating α' -corrected black holes in four and higher dimensions. *Phys. Rev. D*, 107(8):084014.
- Akiyama, K., Alberdi, A., Alef, W., Algaba, J. C., Anantua, R., Asada, K., Azulay, R., Bach, U., Baczko, A.-K., Ball, D., et al. (2022). First sagittarius a* event horizon telescope results. v. testing astrophysical models of the galactic center black hole. *The Astrophysical Journal Letters*, 930(2):L16.
- Akiyama, K., Alberdi, A., Alef, W., Asada, K., Azulay, R., Baczko, A.-K., Ball, D., Baloković, M., Barrett, J., Bintley, D., et al. (2019). First m87 event horizon telescope results. v. physical origin of the asymmetric ring. *The Astrophysical Journal Letters*, 875(1):L5.
- Alexander, S. and Yunes, N. (2009). Chern–simons modified general relativity. *Physics Reports*, 480(1-2):1–55.
- Amarilla, L., Eiroa, E. F., and Giribet, G. (2010). Null geodesics and shadow of a rotating black hole in extended chern-simons modified gravity. *Physical Review D*, 81(12).
- Appel, A. (1968). Some techniques for shading machine renderings of solids. In *Proceedings of the April 30–May 2, 1968, spring joint computer conference*, pages 37–45.
- Archibald, A. M., Gusinskaia, N. V., Hessels, J. W., Deller, A. T., Kaplan, D. L., Lorimer, D. R., Lynch, R. S., Ransom, S. M., and Stairs, I. H. (2018). Universality of free fall from the orbital motion of a pulsar in a stellar triple system. *Nature*, 559(7712):73–76.
- Ayzenberg, D., Yagi, K., and Yunes, N. (2016). Can the Slow-Rotation

- Approximation be used in Electromagnetic Observations of Black Holes? *Class. Quant. Grav.*, 33(10):105006.
- Ayzenberg, D. and Yunes, N. (2018). Black Hole Shadow as a Test of General Relativity: Quadratic Gravity. *Class. Quant. Grav.*, 35(23):235002.
- Balbus, S. A. and Hawley, J. F. (1990). A powerful local shear instability in weakly magnetized disks: I. linear analysis. In *Bulletin of the American Astronomical Society*, Vol. 22, p. 1209, volume 22, page 1209.
- Bandyopadhyay, B., Fendt, C., Schleicher, D. R., Lagunas, J., Pedreros, J., Nagar, N. M., and Agurto, F. (2023). Signatures of winds and jets in the environment of supermassive black holes. *arXiv preprint arXiv:2303.06650*.
- Bandyopadhyay, B., Fendt, C., Schleicher, D. R., and Vourellis, C. (2021). General relativistic radiation transport: implications for vlbi/eht observations of agn discs, winds, and jets. *Monthly Notices of the Royal Astronomical Society*, 507(4):4933–4952.
- Bardeen, J. M. (1973). Timelike and null geodesics in the Kerr metric. *Proceedings, Ecole d'Eté de Physique Théorique: Les Astres Occlus : Les Houches, France, August, 1972*, 215-240, pages 215–240.
- Belczynski, K., Bulik, T., Fryer, C. L., Ruitter, A., Valsecchi, F., Vink, J. S., and Hurley, J. R. (2010). On the maximum mass of stellar black holes. *The Astrophysical Journal*, 714(2):1217.
- Biriukov, A., Kauts, V., Kulagin, V., Litvinov, D., and Rudenko, V. (2014). Gravitational redshift test with the space radio telescope “radioastron”. *Astronomy Reports*, 58:783–795.
- Boehle, A., Ghez, A., Schödel, R., Meyer, L., Yelda, S., Albers, S., Martinez, G., Becklin, E., Do, T., Lu, J., et al. (2016). An improved distance and mass estimate for sgr a* from a multistar orbit analysis. *The Astrophysical Journal*, 830(1):17.
- Broderick, A. E. (2006). Radiative transfer along rays in curved space–times. *Monthly Notices of the Royal Astronomical Society: Letters*, 366(1):L10–L12.
- Bronzwaer, T., Davelaar, J., Younsi, Z., Mościbrodzka, M., Falcke, H., Kramer, M., and Rezzolla, L. (2018). Raptor-i. time-dependent radiative transfer in arbitrary spacetimes. *Astronomy & Astrophysics*, 613:A2.
- Bronzwaer, T., Davelaar, J., Younsi, Z., Mościbrodzka, M., Olivares, H., Mizuno, Y., Vos, J., and Falcke, H. (2021). Visibility of black hole shadows in low-luminosity agn. *Monthly Notices of the Royal Astronomical Society*, 501(4):4722–4747.
- Bronzwaer, T., Younsi, Z., Davelaar, J., and Falcke, H. (2020). Raptor-ii. polarized radiative transfer in curved spacetime. *Astronomy & Astrophysics*, 641:A126.

- Burgay, M., D'Amico, N., Possenti, A., Manchester, R., Lyne, A., Joshi, B., McLaughlin, M., Kramer, M., Sarkissian, J., Camilo, F., et al. (2003). An increased estimate of the merger rate of double neutron stars from observations of a highly relativistic system. *Nature*, 426(6966):531–533.
- Cano, P. A., Chimento, S., Linares, R., Ortín, T., and Ramírez, P. F. (2020). α' corrections of Reissner-Nordström black holes. *JHEP*, 02:031.
- Cano, P. A., Meessen, P., Ortín, T., and Ramírez, P. F. (2018). α' -corrected black holes in String Theory. *JHEP*, 05:110.
- Carter, B. (1968). Global structure of the kerr family of gravitational fields. *Physical Review*, 174(5):1559.
- Chan, C.-K., Psaltis, D., Özel, F., Narayan, R., Sa, A., et al. (2015). The power of imaging: constraining the plasma properties of grmhd simulations using eht observations of sgr a. *The Astrophysical Journal*, 799(1):1.
- Chandrasekhar, S. (1935). The highly collapsed configurations of a stellar mass (second paper). *Monthly Notices of the Royal Astronomical Society*, Vol. 95, p. 207-225, 95:207–225.
- Collaboration, E. H. T., Akiyama, K., Alberdi, A., Alef, W., Asada, K., AZULY, R., et al. (2019). First m87 event horizon telescope results. i. the shadow of the supermassive black hole. *Astrophys. J. Lett*, 875(1):L1.
- Cunningham, C. and Bardeen, J. M. (1973). The optical appearance of a star orbiting an extreme kerr black hole. *Astrophysical Journal*, Vol. 183, pp. 237-264 (1973), 183:237–264.
- Dauser, T., Wilms, J., Reynolds, C., and Brenneman, L. (2010). Broad emission lines for a negatively spinning black hole. *Monthly Notices of the Royal Astronomical Society*, 409(4):1534–1540.
- Davis, S. W. and Hubeny, I. (2006). A grid of relativistic, non-lte accretion disk models for spectral fitting of black hole binaries. *The Astrophysical Journal Supplement Series*, 164(2):530.
- De Villiers, J.-P. and Hawley, J. F. (2003). A numerical method for general relativistic magnetohydrodynamics. *The Astrophysical Journal*, 589(1):458.
- Debney, G., Kerr, R. P., and Schild, A. (1969). Solutions of the einstein and einstein-maxwell equations. *Journal of Mathematical Physics*, 10(10):1842–1854.
- Dexter, J. (2016). grtrans: Polarized general relativistic radiative transfer via ray tracing. *Astrophysics Source Code Library*, pages ascl–1605.
- Dexter, J. and Agol, E. (2009). A fast new public code for computing photon orbits in a kerr spacetime. *The Astrophysical Journal*, 696(2):1616.
- Dexter, J., Agol, E., and Fragile, P. C. (2009). Millimeter flares and vlbi

- visibilities from relativistic simulations of magnetized accretion onto the galactic center black hole. *The Astrophysical Journal*, 703(2):L142.
- Dexter, J. and Fragile, P. C. (2011). Observational signatures of tilted black hole accretion disks from simulations. *The Astrophysical Journal*, 730(1):36.
- Dexter, J., McKinney, J. C., and Agol, E. (2012). The size of the jet launching region in m87. *Monthly Notices of the Royal Astronomical Society*, 421(2):1517–1528.
- Dolence, J. C., Gammie, C. F., Mościbrodzka, M., and Leung, P. K. (2009). grmonty: a monte carlo code for relativistic radiative transport. *The Astrophysical Journal Supplement Series*, 184(2):387.
- Dyson, F., Eddington, A., and Davidson, C. (1920). A determination of the deflection of the light by the sun's gravitational field, in philosophical transactions of the royal society. *Series A*, pages 291–298.
- Einstein, A. (1915a). Die feldgleichungen der gravitation. *Sitzungsberichte der Königlich Preussischen Akademie der Wissenschaften*, pages 844–847.
- Einstein, A. (1915b). Erklärung der perihelbewegung des merkur aus der allgemeinen relativitätstheorie. *Sitzungsberichte der königlich preussischen Akademie der Wissenschaften*, pages 831–839.
- Einstein, A. (1916). Näherungsweise integration der feldgleichungen der gravitation. *Sitzungsberichte der Königlich Preussischen Akademie der Wissenschaften*, pages 688–696.
- Einstein, A. (1918). Über gravitationswellen. *Sitzungsberichte der Königlich Preussischen Akademie der Wissenschaften*, pages 154–167.
- Einstein, A. (1989). Relativitätsprinzip und die aus demselben gezogenen folgerungen. *Collected Papers of Albert Einstein*, 2:255.
- Falcke, H., Melia, F., and Agol, E. (1999). Viewing the shadow of the black hole at the galactic center. *The Astrophysical Journal*, 528(1):L13.
- Fanton, C., Calvani, M., de Felice, F., and Čadež, A. (1997). Detecting accretion disks in active galactic nuclei. *Publications of the Astronomical Society of Japan*, 49(2):159–169.
- Farr, W. M., Sravan, N., Cantrell, A., Kreidberg, L., Bailyn, C. D., Mandel, I., and Kalogera, V. (2011). The mass distribution of stellar-mass black holes. *The Astrophysical Journal*, 741(2):103.
- Ferrarese, L., Côté, P., Dalla Bontà, E., Peng, E. W., Merritt, D., Jordán, A., Blakeslee, J. P., Haşegan, M., Mei, S., Piatek, S., et al. (2006). A fundamental relation between compact stellar nuclei, supermassive black holes, and their host galaxies. *The Astrophysical Journal*, 644(1):L21.

- Ferrarese, L. and Merritt, D. (2000). A fundamental relation between supermassive black holes and their host galaxies. *The Astrophysical Journal*, 539(1):L9.
- Gair, J. R., Vallisneri, M., Larson, S. L., and Baker, J. G. (2013). Testing general relativity with low-frequency, space-based gravitational-wave detectors. *Living Reviews in Relativity*, 16(1):1–109.
- Gallo, E., Treu, T., Jacob, J., Woo, J.-H., Marshall, P. J., and Antonucci, R. (2008). Amuse-virgo. i. supermassive black holes in low-mass spheroids. *The Astrophysical Journal*, 680(1):154.
- Gammie, C. F., McKinney, J. C., and Tóth, G. (2003). Harm: a numerical scheme for general relativistic magnetohydrodynamics. *The Astrophysical Journal*, 589(1):444.
- Ghez, A., Salim, S., Hornstein, S. D., Tanner, A., Lu, J., Morris, M., Becklin, E., and Duchêne, G. (2005). Stellar orbits around the galactic center black hole. *The Astrophysical Journal*, 620(2):744.
- Gold, R., McKinney, J. C., Johnson, M. D., and Doeleman, S. S. (2017). Probing the magnetic field structure in on black hole horizon scales with polarized radiative transfer simulations. *The Astrophysical Journal*, 837(2):180.
- Gralla, S. E., Holz, D. E., and Wald, R. M. (2019). Black hole shadows, photon rings, and lensing rings. *Physical Review D*, 100(2):024018.
- Gralla, S. E., Lupsasca, A., and Marrone, D. P. (2020). The shape of the black hole photon ring: A precise test of strong-field general relativity. *Physical Review D*, 102(12):124004.
- Gross, D. J. and Witten, E. (1986). Superstring Modifications of Einstein's Equations. *Nucl. Phys. B*, 277:1.
- Gültekin, K., Richstone, D. O., Gebhardt, K., Lauer, T. R., Tremaine, S., Aller, M. C., Bender, R., Dressler, A., Faber, S., Filippenko, A. V., et al. (2009). The $m-\sigma$ and $m-l$ relations in galactic bulges, and determinations of their intrinsic scatter. *The Astrophysical Journal*, 698(1):198.
- Henrik (2023). Ray trace diagram. Accessed on August 20, 2023.
- Johannsen, T. (2013a). Photon rings around kerr and kerr-like black holes. *The Astrophysical Journal*, 777(2):170.
- Johannsen, T. (2013b). Regular black hole metric with three constants of motion. *Physical Review D*, 88(4):044002.
- Johannsen, T. (2013c). Systematic study of event horizons and pathologies of parametrically deformed kerr spacetimes. *Physical Review D*, 87(12):124017.
- Johannsen, T. (2014). X-ray probes of black hole accretion disks for testing the no-hair theorem. *Physical Review D*, 90(6):064002.

- Kerr, R. P. (1963). Gravitational field of a spinning mass as an example of algebraically special metrics. *Physical review letters*, 11(5):237.
- Kormendy, J. and Richstone, D. (1995). Inward bound—the search for supermassive black holes in galactic nuclei. *Annual review of astronomy and Astrophysics*, 33(1):581–624.
- Kulkarni, A. K., Penna, R. F., Shcherbakov, R. V., Steiner, J. F., Narayan, R., Sądowski, A., Zhu, Y., McClintock, J. E., Davis, S. W., and McKinney, J. C. (2011). Measuring black hole spin by the continuum-fitting method: effect of deviations from the novikov–thorne disc model. *Monthly Notices of the Royal Astronomical Society*, 414(2):1183–1194.
- Le Verrier, U. J. (1859). Theorie du mouvement de mercure. *Annales de l’Observatoire imperial de Paris; t. 5; Annales de l’Observatoire de Paris. Memoires; t. 5., Paris: Mallet-Bachelier, 1859., 195 p.; 28 cm., 5.*
- Leung, P. K., Gammie, C. F., and Noble, S. C. (2011). Numerical calculation of magnetobremstrahlung emission and absorption coefficients. *The Astrophysical Journal*, 737(1):21.
- Li, L.-X., Zimmerman, E. R., Narayan, R., and McClintock, J. E. (2005). Multitemperature blackbody spectrum of a thin accretion disk around a kerr black hole: model computations and comparison with observations. *The Astrophysical Journal Supplement Series*, 157(2):335.
- Lin, D., Strader, J., Romanowsky, A. J., Irwin, J. A., Godet, O., Barret, D., Webb, N. A., Homan, J., and Remillard, R. A. (2020). Multiwavelength follow-up of the hyperluminous intermediate-mass black hole candidate 3xmm j215022.4- 055108. *The Astrophysical Journal Letters*, 892(2):L25.
- Lindquist, R. W. (1966). Relativistic transport theory. *Annals of Physics*, 37(3):487–518.
- Lo, K.-H., Young, K., and Lee, B. Y. (2013). Advance of perihelion. *American journal of physics*, 81(9):695–702.
- Luminet, J.-P. (1979). Image of a spherical black hole with thin accretion disk. *Astronomy and Astrophysics*, vol. 75, no. 1-2, May 1979, p. 228-235., 75:228–235.
- Madau, P., Haardt, F., and Dotti, M. (2014). Super-critical growth of massive black holes from stellar-mass seeds. *The Astrophysical Journal Letters*, 784(2):L38.
- Maeda, K.-i., Ohta, N., and Sasagawa, Y. (2009). Black Hole Solutions in String Theory with Gauss-Bonnet Curvature Correction. *Phys. Rev. D*, 80:104032.
- Maoz, E. (1998). Dynamical constraints on alternatives to supermassive black holes in galactic nuclei. *The Astrophysical Journal*, 494(2):L181.
- Marck, J.-A. (1996). Short-cut method of solution of geodesic equations for schwarzschild black hole. *Classical and Quantum Gravity*, 13(3):393.

- Markoff, S., Collaboration, E. H. T., et al. (2022). First sagittarius a* event horizon telescope results: The shadow of the supermassive black hole in the center of the milky way. In *American Astronomical Society Meeting Abstracts*, volume 54, pages 211–01.
- McConnell, N. J. and Ma, C.-P. (2013). Revisiting the scaling relations of black hole masses and host galaxy properties. *The Astrophysical Journal*, 764(2):184.
- McKinney, J. C. and Gammie, C. F. (2004). A measurement of the electromagnetic luminosity of a kerr black hole. *The astrophysical journal*, 611(2):977.
- Merritt, D. (1999). Black holes and galaxy evolution. *arXiv preprint astro-ph/9910546*.
- Metsaev, R. R. and Tseytlin, A. A. (1987). Order alpha-prime (Two Loop) Equivalence of the String Equations of Motion and the Sigma Model Weyl Invariance Conditions: Dependence on the Dilaton and the Antisymmetric Tensor. *Nucl. Phys. B*, 293:385–419.
- Mościbrodzka, M., Falcke, H., and Shiokawa, H. (2016). General relativistic magnetohydrodynamical simulations of the jet in m 87. *Astronomy & Astrophysics*, 586:A38.
- Mościbrodzka, M., Gammie, C. F., Dolence, J. C., Shiokawa, H., and Leung, P. K. (2009). Radiative models of sgr a* from grmhd simulations. *The Astrophysical Journal*, 706(1):497.
- Narayan, R., Johnson, M. D., and Gammie, C. F. (2019). The shadow of a spherically accreting black hole. *The Astrophysical Journal Letters*, 885(2):L33.
- Noble, S. C. and Krolik, J. H. (2009). Grmhd prediction of coronal variability in accreting black holes. *The Astrophysical Journal*, 703(1):964.
- Noble, S. C., Krolik, J. H., Schnittman, J. D., and Hawley, J. F. (2011). Radiative efficiency and thermal spectrum of accretion onto schwarzschild black holes. *The Astrophysical Journal*, 743(2):115.
- Noble, S. C., Leung, P. K., Gammie, C. F., and Book, L. G. (2007). Simulating the emission and outflows from accretion discs. *Classical and Quantum Gravity*, 24(12):S259.
- Novikov, I. D. and Thorne, K. S. (1973). Astrophysics of black holes. *Black holes (Les astres occlus)*, 1:343–450.
- Oppenheimer, J. R. and Volkoff, G. M. (1939). On massive neutron cores. *Physical Review*, 55(4):374.
- Page, D. N. and Thorne, K. S. (1974). Disk-accretion onto a black hole. time-averaged structure of accretion disk. *The Astrophysical Journal*, 191:499–506.

- Rhoades Jr, C. E. and Ruffini, R. (1974). Maximum mass of a neutron star. *Physical Review Letters*, 32(6):324.
- Roelofs, F., Falcke, H., Brinkerink, C., Mościbrodzka, M., Gurvits, L. I., Martín-Neira, M., Kudriashov, V., Klein-Wolt, M., Tilanus, R., Kramer, M., et al. (2019). Simulations of imaging the event horizon of sagittarius a* from space. *Astronomy & Astrophysics*, 625:A124.
- Roll, P. G., Krotkov, R., and Dicke, R. H. (1964). The equivalence of inertial and passive gravitational mass. *Annals of Physics*, 26(3):442–517.
- Ryan, F. D. (1995). Gravitational waves from the inspiral of a compact object into a massive, axisymmetric body with arbitrary multipole moments. *Physical Review D*, 52(10):5707.
- Schlamminger, S., Choi, K.-Y., Wagner, T. A., Gundlach, J. H., and Adelberger, E. G. (2008). Test of the equivalence principle using a rotating torsion balance. *Physical Review Letters*, 100(4):041101.
- Schnittman, J. D., Krolik, J. H., and Hawley, J. F. (2006). Light curves from an mhd simulation of a black hole accretion disk. *The Astrophysical Journal*, 651(2):1031.
- Schwarzschild, K. (1916). Über das gravitationsfeld eines massenpunktes nach der einsteinschen theorie. *Sitzungsberichte der königlich preussischen Akademie der Wissenschaften*, pages 189–196.
- Shakura, N. I. and Sunyaev, R. A. (1973). Black holes in binary systems. observational appearance. *Astronomy and Astrophysics*, Vol. 24, p. 337-355, 24:337–355.
- Shapiro, I. I. (1964). Fourth test of general relativity. *Physical Review Letters*, 13(26):789.
- Shapiro, I. I., Pettengill, G. H., Ash, M. E., Stone, M. L., Smith, W. B., Ingalls, R. P., and Brockelman, R. A. (1968). Fourth test of general relativity: preliminary results. *Physical Review Letters*, 20(22):1265.
- Shapiro, S. L. and Teukolsky, S. A. (2008). *Black holes, white dwarfs, and neutron stars: The physics of compact objects*. John Wiley & Sons.
- Shapiro, S. S., Davis, J. L., Lebach, D. E., and Gregory, J. (2004). Measurement of the solar gravitational deflection of radio waves using geodetic very-long-baseline interferometry data, 1979–1999. *Physical Review Letters*, 92(12):121101.
- Spera, M., Mapelli, M., and Bressan, A. (2015). The mass spectrum of compact remnants from the parsec stellar evolution tracks. *Monthly Notices of the Royal Astronomical Society*, 451(4):4086–4103.
- Swope, W. C., Andersen, H. C., Berens, P. H., and Wilson, K. R. (1982). A computer simulation method for the calculation of equilibrium constants for

- the formation of physical clusters of molecules: Application to small water clusters. *The Journal of chemical physics*, 76(1):637–649.
- Tóth, G. (2000). The $b=0$ constraint in shock-capturing magnetohydrodynamics codes. *Journal of Computational Physics*, 161(2):605–652.
- v. Eötvös, R., Pekár, D., and Fekete, E. (1922). Beiträge zum gesetze der proportionalität von trägheit und gravität. *Annalen der Physik*, 373(9):11–66.
- van den Heuvel, E. P. (1992). Endpoints of stellar evolution: the incidence of stellar mass black holes in the galaxy. *Environment Observation and Climate Modelling Through International Space Projects*, pages 29–36.
- Vincent, F. H., Paumard, T., Gourgoulhon, E., and Perrin, G. (2011). Gyoto: a new general relativistic ray-tracing code. *Classical and Quantum Gravity*, 28(22):225011.
- Vitral, E., Libralato, M., Kremer, K., Mamon, G. A., Bellini, A., Bedin, L. R., and Anderson, J. (2023). An elusive dark central mass in the globular cluster m4. *Monthly Notices of the Royal Astronomical Society*, 522(4):5740–5757.
- Voisin, G., Cognard, I., Freire, P. C., Wex, N., Guillemot, L., Desvignes, G., Kramer, M., and Theureau, G. (2020). An improved test of the strong equivalence principle with the pulsar in a triple star system. *Astronomy & Astrophysics*, 638:A24.
- Webster, B. L. and Murdin, P. (1972). Cygnus x-1—a spectroscopic binary with a heavy companion? *Nature*, 235(5332):37–38.
- Whitted, T. (1979). An improved illumination model for shaded display. In *Proceedings of the 6th annual conference on Computer graphics and interactive techniques*, page 14.
- Wu, X.-B., Wang, F., Fan, X., Yi, W., Zuo, W., Bian, F., Jiang, L., McGreer, I. D., Wang, R., Yang, J., et al. (2015). An ultraluminous quasar with a twelve-billion-solar-mass black hole at redshift 6.30. *Nature*, 518(7540):512–515.
- Younsi, Z., Zhidenko, A., Rezzolla, L., Konoplya, R., and Mizuno, Y. (2016). New method for shadow calculations: Application to parametrized axisymmetric black holes. *Physical Review D*, 94(8):084025.
- Yunes, N. and Pretorius, F. (2009). Dynamical chern-simons modified gravity: Spinning black holes in the slow-rotation approximation. *Physical Review D*, 79(8).
- Yunes, N. and Siemens, X. (2013). Gravitational-wave tests of general relativity with ground-based detectors and pulsar-timing arrays. *Living Reviews in Relativity*, 16(1):1–124.

Appendix A

Supplementary calculations

A1 Modified coordinates

Here we present a non-trivial coordinates transformations used by RAPTOR code. From Boyer-Lindquist coordinates to Modified Kerr-Schild coordinates,

A1.1 From Boyer-Lindquist to Kerr-Schild

The transformations between the coordinate vector is given by (see. (CITAR FONT.)):

$$\hat{t} = t + M \ln \Delta + \frac{2M^2}{r_+ - r_-} \ln \left(\frac{r - r_+}{r - r_-} \right), \quad (\text{A1.1})$$

$$\hat{\phi} = \phi + \frac{a}{r_+ - r_-} \ln \left(\frac{r - r_+}{r - r_-} \right), \quad (\text{A1.2})$$

$$\dot{\hat{t}} = \dot{t} + \frac{2Mr}{\Delta} \dot{r}, \quad (\text{A1.3})$$

$$\dot{\hat{\phi}} = \dot{\phi} + \frac{a}{\Delta} \dot{r}, \quad (\text{A1.4})$$

where the overdot means the differentiation with respect to the affine parameter λ , $r_{\pm} := M \pm \sqrt{M^2 - a^2}$ denotes the outer and inner event horizon radius, $\Delta = r^2 - 2Mr + a^2$ and M is the mass of the black hole.

On the other hand, four-vectors transform differently. In RAPTOR the initial wave vector k_0^μ is always constructed in Boyer-Lindquist coordinates, so must be transformed to Kerr-Schild coordinates. This is do it following the

transformation of [McKinney and Gammie \(2004\)](#)

$$\hat{k}^\alpha = \begin{pmatrix} 1 & 2r/\Delta & 0 & 0 \\ 0 & 1 & 0 & 0 \\ 0 & 0 & 1 & 0 \\ 0 & a/\Delta & 0 & 1 \end{pmatrix} k^\alpha, \quad (\text{A1.5})$$

where k^α denotes de wave vector in Boyer-Lindquist coordinates and \hat{k}^α denotes the wave vector in Kerr-Schild coordinates. The reverse transformation is

$$k^\alpha = \begin{pmatrix} 1 & -2r/\Delta & 0 & 0 \\ 0 & 1 & 0 & 0 \\ 0 & 0 & 1 & 0 \\ 0 & -a/\Delta & 0 & 1 \end{pmatrix} \hat{k}^\alpha. \quad (\text{A1.6})$$

A1.2 From Kerr-Schild to Modified Kerr-Schild coordinates

The modified Kerr-Schild coordinates (MKS) [Gammie et al. \(2003\)](#), are denoted by $(\hat{t}, x^1, x^2, \hat{\phi})$, and are

$$x^1 = \ln r - r_0 \quad (\text{A1.7})$$

$$\dot{x}^1 = \frac{\dot{r}}{r - r_0} \quad (\text{A1.8})$$

$$\dot{x}^2 = \frac{\dot{\theta}}{\pi[1 + (1 - h) \cos(2\pi x^2)]}, \quad (\text{A1.9})$$

where $0 \leq h \leq 1$ is obtained by the GRMHD data and stretches the zenith coordinate near the poles and the equatorial plane. We do not put here the transformation $x^2(\theta)$ because this requires solving a transcendental equation, so RAPTOR find this coordinate numerically. The inverse transformation is

$$r = r_0 + \exp x^1, \quad (\text{A1.10})$$

$$\theta = \pi x^2 + \frac{1}{2}(1 - h) \sin(2\pi x^2), \quad (\text{A1.11})$$

$$\dot{r} = \dot{x}^1(r - r_0), \quad (\text{A1.12})$$

$$\dot{\theta} = \pi \dot{x}^2 [1 + (1 - h) \cos(2\pi x^2)]. \quad (\text{A1.13})$$

to find $\theta \rightarrow x^2$. RAPTOR solves numerically the equation by a Newton-Raphson algorithm (see Appendix of Bronzwaer et al. (2018)).

A2 Christoffel symbols of Kerr-Like metric

To determine the connection of the Kerr-Like metric in Kerr-Schild coordinates, we utilized Maple software to perform analytical calculations of all components of the Christoffel symbols, to provide a concise perspective and prevent the document from extending beyond necessary limits, we will only present the components (t, t, t) , (r, r, r) , (θ, θ, θ) , and (ϕ, ϕ, ϕ) . The remaining components can be found in the footnote link as a Maple document, where they are also translated into the C programming language. ¹

$$\begin{aligned}
\Gamma^t_{tt} &= \frac{A_1(r) [(\cos^2(\theta)a^2 - a^2)A_2(r)^2 + \Delta(r)] F(r, \theta) \frac{\partial}{\partial r} \Sigma(r, \theta)}{4\Sigma(r, \theta) [(\cos^2(\theta)a^2 - a^2)A_2(r) + A_1(r)(a^2 + r^2)] F(r, \theta)} \\
&\quad \times \left[\frac{\cos^2(\theta)a^2}{2} - \frac{a^2}{2} \right] A_2(r) + A_1(r) \left[Mr + \frac{\Delta(r)}{2} \right]^2 \\
\Gamma^r_{rr} &= \frac{1}{8\Sigma(r, \theta)} \left[\frac{8(a^2 A_2(r) \cos^2(\theta) + A_1(r)a^2 + A_1(r)r^2 - a^2 A_2(r))F(r, \theta)A_5(r)}{\left(\frac{a^2 \Delta(r) (\cos(\theta) - 1)(\cos(\theta) + 1) A_2(r)^2}{8} + M^2 r^2 + \frac{Mr \Delta(r)}{2} + \frac{\Delta(r)^2}{8} \right) A_1(r)^2 + \dots} \right] \\
\Gamma^\theta_{\theta\theta} &= \frac{\frac{\partial}{\partial \theta} \Sigma(r, \theta)}{2\Sigma(r, \theta)} \\
\Gamma^\phi_{\phi\phi} &= -\frac{a\sqrt{A_5(r)} \sin^2(\theta) A_2(r)}{4\Sigma(r, \theta)} \\
&\quad \times \left(A_1(r) \left(Mr + \frac{\Delta(r)}{2} \right) - \frac{a^2 A_2(r) \sin^2(\theta)}{2} \right) \\
&\quad \times F(r, \theta) \left((-a^2 - r^2) A_1(r) + a^2 A_2(r) \sin^2(\theta) \right)
\end{aligned} \tag{A2.1}$$

In the denominator of the equation for Γ^r_{rr} , the "..." is used to represent the omitted terms due to their excessive length.

¹[Link](#)